UNIVERSITÀ
DEGLI STUDI
FIRENZE

DOTTORATO DI RICERCA IN FISICA E ASTRONOMIA

CICLO XXIX
Coordinatore: Massimo Gurioli

HIRES/E-ELT astrobiology science case. Cosmogonic indicators in comets: Targeting a quantum leap using new-generation high-resolution echelle spectrometers.

Settore scientifico disciplinare: FIS/05 Fisica e Astronomia

Tutori
Brucato John Robert
John Robert Brucato

Tozzi Gian Paolo
Gian Paolo

Dottoranda
Faggi Sara
Sara Faggi

Coordinatore
Gurioli Massimo

Anni: 2013/2016

To my parents

In collaboration with:
Michael J. Mumma and Geronimo L. Villanueva
NASA Goddard Space Flight Center

Table of contents

Executive Summary

Life on Earth, as we know it, is based on liquid water and organic chemicals. The search for such molecules in non-terrestrial environments, in order to understand the origin of life on our planet, is one of the main goals of astrobiology.

Our planetary system formed 4.6 billion years ago, from a collapsing cloud of interstellar dust and gas. Hydrogen is strongly underabundant in the bulk Earth (H/O << solar) suggesting that it formed in a dry region, well within the threshold heliocentric distance where water ice is stable (the water snow line). Within the water snow line, only silicates and metals are stable solids and the planetesimals formed from them are rocky. Other gases have their own "snow" lines, whose heliocentric positions increase in distance (R_h) in inverse relation to their condensation temperatures (thus H_2O, CH_3OH, CO_2, NH_3, CO, etc.). All these species remain in the gas-phase at Earth's formative distance (ca. 1 au), because their ices are not stable in such warm inner regions. Earth is too small in mass to capture significant amounts of local nebular gas, which is ultimately swept outward by particles escaping from the proto-Sun (the solar wind) – depleting volatiles from the inner solar system. Lacking other events, Earth should be a dry planet – and indeed, the bulk Earth IS dry (low H/O elemental ratio). But, the surface is wet (high H/O ratio, and H_2O is abundant there!). The reason why so much liquid water covers our planet is still unclear. Delivery of this veneer by impacts of bodies formed farther out – beyond the snow lines – is considered most likely. Beyond the snow lines, hydrogen compounds and rocks can condense (or survive from the natal interstellar cloud core) and will accrete in icy-rocky planetesimals.

According to the “Grand Tack” model, in the first 4-5 Myr of gaseous solar nebula lifetime only giant planets grew to their final sizes, while inner rocky volatile-poor (S-type) and outer icy-rocky (C-type) planetesimals grew to be lunar-sized planetary embryos (Walsh et al., 2012). Simulations showed that few million years after the formation of such solid embryos, but before the final formation of terrestrial planets, a migration of giant planets occurred. Initially, Jupiter and Saturn moved into the inner part of the early solar system driven by mutual orbital resonances and by their interactions with solar nebula gases, and later (the “tack”) retreated into the outer part of the solar system as result of their 2:3 mean resonance motion. The inward migration of the giant planets scattered about ~15% of inner S-type embryos in orbits farther than ~ 4au. After the “tack”, the outward migration of giant planets produced a scattering of the S-type material back inward (only ~0.5% of the original S-type material) and also a inward scatter of the outer C-type material, located between and beyond the original positions of the giant planets. Only a small fraction (a few percent) of C-type material was scattered into the inner part of the solar system. This migration reshuffled the composition of the inner planetesimals and determined the conditions of terrestrial planets formations[1] such as the Earth/Mars mass ratio and the composition of asteroid belt population (Walsh et al., 2012). However, despite rocky and icy bodies being co-mingled in the early asteroid belt and the icy disk; the icy/rocky ratio should differ with heliocentric distance R_h in the icy disk and perhaps also in the cometary forming regions. The end state of the “Grand Tack” model provides the initial conditions for the “Nice” model.

---

[1] Even if Earth formed in this co-mingled population of embryos, it was molten during its early stages due to frequent collisions with other bodies that led to extreme volcanism and material differentiation. Moreover, a huge impact with an almost planet-sized body, believed to be responsible for the formation of the Moon, produced another catastrophic change to its primordial atmosphere. Liquid water was unlikely present.

According to the “Nice” model (Morbidelli et al., 2005), comets (leftovers of icy proto-planetary material) formed in two regions of the proto-planetary disk: between R_h ~ 5 and 15 au (i.e., in the giant planets forming region) and beyond ~20 au. Early on, the four giant planets were surrounded by icy debris, and were maintained in closer orbits than their current ones by a disk of icy bodies, remnants of the early proto-planetary disk. As Saturn and Jupiter scattered planetesimals from their vicinity, they migrated outward until reaching the 2:1 mean motion orbital resonance at ~3.9–3.8 billion years ago, whereupon their combined gravitational perturbations destabilized the orbits of Neptune and Uranus and caused them to switch places. These dynamical instabilities disrupted the icy disk, causing a huge dispersion of icy planetesimals into both the inner and outer parts of the solar system. Icy debris that entered the inner solar system catastrophically collided with the rocky inner planets (and the Moon, see Figure a). Scattered icy nuclei also populated both the Oort cloud (OC) and the Kuiper belt (KB), the actual known cometary reservoirs, but perhaps in different proportions.

Comets are considered the most pristine bodies of the solar system and their investigation provides important information on physical conditions in their formation region(s) in the native proto-planetary disk. Comets may have played an important role in depositing on the primordial Earth the organic matter that was essential for the origin of life. Deep understanding of cometary composition and dynamics is required in order to assess the changes they brought to these impacted bodies.

The heavy cometary bombardment is believed to be responsible for the deposition of about $10^{16} - 10^{18}$ kg of carbon on the primordial Earth, during only 100 My (Gilmour and Sephton, 2004). Water is the most abundant constituent of cometary ices and its production rate is used to quantify cometary activity and serves as the paradigm for all other species.

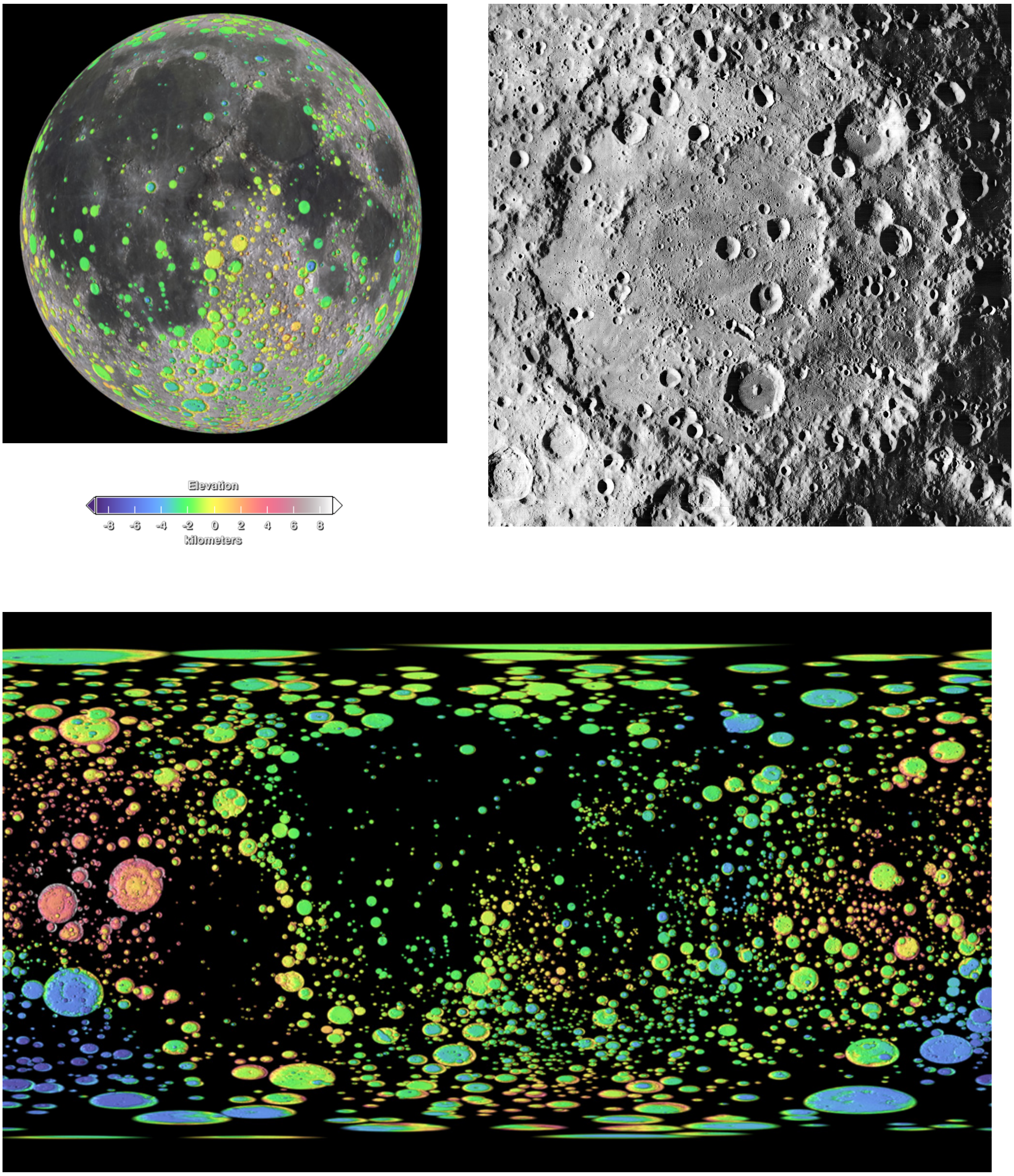

Figure a
Upper left: Moon’s topographic map at high definition obtained by the NASA’s Lunar Reconnaissance Orbiter (LRO). The map reveals the location of more than 5000 craters over 12 miles in diameter. Credit: NASA's Scientific Visualization Studio.
Upper right: Image of Korolov crater acquired by NASA’s Lunar Orbiter 1 mission in 1966, the first American spacecraft orbiting the Moon.
Bottom: Stereographic visualization of the distribution of large and small craters on the Moon. Two distinct populations of impactors are suggested from the size distribution. The blue-colored craters near the bottom of this map lie inside the South Pole-Aitken basin, one of the largest impact basins in the solar system. Credit: NASA's Scientific Visualization Studio, https://svs.gsfc.nasa.gov/3662

Moreover, from past investigations of the D/H ratio water in various bodies of the solar system, the origin of terrestrial water could be attributed (for the most part) to small bodies, such as asteroids and comets. However, our view of the relative contribution of comets is still undergoing rapid change as new measurements are made.

The study of cometary composition is highly relevant for understanding the evolution of our planetary system and for verifying the hypothesis of their delivery of prebiotic compounds to early Earth .

The parameters that can allow us to identify which class of objects delivered water and organics to Earth are cosmogonic indicators: unalterable parameters that reveal the native formative conditions such as temperature, irradiation, heliocentric distance, and so on. The investigation of cosmogonic thermometers encoded by biologically relevant volatiles in cometary comae is a key to understanding the formation and evolution of our planetary system, to testing the delivery of organic matter to the terrestrial planets by small icy bodies and to addressing the puzzling origin of Earth's oceans.

Cosmogonic indicators include:

- **Isotopic ratios**: isotopic enrichment (D/H, $^{13}C/^{12}C$, etc.) of cometary ices is particularly sensitive to the formation conditions. For example, deuteration is a process sensitive to the formation temperature of ices through ion-molecule reactions, and also through H- and D-atom retention on grain surfaces. Fractionation of carbon and nitrogen in isotopologues tests similar formation factors. The comparison with current terrestrial values can test delivery of water and prebiotic material to early Earth.
- **Molecular abundances:** chemical abundances of volatile species are strongly influenced by temperatures at the time of their formation, and by exposure to energetic radiation.

- **Spin temperatures:** the nuclear spin temperature is derived from spin isomeric ratios (e.g., ortho/para water); it may record and preserve the temperature at time of the molecule's formation, or perhaps its exposure to paramagnetic species such as O_2, in the ice phase. The key to unraveling this puzzle is to measure spin temperatures in multiple molecular species, and to compare them with formation temperatures implied by isotopic ratios.

This PhD thesis proposes a new science case regarding cometary science for the next-generation high-resolution echelle spectrometer HIRES/E-ELT. Equipped with a 39 mt primary mirror, the European Extremely Large Telescope (E-ELT) will be Earth's largest ground-based IR-optical telescope. ESO has been developing this project since 2005; it was approved in 2012, and first light is expected in 2024. HIRES (HIgh REsolution Spectrograph) is the future echelle spectrometer for E-ELT with resolving power (RP = $\lambda/\delta\lambda$) ~100,000 and near-infrared wavelength coverage (0.3 – 2.5) μm. The combination of the huge telescope collecting area and the high resolving power of HIRES will enable observations that should contribute significantly to our understanding of the formation and evolution of the solar system and origin of life on our Earth.

This work presents results obtained with the high-resolution echelle spectrometer GIANO/TNG with RP~50,000 – a precursor to HIRES/E-ELT. GIANO is the near-infrared high-resolution spectrograph mounted at the Nasmyth-A focus of the TNG telescope (Telescopio Nazionale Galileo) in La Palma, Canary Islands, Spain. GIANO covers more or less the same infrared spectral range (0.9-2.5) μm as HIRES, so working on GIANO provided essential experience for planning the best use of the future IR high-resolution spectrograph.

We observed the Oort cloud comet C/2014 Q2 (Lovejoy) on 2015 January 31 and February 1 and 2 at a heliocentric distance of 1.3 au and geocentric distance of 0.8 au during its approach to the Sun. We detected strong emissions from the radical CN and water, along with many emission features of unidentified origin, across the 0.9 – 2.5 μm spectral range covered by GIANO. Spectral lines from eight ro-vibrational bands of H_2O were detected, six of them for the first time. We quantified the water production rate [$Q(H_2O) = (3.11 \pm 0.14)x10^{29}\ s^{-1}$] by comparing the calibrated line fluxes with the Goddard full non-resonance cascade fluorescence model for H_2O. The production rates of ortho-water [$Q\ (H_2O)^{ORTHO} = (2.33\pm0.11)\ x10^{29}\ s^{-1}$] and para-water [$Q(H_2O)\ ^{PARA} = (0.87\pm0.21)\ x10^{29}\ s^{-1}$] provide a measure of the ortho-to-para ratio (2.70 ± 0.76). The confidence limits are not small enough to provide a critical test of the nuclear spin temperature. Spectral lines from five ro-vibrational bands of the CN electronic transition ($A^2\Pi$ - $X^2\Sigma^+$, the so-called Red System) were detected across the echellogram. In order to quantify the radical CN production rate we developed a full non-resonance quantum mechanical fluorescence model for the coupled Red, Violet, and Ground State Systems of $^{12}C^{14}N$ and its isotopologues ^{13}CN and $C^{15}N$. By comparing the calibrated line fluxes with the full non-resonance fluorescence cascade model for CN we obtained a radical cyanide production rate of about $Q(CN)= (1.567 \pm 0.026)\ x\ 10^{25}[s^{-1}]$.

The first chapter introduces various relevant aspects of comets, including their structure, icy composition, and their reservoirs. The chapter also describes the importance of cometary science for understanding the early formative stages of formation and evolution of solar system.

Chapter 2 describes solar-pumped fluorescent emission – the main excitation process of IR emission lines in cometary comae – together with the state-of-the-art of near infrared measurements of water and organic compounds.

The third chapter deals with the E-ELT telescope and the HIRES spectrograph, followed by an illustration of the case for cometary science with HIRES/E-ELT.

Chapter four emphasizes the observations of comet Lovejoy performed with the GIANO/TNG spectrograph, the data reduction, and calibration of the spectra. Chapter five covers the identification of the 52 detected water lines, along with the quantum mechanical fluorescence model, the retrieval of rotational temperature, production rate and OPR for water.

Chapter six provides a detailed description of the quantum mechanical fluorescence model for the radical CN, followed by the CN fluorescence analysis – leading to an evaluation of the rotational temperature and production rate in chapter seven. Chapter seven also describes the quantum mechanical structure of the radical CN (its quantum numbers and energy levels), and the theoretical fluorescence pumping and cascade processes. Chapter eight summarizes the results and compares them with other measurements obtained for comet Lovejoy.

Proposed future work that can be conducted with the high-resolution spectrographs available today and in the coming few years are described in Chapter nine. This chapter illustrates the need to conduct observations of bright comets with iSHELL/IRTF, CRIRES+/VLT and GIARPS/TNG, in preparation for the new high-resolution spectrographs on large telescopes. Several promising targets are listed for 2017-18. Four Appendixes appear at the end of the manuscript. Appendix A summarizes the wavelength coverage of the 50 orders of the GIANO echellogram. In Appendix B, results of the flux calibration process are reported. The mean flux calibration factors obtained for the GIANO instrument are shown. A detailed analysis of noise and detector performance is described in Appendix C, while evaluation of GIANO throughputs is reported in Appendix D.

Chapter 1

Comets

Ancient cultures have recorded the appearance of comets for millennia. Dated to the 11th century B.C.E., the Chinese Oracle Bone is the oldest surviving record of a cometary apparition (Festou et al., 2004). By contrast, at that time Western classical culture was pervaded by the Aristotelian idea that comets were phenomena that occurred in the terrestrial atmosphere, and so were of meteorological origin. They were seen as omens of misfortune and were never clearly established as astronomical bodies. The onset of observational astronomy in the XVth century saw the Italian scientist Toscanelli observing many comets and recording them with improved accuracy. Comets were first recognized as extraterrestrial objects in 1577, when the Danish astronomer Tycho Brahe measured the parallax shift of the Great Comet of 1577 from two different locations, demonstrating that the comet was transiting at a distance greater than the Moon's. Applying his gravitational theory in 1687, Sir Isaac Newton demonstrated that comets move along elliptic or parabolic orbits. This led Edmund Halley in 1705 to publish the orbits and periodicities of many comets, and to predict their future returns – famously including that of the bright comet of 1682 now known as 1P/1682 Q1 Halley (cite: *Synopsis Astronomia Cometicae*). Its predicted return in 1758 was observed, confirming Newton's theory of gravitation and the nature of comets as bodies in orbit about the Sun.

However, the passage of 1P/Halley in 1835 opened a new era – science of the comet itself. For the first time the spatial structure of the coma was described in detail and the idea advanced that the observed tail, jets and streamers were associated with dust particles ejected towards the Sun (Festou et al., 2004).

The current picture of comets as an ensemble of primordial ice and dust, interacting with the solar radiation field was born around 1950 with the formulation of three revolutionary ideas: the icy-conglomerate Whipple model[2] the so called "dirty snowball", the discovery of the Oort cloud reservoir[3] (see Chapter 1.2 for further details), and the theory of interaction between the cometary plasma particles with the solar wind (Festou et al., 2004). These three ideas brought the modern concept of comets as the frozen remnants of primordial material accreted in the earliest phases of our solar system. In fact, in the last 40 years comets became interesting targets for space missions and Earth-based observations due to their relevance for understanding the formation and evolution of the proto-solar nebula and the origin of pre-biotic molecules on Earth. Despite the fact that many space missions have been directed to comets and that enormous amounts of data have been collected from telescopes, many questions remain unsolved.

1.1 Comet's structure: nucleus, coma and tails

A comet is characterized by three main components: the nucleus, the coma and the tails (see Figure 1).

---

[2] In the "dirty snowball" theory the nucleus is considered as a mixture of dust and ices from which the gases in the coma are produced by sublimation. The gas in the coma increases as the comet approaches the Sun. This model was largely accepted because it could explain many observed features in the gas coma (jets-like structures), the huge production rates (e.g. C_2) in Halley comet, and the non- gravitational forces induced by the gas outflows.

[3] The idea of a hypothetical distant reservoir of comets was necessary to explain the observed very large values for semi-major axes (a >10,000 AU) displayed by many inbound comets. In the 1950 Oort demonstrated the existence of a cloud studying the distribution of the semimajor axes (a) of 19 comets. He inferred that most of the comets stored in this distant cloud maintain their stable orbits for distances of about 200,000 AU. However, some of them could be diverted inward by the perturbations of passing stars. To explain the discovery rate of new comets each year, Oort estimated that the reservoir should contain a number of comets around $2x10^{11}$. Moreover, considering a mean cometary mass of 10^{13} kg, the mass of the Oort cloud would be around $2x10^{24}$kg, e.g. 0.3 Earth's mass.

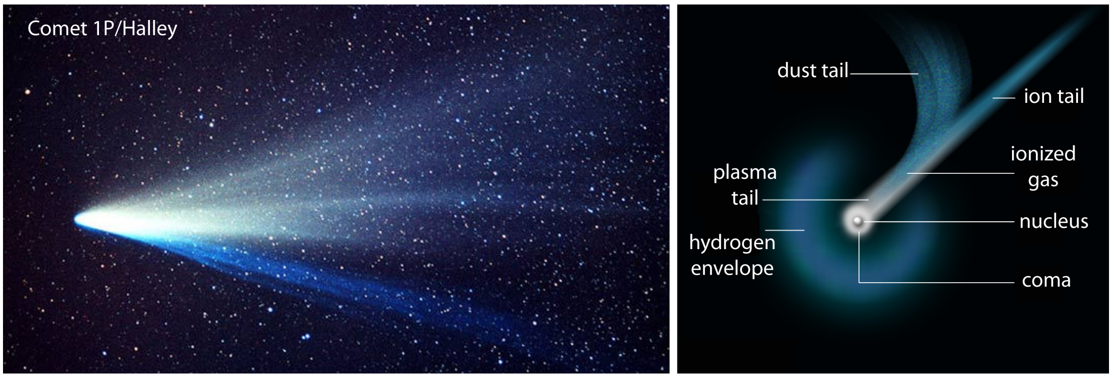

Figure 1. On left panel a colored picture of Comet 1P/Halley on March 1986 shows the different components of ion (in blue) and dust (in white) tails. On right panel a cartooned image of comet structure is reported. The main components (nucleus, coma, tails) are shown.

These components are dynamically related to the cometary activity. In fact, when stored in its reservoir (the Oort cloud or the Kuiper belt[4], see §1.2) a comet is simply a rocky body commonly identified with its "*nucleus*". The nucleus is a mix of rocks, dust (silicates, olivine, refractory carbon-rich molecules etc.) and ices (mainly water ice, CO ices, etc.). The cometary activity begins as the comet approaches the Sun, entering the inner part of the solar system where coma and tail are formed. A comet can leave its stable orbit in the Oort cloud or Kuiper belt due to gravitational instabilities produced by crossing stars, by gravitational attraction of giant molecular clouds or by tidal forces produced by the Milky Way. During its journey to the Sun the comet aspect changes according to the heating received. The frozen gases that form the nucleus start to sublimate, producing a surrounding cloud called "*coma*". The coma is a sort of "dynamic cometary atmosphere", with a shape that changes as the comet approaches the Sun. A mixture of gas and dust composes the coma. The gas is mainly produced by the direct sublimation of ices in the nucleus while the dust is extracted by the sublimating gases and dragged in the surrounding atmosphere. At distances near perihelion, the final component, the "*tail*", is formed. The tail is an extension

---

[4] The Oort cloud is a spherical reservoir of comets located at 50,000 AU far from the Sun. The Kuiper belt is a reservoir located beyond Neptune, between 30 and 100 AU.

of the coma. It is produced by the interaction of the gas and dust in the coma with the solar wind. Comets develop multiple tails: the most famous are the dust tail and the ion tail.

These two tails are formed when the comet is closest to the Sun where both cometary plasma produced after photo-dissociation of product species by solar UV radiation interacts with the solar wind and when cometary dust particles interact with the solar radiation pressure. Only recently in addition to these two tails, a third tail, the neutral gas tail, was discovered by Cremonese in 1997 in comet Hale-Bopp (Cremonese et al., 1997).Tails reach their maximum extension (e.g. ~ 10^7 km) at the closest distance to the Sun.

Nucleus

Cometary nuclei were studied both by ground-based observations and space missions. Earth-based photometric and polarimetric observations could provide hints on their size, approximate shape and possibly rotational characteristics. However, they are too small and faint to be resolved by ground-based telescopes, moreover they are immersed in the coma and obscured by its brightness (Keller et al., 2004; Weissman et al., 2004).

Space missions allowed the study of nucleus properties thanks to a suite of scientific instruments such as high-resolution imagers and visible/infrared/radio spectrometers. Further information can be achieved by *in situ* measurements of dust/gas coma components by mass spectrometers. In the past decades, flybys of comets Halley, Borrelly, Wild 2, Tempel 1, Hartley 2 and (recently) 67P/Churyumov-Gerasimenko taught us that cometary nuclei show significant differences in morphology and composition. For example, both Wild 2 and Tempel 1 showed significant portions of their nuclei characterized by pitted areas, whereas this peculiarity was completely absent in Borrelly and Hartley 2. Comet Tempel 1 showed smoothed flows areas that were also present in Hartley 2, but not observed in Wild 2. Evidence of layering was noted in Borrelly as well as in Wild 2. The morphologies of these six comets are compared in Figure 2. Our understanding of nucleus structure and properties increased dramatically with the recently completed ESA/Rosetta mission to comet 67P/Churyumov- Gerasimenko (hereafter 67P/CG). Since 23 March 2014, when the comet 67P/CG was at a distance of 5 million km, the OSIRIS instrument (Optical Spectroscopic and Infrared Remote Imaging System) provided spectacular images of the nucleus of the comet through its narrow- and wide-angle cameras, NAC and WAC.

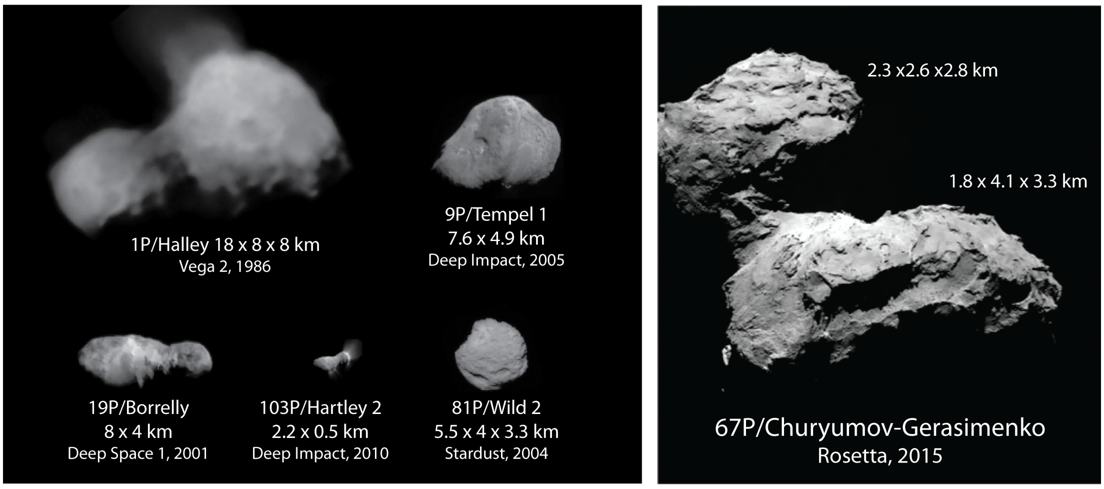

Figure 2. Cometary nuclei visited by space missions. On the left panel five images collected by space missions to comets from 1986 to 2010 are shown. From the top left to the bottom right: comet Halley visited by Vega 2 and Giotto, comet Tempel 1 visited by Deep impact, comet Borrelly visited by Deep Space 1, comet Wild 2 visited by Stardust, and comet Hartley 2 visited by Deep Impact. Right panel shows comet 67P/C-G visited by the Rosetta spacecraft on 2015-2016.

Moreover, the OSIRIS instrument characterized the dust and gas environment with 25 broad- and narrow-band filters covering the wavelength range from 240 to 1000 nm. The “head” of the “duck shaped” 67P/CG comet showed cliffs and aligned linear structures of about 500 m in length, while fractures and erosion features were seen over the entire nucleus at different scales. In the region extending around the “neck” (colloquial way to call the region between the two adhering blocks that form the nucleus), a collection of active pits was observed immersed in a flat floor with depressed regions. Interestingly, new features still not interpreted called “Goosebumps” were observed in several places across the nucleus. These bumps are characterized approximately by the same height (~3 m) that could be a hint of their formation process (Sierks et al., 2015).

Coma

As mentioned before, the cometary coma is composed by two components: the gas and the dust. The coma is formed by the sublimation process of cometary surface ices and it is strongly related to nucleus outgassing activity. The outgassing comes from specific active regions on nucleus surface identified by the particular composition, structure, and morphology. These areas are activated by the amount of solar radiation received. The activity arises as the comet approaches the Sun and varies with respect to the cometary rotational period (see Figure 3).

Although the gas coma comes from the direct sublimation of ices in the nucleus, it does not completely reflect the nucleus composition, because the gas is affected by photochemical reactions and by collisions.

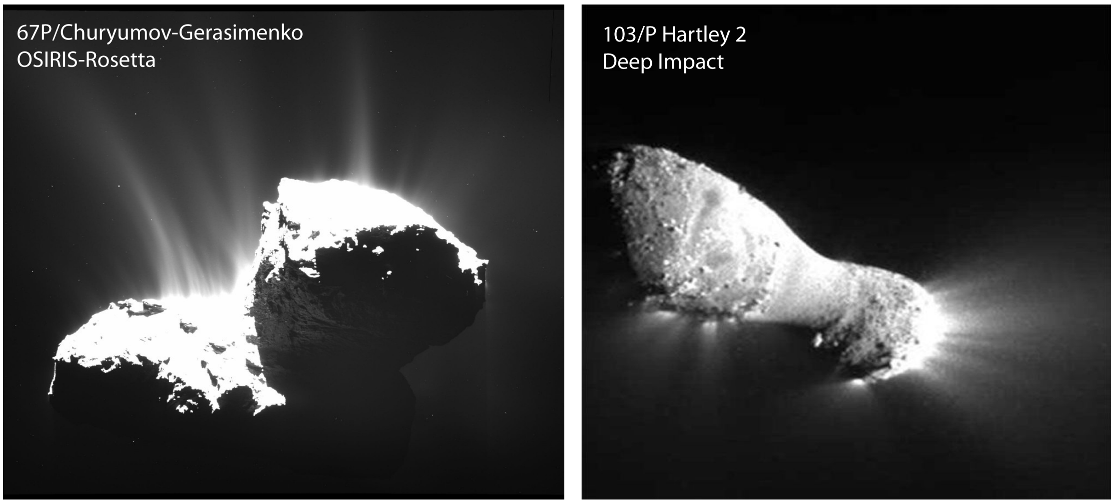

Figure 3. Left panel: OSIRIS wide-angle camera image of Comet 67P/CG acquired on 22 November 2014 from a distance of 30 km with image resolution of 2.8 m/pixel (ESA/Rosetta/MPSforOSIRISTeamMPS/UPD/LAM/IAA/SSO/INTA/UPM/DASP/IDA). Right panel: image of comet Hartley 2 acquired in November 2010 by NASA's EPOXI mission. Credit: NASA/JPL-Caltech/UMD

The volatile coma is composed by "primary" species (the so-called parent species) released by direct sublimation of ices from nucleus and by "product" species (also called daughter species) produced by photo-dissociation and/or photo-ionization processes. Some examples of primary molecules are H_2O, CO, CO_2, CH_3OH (Methanol), CH_2O (Formaldehyde). [Note: a parent volatile need not be a primary volatile – it can itself be a product species, e.g., even if no CO is stored in the nucleus as a ‘primary” volatile, it can be produced in the coma by dissociation of H_2CO or CO_2, and can later be a parent of O and C. For this reason, we prefer the term “primary” and “product” as being uniquely related to the heritage of an individual species, or sub-set of the whole.] Water is the most abundant constituent of cometary ices and its production rate is used to quantify cometary activity and abundance (Mumma and Charnley, 2011) (see §1.3 for further details on volatiles in coma).

The dust component of the coma is formed as consequence of direct sublimation of nucleus ices. During ice sublimation, the dust embedded within is freed and dragged out by the expanding gas. The dust motion depends on the three- dimensional gas-dust interactions that take place close to the nucleus surface. In comet 67P/CG, for example, the dust coma was observed since April 2014. Active regions were identified as being mainly in the neck region. When the spacecraft was sufficiently near to localize the active areas, they were associated with jets coming from active pits. The observed nucleus activity formed the major coma feature and it showed a “daily” variability due to changing of insolation conditions as the nucleus rotated (Sierks et al., 2015). As mentioned above, the direct sublimation process from the external layers of the nucleus is the dominant source of coma, however the nucleus alone can not be responsible for all the observed gas in the coma. An additional extended source is likely due to icy grains, which are ejected into the coma and once heated by the solar radiation they are responsible for the increase of subliming material in the coma.

1.2 Cometary reservoirs and classifications

Comets are stored in two main reservoirs: the Oort cloud and the Kuiper belt (Figure 4). The presence of a distant comet cloud surrounding the solar system was inferred by Jan Hendrick Oort in 1950 through simulation and observations of comets. This reservoir is thought as a huge spherical cloud of planetesimals (~ many billions of bodies) orbiting around 50,000 au of distance from the Sun. According to the "*Nice*" model[5] (Morbidelli, 2008), Oort cloud comets were formed in inner regions of the solar system nearby the giant planets. When the Oort cloud was still empty the giant planets neighborhoods were full of icy planetesimals, remnants of the primordial proto-planetary disk. The scattering action of giant planets dispersed icy planetesimals remnants of primordial proto-planetary disk throughout the solar system. The Nice model predicts that comets ejected from the outer disk beyond heliocentric distance R_h ~15 au later entered both the Oort cloud and the Kuiper belt. Some objects moved in eccentric orbits with large semi-major axis, but with perihelion distance still in the planetary region. Some others reached a semi-major axis about 10,000 au, these objects started to feel the effects of a galactic tide, modifying their orbits and raising their perihelia from the giant planets' region (Morbidelli et al., 2005). Simulations showed that the planetesimals' distribution was randomized, giving rise to spherical structure of the Oort cloud as inferred from observations (Morbidelli, 2008). The Oort cloud is, thus, the reservoir of long-period comets (LPC) that are periodically

---

[5] The Nice model assumes an initial configuration of the giant planets more compact than the current one; they are assumed to have formed within 15 AU of the Sun. The model retrieves the giant planets' current orbits through a dynamical instability phase. After ~700 Myr, Jupiter and Saturn crossed their mutual 1:2 mean motion resonance. This event triggered a global instability leading to a reorganization of the outer solar system, producing a violent scattering its inhabitants throughout the solar system.

perturbed from their orbits by gravitational attractions of a crossing star, giant molecular cloud interactions, or tidal forces of the Milky Way.

Comets can be scattered outside or inside the solar system, so the bodies that visit for the first time the internal region of the solar system are usually called dynamically "*new*" comets. Proceeding in their approach into the solar system they could encounter the planets, in particular Jupiter, and their orbits could be again perturbed. Due to Jupiter's gravitational force, the comets could leave the solar system entirely or could be injected inward toward the inner part of the solar system, and be seen as long period comets.

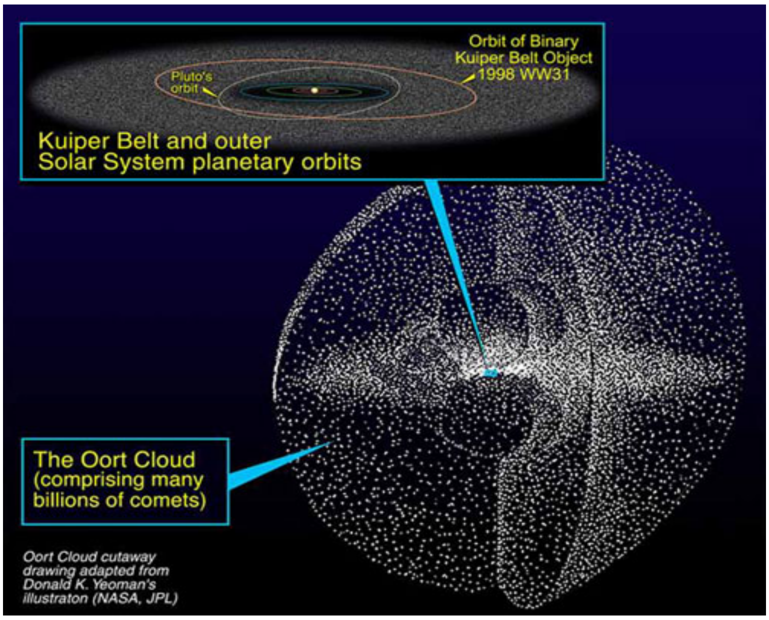

Figure 4.
Representation of the two reservoirs of comets: the Oort cloud and the Kuiper belt. The graphic shows the huge size and large distance (~50,000 au) of the Oort cloud from the Sun, with respect to the Kuiper belt and inner solar system dimensions.

The Kuiper belt is the second reservoir of comets residing beyond Neptune. This area stores the so-called Kuiper Belt Objects (KBO) or the Trans-Neptunian Objects (TNO). The astronomers Kenneth Edgeworth and Gerard Peter Kuiper were the first to formulate the idea that a belt reservoir of comets should be present at the extreme edge of the outer planets' region. To explain comets with low inclinations and short period (SPC), Kuiper asserted the existence of another reservoir of planetesimals beyond Neptune, at R_h ~20 au. Although orbits are now quantified for more than 1000 objects, and millions are estimated to exist, the KBOs were difficult to detect due to their small size and low albedo. The first

Kuiper belt object was indeed discovered in 1992 (Jewitt and Luu, 1993; Jewitt et al., 1992).

Comets of Kuiper belt are classified in three dynamical classes: the Resonant Objects, the Classical Objects and the Scattered Disk (Gladman, 2005). The Resonant Objects are located in some mean-motion resonance with Neptune. They are mostly present in the 3:2 resonance zone, with semi-major axis of about 39 au, with Pluto as the most well known. The Classical Objects are objects with nearly circular or quite eccentric orbits that are not in resonance with Neptune. Their orbital semi-major axis range is between 30 - 50 au. Due to their relatively low eccentricity they always stay away from Neptune, even at perihelion. Thus, they are considered as objects that best represent the remnants of the solar nebula accretion disk. The Scattered Disk Objects are objects with very eccentric and inclined orbits. They have perihelia at 30 au, thus close to Neptune and they weakly interact with it. Other objects are found that do not belong to any of these three categories. These objects have semi-major axes larger than 50 au and are on highly eccentric orbits. They are called extended or scattered disk objects (Morbidelli, 2008). However, the dynamical structure of the Kuiper belt presents characteristics that are much more complex than expected. In fact, the gravitational influence of Neptune and other giant planets is not sufficient to take into account for the observed dynamical structure, especially for objects with high orbital eccentricities and inclinations.

Apparently-active bodies were observed also in the main asteroid belt between Mars and Jupiter leading to the possible existence of a third reservoir of icy bodies ("Main Belt Comets" or "Active Asteroids") however, their composition and activity is still not well known (Jewitt, 2012).

Historically comets were classified by their dynamical properties in short period comets ($P < 200$ yr) and long period comets ($P > 200$ yr). Furthermore, comets characterized by a period shorter than 20 yr or by a period longer than 20 yr were classified as Jupiter family comets or Halley type comets respectively (Morbidelli, 2005). Nonetheless, comets could change their semi-major axis due to the interaction with giant planets that could be responsible for change in their period and classification within their life-time. Levison, (1996) introduced a classification of comets based on a parameter that remains relatively unchanged during a comet's dynamical evolution: the Tisserand parameter[6], hereafter T_j. According to Levison's classification, comets are divided into two main classes with respect to the value of the Tisserand parameter lesser or grater than 2, the nearly isotropic and the ecliptic comets, respectively. Ecliptic comets are characterized by short periods and low inclinations, so they are likely coming from the Kuiper belt. This class of comets is divided into three other sub-classes: the Jupiter Family comets (JFCs), whose dynamic is completely determined by the interaction with Jupiter, and the Encke type and the Chiron type comets according to whether the semi-major axis is respectively entirely internal or external to Jupiter. The nearly isotopic comets originated mainly from the Oort cloud. These comets are divided into 2 different sub-classes with respect to the assumed orbit during injection into the inner solar system. Comets with semi-major axis $a > 10{,}000$ au are called dynamically new comets because they are entering into the inner part of the solar system for the first time since emplacement in the OC. Comets with semi-major axis axis $a < 10{,}000$ au are defined as returning comets. The returning comets are divided in two sub-classes according with another condition on $a > 40$ au and $a < 40$ au. The first condition classifies the long period comets (LPCs) (or external comets, alternatively), and the second condition defines the Halley type comets (HTCs).

---

[6] The Tisserand parameter is an approximation of the Jacobi constant, which is an invariant of the dynamics of a small body in the framework of the restricted, circular, three-body problem.

1.3 Volatiles in cometary coma

Comets are today located in their reservoirs as result of the dynamical events that occurred during the solar system's evolution. Thus, the chemical composition of comets reflects both the processes that occurred at the primordial stages of solar system formation and their evolution. Moreover, their storage in the different reservoirs perhaps caused them to follow different routes to their current composition. For example, short period comets are subjected to solar radiation more times than long period comets. Cometary nuclei are a mixture of refractory and icy compounds, but ices are more sensitive to the thermal and radiation processes. The main process that leads the formation of volatiles in cometary comae is the direct sublimation of ices from nucleus surface by solar heating. This mechanism, as already introduced in chapter 1.1, produces the "primary" volatiles. Consequently, these molecules can be photo-dissociated or ionized by UV radiation creating a second population of volatiles called "product" species. In Figure 5, a cartoon example of cometary production of volatiles is shown.

Due to their persistence in their reservoirs for almost their entire lives, comets don't modify their original composition. Only their outer layers could undergo thermal evolution, erosion by interstellar grains or altered by cosmic-rays bombardment. The inner part of their nuclei should be un-changed from the primordial composition. Thus, volatiles abundances can provide essential clues to understand the origin and the evolution of the early stages of our proto-solar nebula (Mumma and Charnley, 2011).

Figure 5.
This graphic illustrates cometary activity. Release of parent volatiles (H_2O, CO, CO_2, HCN, CH_3OH and H_2CO) by direct sublimation from ices on nucleus surface is shown together with refractory grains being dragged into the coma by the escaping gas. Multiple channels for forming daughter species by photolysis of parents are also shown

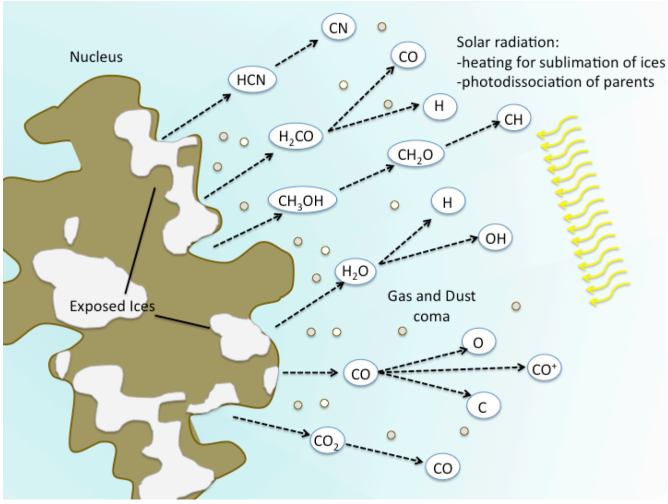

1.3.1 Main parent molecules and product species

A summary of the principal primary species detected in cometary comae and shown in Figure 5 follows:

- Water (H_2O) is the most abundant molecule in cometary comae. Its presence was confirmed around 1970 when its primary products H and OH were found with production rates and spatial distributions that were consistent with their production as daughter species (Weaver et al., 1981). Due to the strong atmospheric telluric absorptions, the fundamental vibrational bands of water near ~2.7 μm could not be detected with ground based observations. These bands were observed for the first time in 1P/Halley with the Kuiper Airbone Observatory (KAO) by (Mumma et al., 1986). However, even if the non-resonant fluorescence water bands (hot-bands) near ~2.7 μm had weaker g-factors, they were observable from the ground because they were not affected by telluric absorption. Hot-band emissions were targeted and detected near ~2 μm in comets C/1991 T2 (Shoemaker-Levy) and 6P/d' Arrest (Mumma et al., 1995) and then systematically in C/1996 B2 (Hyakutake) (Dello Russo et al., 2002). Another spectral region of high interest was near ~4.7 μm where detections of water hot- bands were possible together with the CO (1-0) band. Further discussions on water will be address on Chapters 2, 3 and 5.

- Carbon monoxide (CO) ranges widely in abundance relative to water – it can be the second most abundant molecule in the coma, or only a minor constituent. It was detected for the first time in comet C/1975 West through the resonant fluorescence ($A^1\Pi - X^1\Sigma^+$) band system in the UV near 1550 Å (Feldman and Brune, 1976). These bands were detected in almost all the observed comets in the UV range and only recently, in 2002, other emission bands of the Hopfield-Bridge system near 1075 Å and 1155 Å were detected in comet C/2001 A2 LINEAR opening a new path to study CO at UV wavelengths (Feldman et al., 2002). CO was detected in many comets and relative abundance to water varied between (0.4 – 30) %. The first clear detection of CO at IR wavelengths, near ~4.7 μm, was in comet Hyakutake with CSHELL/NASA-IRTF (DiSanti et al., 2003; Mumma et al., 1996). From the Boltzmann analysis, the rotational temperature and production rate of CO were extrapolated in order to constrain its abundance. The CO detection in eight comets led to an abundance range of about (1 – 24) % with respect to water (Mumma et al., 2003). The range in 23 comets from the Oort cloud (0.4 – 28%) was recently reviewed by (Paganini et al., 2014).
- Carbon dioxide (CO_2) in cometary comae is not accessible from ground-based observatories due to the strong CO_2 atmospheric terrestrial absorptions. The presence of carbon dioxide had long been inferred from the detection of CO_2^+ emissions in the UV, but it was not possible to extract a reliable production rate for CO_2 from those bands. The CO_2 ν_3-band near 4.26 μm was detected for the first time in comet 1P/Halley with the Vega/IKS space mission (Combes et al., 1988), and later with ISO space observatory (Crovisier et al., 1996). The derived CO_2

abundance with respect water was around ~3.5% in comet Halley, ~9% in comet Hartley 2 (Colangeli et al., 1999) and >20% in comet Hale-Bopp (Crovisier et al., 1996). The recent *Akari* infared space observatory surveyed 18 comets in H_2O, CO, and CO_2, and demonstrated that CO_2 was more abundant than CO in most of them (Ootsubo et al., 2012).

- Methanol (CH_3OH) ν_3-band fluorescence emission near ~3.5 μm at low rotational temperature (70K) was suggested for the first time by (Hoban et al., 1991) to explain the detected broad features in the low-resolution spectra of four comets; the band shape in comet Austin was consistent with the modeled P,Q,R branch structure at 70K. Identification of methanol was obtained at 145 GHz in comet C/1989 X1 Austin and C/1990 K1 Levy with the 30-m radio telescope IRAM (Bockelée-Morvan et al., 1991). P, Q and R high-resolution structure of methanol ν_3-band near at ~3.5μm was detected through a high-resolution Keck/NIRSPEC spectra in comets C/1999 H1 Lee and C/1999 S4 LINEAR (Mumma et al., 2001a; 2001b). In 2012, a new line-by-line quantum mechanical fluorescence model for the ν_3-band of methanol was developed (Villanueva et al., 2012a) to perform accurate synthesis of line-by-line spectra for three observed comets C/2001 A2 LINEAR, C/2004 Q2 Machholz and 8P/Tuttle. The new model quantified with high accuracy the rotational temperatures and production rates for the three observed comets and reconciled the retrieved production rates obtained at IR and radio wavelengths for C/2001 A2 LINEAR.
- Cometary formaldehyde (H_2CO) was detected for the first time in comet 1P/Halley with the Giotto NMS/ion-mass spectrometer (Meier et al., 1993). The spatial distribution of formaldehyde showed a behavior different from an expected primary

volatile[7] suggesting the presence of an additional extended source in the coma (see Figure 5). Due to its "daughter" species spatial density and its low abundance, the detection of H_2CO in cometary coma at IR wavelengths by long-slit spectroscopy was difficult. The first quantum-mechanical model for the ν_1 and ν_5 bands near 3.53 μm and 3.62 μm was developed by (Mumma and Reuter, 1989), who also computed the line-by-line IR fluorescence spectrum. Mumma and Reuter 1989 then applied the model to IKS low-resolution spectra of 1P/Halley, showing that H_2CO was an important contributor to the 3.5 μm spectral feature and deriving a production rate and rotational temperature for H_2CO. Recently, (DiSanti et al., 2006) revived the model and applied it to fluorescent emission of formaldehyde in comet C/2002 T7 LINEAR with CSHELL, the high resolving power (~25,000) spectrograph at NASA-IRTF (NASA Infrared Telescope Facility). The observed ν_1 and ν_5 bands near 3.53 μm and 3.62 μm, respectively, represented the first spectrally resolved detection of cometary H_2CO at IR wavelengths.

- Hydrogen cyanide (HCN) is a common parent species in cometary comae and is easily detected from ground based observatories. It was first detected in comet 1P/Halley at 88.6 GHz by several teams (Schloerb et al., 1986). Its first IR detection was in C/1996 B2 (Hyakutake), through the ν_3-band at 3.0 μm (T. Y. Brooke et al., 1996; Magee-Sauer et al., 2002), and later was detected in many other comets (Mumma et al., 2003; 2001a). Its median abundance with respect to water is ~0.2%, however, the spread in abundance ratios ranges from 0.034 ± 0.008% in 6P/d'Arrest to 1.3 ± 0.2% in C/2010 G2 (Hill) (Russo et al., 2009). It once was taken as an H_2O-

---

1. [7] For spherically symmetric release, a primary molecule shows a column density that varies according to the Haser model as $(e^{-r/L})$ /r, where r is the nucleocentric distance projected along the line of sight and L is the molecular scale length. In the approximation of $r \ll L$, the column density has a behavior of 1/r. For a product species the variation of column density with respect to r is much flatter.

substitute when evaluating diversity among relative molecular abundances, but now is recognized to be inappropriate for that purpose. HNC (hydrogen iso-cyanide) is an isomeric form of HCN, with the hydrogen displaced by 180° with respect to the CN radical. It was detected for the first time in comet Hyakutake at 363 GHz (Irvine et al., 1998). The origin of HNC is still being debated. It is the most stable isomer of HCN, suggesting its origin in the natal interstellar cloud core. However, the detections performed in comet Hale-Bopp at different heliocentric distances showed a ratio of HNC/HCN varying from 0.02 at Rh >2.5 au to 0.2 at perihelion, suggesting another production mechanism of HNC in the coma (Biver et al., 1997). Later studies seemed to confirm this strong trend, with HNC/HCN varying linearly with heliocentric distance between 0.5 to 1.2 au in 10 comets; however comet 73P/SW 3 comets diverged significantly from the trend, being lower by a factor of seven than the trend line and challenging the idea that coma chemistry is the sole factor controlling the isomeric ratio (Lis et al., 2008). Regardless, studying the isomeric abundance ratio (HNC/HCN) can provide hints on the competition between chemistry that occurred at the primitive stage of solar system formation and chemical production of HNC in the cometary coma. Recently, a new quantum mechanical fluorescence model for HCN and HNC was developed by (Villanueva et al., 2013). The model describes with high accuracy the complex emission spectrum detected in comet C/2007 W1 Boattini, providing rotational temperatures and production rates with greatly improved limits of confidence compared with previous fluorescence models. Moreover, the model takes into account possible radiative isomerization of HCN to HNC , providing estimations of conversion efficiencies under typical cometary conditions. Additonial tests are needed, and are now enabled by the emerging class of high-resolution IR spectrometers at IRTF, Keck, and E-ELT.

Many cometary molecules observed in a wide range of wavelengths, from UV to visible to IR spectral region, are the "product" species, e.g. radicals (OH, NH, CN, CH, C_2, etc), atoms (NaI, OI, etc) and ions (OH^+, CO^+,CO_2^+ CH^+, etc) (Feldman et al., 2004). These daughter species are not directly sublimating from the nucleus but are produced from parent molecules by photo-dissociation, ionization, chemical reactions in the gas-phase, and destruction of refractory organic grains. The combination of spectroscopic studies of daughter species together with their parent molecules provides complementary information on physical and chemical processes occurred in the cometary coma. In Figure 6, the main channels of water photolytic destruction are shown as an illustrative example. The multiple paths were evaluated at 1au distance from the Sun and depend on the incident photon energy.

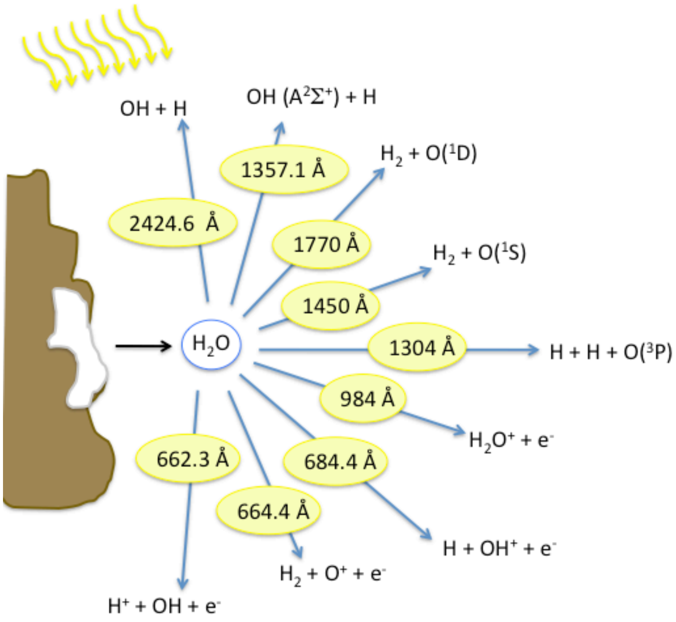

Figure 6.
Production pathways for daughter species by photo-dissociation of water in the cometary coma. The specific pathway depends on the energy of the incident photon, shown here as the threshold wavelength. Efficiencies depend on heliocentric distance and are evaluated at 1 au and described in (Feldman et al., 2004)

1.3.2 Gas production rates, mixing ratios and taxonomy

In order to estimate the relative molecular abundances and characterize the chemical diversity in comets, the measured column densities [mol cm^{-2}] are converted into molecular production rates [mol s^{-1}] that describe the outgassing of the comet. This conversion requires ideally the complete knowledge of the spatial distribution of molecules in the coma. However, under simple assumptions of constant production rate and radial expansion with constant velocity, the Haser model (1957) could be a good description of outgassing of molecules from the nucleus. The density [mol cm^{-3}] is described with the following formula:

$$n(\rho) = \frac{Q}{4\pi v \rho^2}\left(\frac{l_d}{l_p - l_d}\right)\left(e^{-\frac{r_n}{l_p}} - e^{-\frac{r_n}{ld}}\right) \qquad (1)$$

where ρ [cm] is the nucleocentric distance, r_n [cm] is the reduced nucleocentric distance ($r_n = \rho - r_c$, with r_c [cm] comet radius of nucleus). The quantities l_p [cm] and l_d [cm] are respectively the scale lengths for parent and daughter species. Q [mol s^{-1}] is the production rate and v [cm s^{-1}] the gas velocity. In the simplest case in which daughter species are considered as a product of a single step of photo-destruction of parent molecules, *l* is considered $l = v\tau$, where τ is the lifetime of the molecule against destruction.

The column density [mol cm^{-2}] is derived by integration of equation (1) along the line of sight. In reality, the cometary coma is characterized by more complex processes, for example some daughter species can not be produced by a single step of photo-destruction or from a single parent molecule. An observed molecule could come from a chemical pathway of reactions, indeed. Moreover, molecular photo-dissociation is an exothermic process in which the excess of parent released energy is imparted to the product molecules in part as kinetic energy (and often as internal excitation in electronic, vibrational, and/or rotational modes), leading to an increase in velocity for the daughter species (Bockelée-Morvan et al., 2004).

Festou's vectorial model (1981) improved greatly on the Haser model by taking account of the trajectory of molecules, through discrete analytical expressions. In the vectorial model (http://www.boulder.swri.edu/wvm/) daughter species are considered to acquire (as kinetic energy) part of the energy released by the parent after its photo-destruction, allowing them to move with their own velocity in all directions relative to the center-of mass motion (Tozzi and Festou, 1990). Further discussion, emphasizing the CN radical, will be held in Chapters 7 and 8.

The comparison of an outgassing model and the observed spatial distribution of molecules detected in the cometary coma, allows one to retrieve the molecular production rate Q [mol s^{-1}]. Comparing the molecular production rate for a trace gas with that for water defines the abundance *mixing ratio:*

$$R_i = \frac{Q_i}{Q_{H_2O}} \times 100\% \qquad (2)$$

Figure 7 shows an overview of relative abundances of volatiles detected in comets.

(Bockelée-Morvan et al., 2004; Mumma and Charnley, 2011).

The molecular production rate depends on the volatility of the selected species and on the received solar flux, so on the heliocentric distance. Examples of the specie sublimation temperature and the helioecentric distance at which a rapidly rotating black-body reaches that temperature in equilibrium are: $T_{sub}(H_2O)$ =150 K at 3 au, $T_{sub}(CO)$ = 25 K at 100 au, and $T_{sub}(CO_2)$ =80 K at 13 au. The principal species driving the cometary outgassing can change with heliocentric distance, e.g., from CO_2 and CO at large distance to H_2O at small distance. Moreover, the activity of a comet depends on the percentage of active areas on the nucleus surface, their received insolation and their chemical composition and abundance.

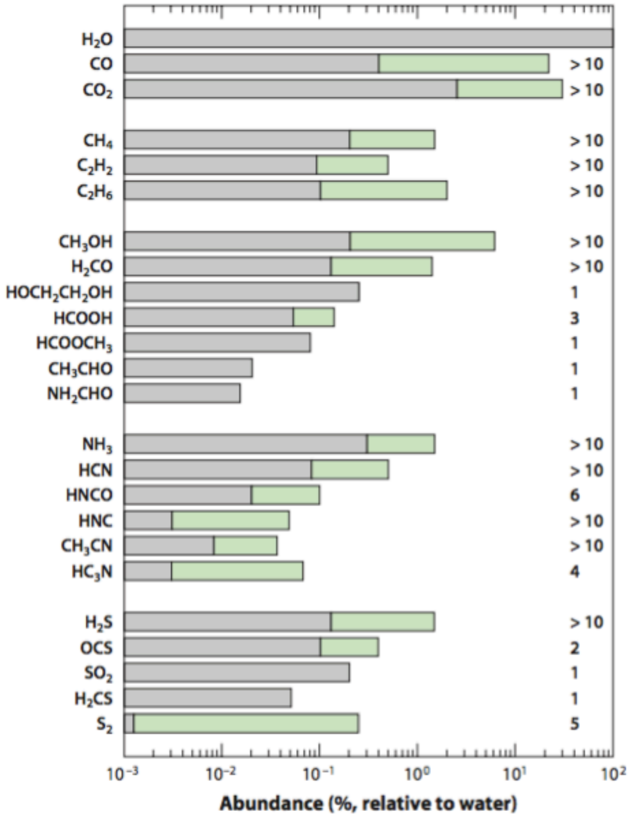

Figure 7.
Percentage abundances relative to water of cometary volatiles detected in spectroscopic surveys. The gray color and the light green color bars represent the minimum and the maximum value of abundances in the measured range. For each molecular species, on the right side the number of comets in which it was detected is shown. The six species labelled with "1" on the right margin were detected only in comet Hale-Bopp, the brightest comet of the past several decades. The graphic is taken from (Mumma and Charnley, 2011)

Determination of molecular production rates with respect to heliocentric distance allows to estimate the evolution of cometary activity. For example, (Biver et al., 1997) measured the evolution of the molecular production rates of many species, such as OH, CO, CH_3OH, H_2S, H_2CO, HCN, CS, CH_3CN, and HNC, with respect to the heliocentric distance in comet Hale-Bopp (the famous "Christmas Tree"). Theoretically, production rates depend on heliocentric distance as R_h^{-2}, if sublimation is dominated by the amount of solar radiation received, but the exponent can assume different values from comet to comet and species to species. For example, (DiSanti et al., 2001) showed that in comet Hale-Bopp the relation fitting the water production rate evolution with respect to R_h had a slope of about 1.88 between 1.49 and 0.93 au: $Q(H_2O) = R_h^{(-1.88 \pm 0.88)}$ while CO production rate showed a slope of 1.76 between 4.10 and 2.02 au: $Q(CO) = R_h^{(-1.76 \pm 0.26)}$.

In the past decades, the increasing performance of astronomical instruments enabled collection of massive databases during compositional surveys. This enhanced our knowledge of cometary composition and molecular abundances, leading scientists to build a new classification of comets based on their chemical composition and relative mixing ratios, instead of dynamical properties (Mumma and Charnley, 2011, Dello Russo et al., 2016). The identification of diversities and similarities, the characterization of organic-rich, super-rich, or depleted nuclei and evaluation of gas-to-dust ratios among comets introduced the concept of different classes of comets, e.g. carbon-rich or -depleted, nitrogen-rich or -depleted, etc., (A'Hearn et al., 1995). The possible connection (or not) between the dynamical and chemical properties is of special interest, and as is the connection between a comet's composition and its forming region vs. evolutionary history.

1.4 Comets origin and connection with solar system formation evolution

The solar system formed from a collapsing cloud of gas and dust (Ehrenfreund and Charnley, 2000). The primordial molecular abundances were defined during the different steps of solar system formation where the gas and dust experienced different physical processes and chemical reactions. The proto-planetary material populating the debris disk was chemically altered according to processes that changed with heliocentric distance. For example, at small distances, inside the inner dust rim, the pure gaseous material was altered by UV solar radiation, and moreover the high temperature allowed thermo-chemical reactions that increased the chemical complexity (Caselli, 2005) (see Figure 8). Outside the inner dust rim many other processes became important, changing both with respect to the heliocentric radial distance and the vertical height within the proto-planetary disk. In the cold mid-plane the low temperatures ($T \leq 30$ K) promoted retention of hydrogen atoms and CO molecules on grain surfaces, leading gas-grain chemistry to assume a fundamental role for enhancing molecular complexity. During this *"freeze-out"* process the grains act as a catalyst for chemical reactions. Moreover this mechanism behaves as a selector for chemical reactions through accreting specific species on grain surfaces, e.g. *"deuteration"* is a process in which the addition of a heavy hydrogen atom becomes the leading process for enhancing molecular complexity (Caselli and Ceccarelli, 2012). Comets are the frozen relicts of this debris disk so they should contain a mixture of this pristine proto-planetary material, and components whose composition should differ according to the place of formation (see Figure 8).

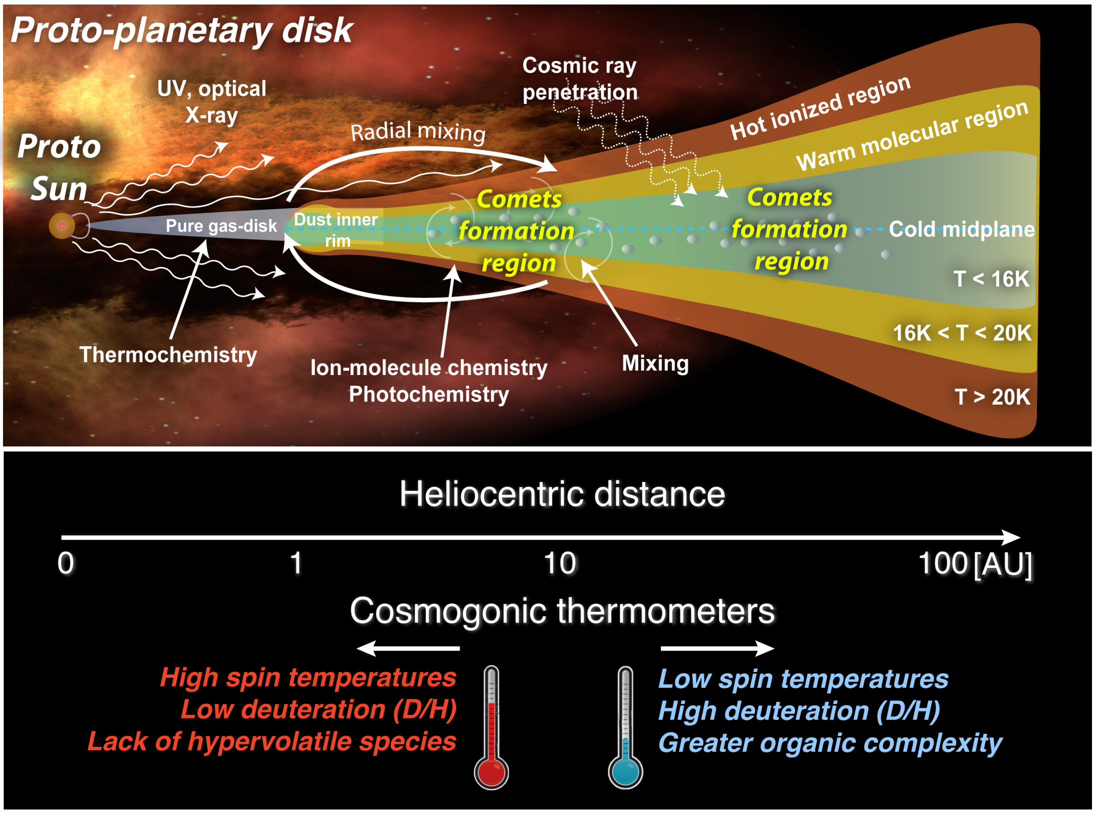

Figure 8. Conceptual view of the proto-planetary disk during the infant stage of its formation. The principal comet-forming regions are shown and some physical processes affecting the conditions of proto-ice formation are indicated. In the lower part of the graphic, the connection linking the distance from the proto-sun with the behavior of cosmogonic thermometers is shown. These are critical points we want to decode.

Moreover, these relicts (cometary nuclei) were stored for millions of years in their reservoirs (the Kuiper belt and the Oort cloud) where they were less thermally processed than were other bodies of the solar system (e.g., asteroids). At those great distances only cosmic rays and interstellar radiation could modify the surface composition (for periodic comets, repeated passages in the inner solar system and even long residence in their short period orbits could have modified the original volatile composition on surfaces) but below the first meter or so their nuclei are thought to preserve information on their original compositions.

The study of cometary nuclei and coma composition – and the further comparison with astrochemical models – are powerful tools for obtaining evidence that inform our understanding solar system formation and evolution. Cosmogonic parameters such as molecular abundance, isotopic ratios and nuclear spin temperatures retrieved from volatiles detected in cometary comae can be indicators of formative temperatures and physical processes that occurred during formative stages of our planetary system. (Further discussion will be given in Chapter 3).

Chapter 2

High resolution spectroscopy of comets in the IR

Spectroscopy in the infrared wavelength range is a powerful tool for studying volatiles in cometary coma. Primary volatiles (native to the nucleus, aka parent molecules) are released into the cometary coma where they can be detected through *solar-pumped fluorescent emission* at infrared wavelengths. Solar radiation excites infrared-active molecules to both fundamental and higher-energy vibrational levels (collisions, scattered light and thermal emission from both grains and nucleus excite vibrational modes only inefficiently). Collisional relaxation is slow in the low-density cometary coma, so the pumped molecules quickly emit at infrared wavelengths through a complicated pathway of fluorescence cascade.

Product species (radicals, atoms and ions produced from parent molecules by photo-dissociation, aka daughter species) can be detected both through fluorescence emission and through *prompt emission*. The excitation process for prompt emission differs from that of fluorescence emission. Radical prompt emission is a mechanism produced by dissociative excitation of parent species. The photo-dissociation of the parents (i.e., H_2O, HCN…) produces daughter species - often in vibrationally excited and rotationally hot states. These excited states are generally unstable and promptly decay to lower energy levels. These levels generally can not be excited by fluorescence pumping of the quiescent daughter specie (rotationally cold) found in the extended coma (Bonev et al., 2004).

Prompt emission lines of a product species are used as tracers for the parent precursors. For example, OH prompt emission lines have spatial distributions similar to that of water, showing a peak intensity in the coma center and a fast decrease with the nucleocentric distance. In contrast, quiescent OH excited in the coma shows a flatter distribution, and even a 'hole' in the innermost coma (Bonev et al., 2004).

Details of fluorescence emission processes are reported in the following section.

2.1 Fluorescence emission processes in cometary coma

As shown in Figure 18 and 19 of Chapter 4 the spectrum of a comet consists of a continuum signal due to solar light reflected by dust particles in the coma (see Figure 6 of Chapter 1), thermal emission from the warm grains ($\lambda > 2\mu m$), and a series of super-imposed emission lines. Depending on the observed spectral region, cometary continuum could be affected by telluric transmittance (i.e., atmospheric absorption). The emission lines are produced by cometary volatile species pumped by sunlight – the fluorescence emission mechanism (Crovisier et al., 1983; Weaver et al., 1984).

According to the Born-Oppenheimer approximation, the accessible energy of a molecule is described by the sum of the electronic, vibrational, and rotational energies – associated respectively with the electrons bonding configuration around the nuclei, the vibrational motion of atomic nuclei within the molecule, and the rotation of the molecule with respect to the molecular axis. In Figure 9 (right side) a schematic example of molecular energy level and transitions is shown.

Rotational spectra are related to transitions that occur between rotational energy levels of a given vibrational level in a specific electronic state, these transitions can be detected at radio wavelengths. Ro-vibrational spectra are formed when transitions take place between rotational levels of different vibrational levels, but in the same electronic state; these transitions can be detected at infrared wavelengths. Finally electronic spectra are defined by transitions between ro-vibrational levels in different electronic states; these transitions can be detected in the UV-visible wavelength range.

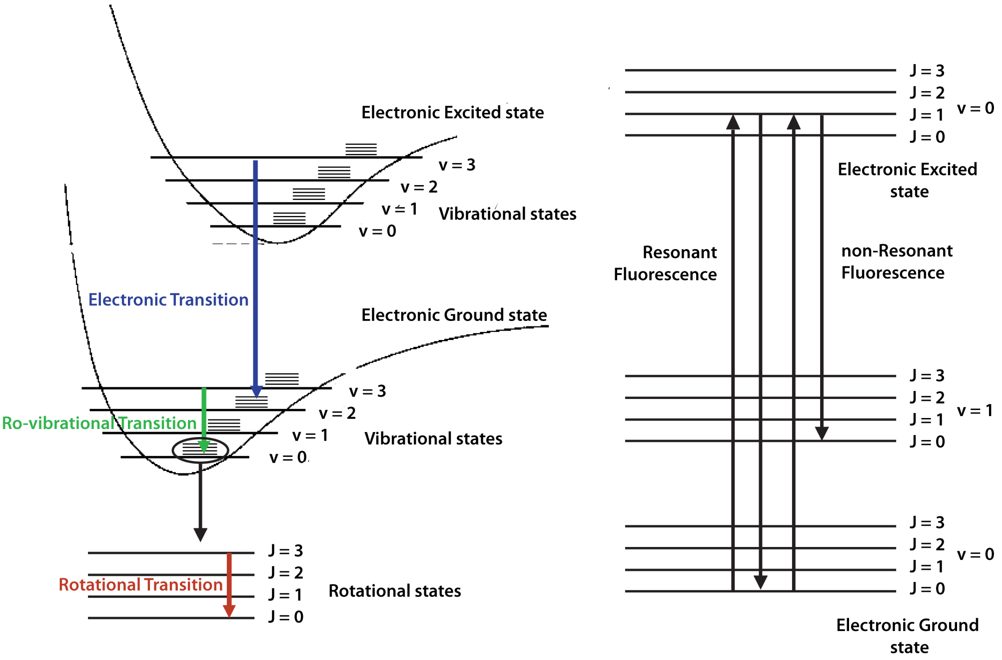

Figure 9.
A simple schematic representation of molecular energy levels is shown. Left: Vibrational and rotational levels of two electronic potential functions, describing the ground and an excited electronic state, are illustrated. Explanatory examples of electronic transitions (blue), ro-vibrational transitions (green) and rotational transitions (red) are shown.
Right: Resonant and non-resonant fluorescence processes are indicated.

According to quantum theory, a transition between two energy levels involves a photon of defined frequency that can be absorbed or emitted by the molecule. In general, the molecule will emit a photon via ***fluorescence*** decay after a precise excitation mechanism promoted the molecule from its initial low energy level (usually the ground state) into a higher energy state. Fluorescence emission can be "resonant" if the molecule returns to the initial energy level or "non-resonant" if the molecule decays to an energy level different from the initial one (Figure 9, left side).

Knowledge of the main excitation and emission processes occurring in cometary coma is essential to quantify the chemical composition of comets from the column densities and production rates of their volatiles, retrieved from the observed ro-vibrational lines.

The excitation processes occurring in cometary comae are led by two principal mechanisms: radiative excitation (at different wavelengths) and/or collisional excitation.

- Radiative vibrational excitation: solar radiation can directly excite fundamental vibrational states of infrared-active gases in comets (Mumma 1982; Yamamoto 1982; Crovisier and Encrenaz 1983; Weaver and Mumma 1984). This was first confirmed by the detection of H_2O ν_3 fundamental band emissions in comet 1P/Halley, but the serendipitous discovery of ν_3 hot-band emission (011-010) demonstrated that combination-band pumping followed by cascade is also important (Mumma et al., 1986; Weaver et al., 1986)[8].
- Radiative electronic excitation: the solar flux is weak at UV wavelengths, leading to a small excitation rate of electronic bands compared to the vibrational excitation rates – even for molecules with strong UV band strengths [e.g., CO ($A^1\Pi$-$X^1\Sigma^+$)]. For example, the total excitation rate of CO near 1500 Angstroms (Tozzi and Feldman, 1998) was about $\sim 10^{-6}$ s^{-1} at heliocentric distance of 1 au, a factor of ~100 smaller than the excitation rate of CO at 4.7 μm by solar pumping (Crovisier et al., 1983). The weak UV fluorescent pumping of diatomic parent molecules explains why the UV emissions are difficult to detect, except in comets with relatively high activity levels. Moreover, in the UV range the solar spectrum is affected by the presence of strong and narrow Fraunhofer absorption lines that introduce significant variations in the fluorescence pumping and consequently in the emission rates depending on comet heliocentric radial velocity (Swings effect) (Bockelée-Morvan

---

[8] Apart from direct solar radiation pumping, the molecular vibrational bands can be radiatively excited by radiation from the nucleus and dust grains, produced by both scattering of solar radiation and by their own emission in the thermal infrared. However, these processes are negligible in the inner coma, except excitation owing to dust thermal emission that can be important in the inner comae of active comets at thermal IR wavelengths [Crovisier and Encrenaz 1983; Weaver and Mumma 1984].

et al., 2004).

- Radiative rotational excitation: Excitation by sunlight at radio wavelengths is negligible due to the weakness of the solar flux at such spectral range. Molecular emission is usually excited by collisions.
- Collisional excitation: in general, collisions with gaseous molecules[9] and/or electrons control the rotational excitation of molecules in the inner coma. Within ~2 au of the Sun, water ice is fully activated and H_2O becomes the most abundant primary gas in the cometary coma. However, at distances greater than ~ 2 au water ice is increasingly stable and by about ~ 4 au more volatile ices dominate gaseous release from the nucleus, with first CO_2 and/or then CO and/or O_2 replacing the role of H_2O at successively larger heliocentric distances. Neutral-neutral collisions can affect the excitation of coma gases, in several ways: (i) collisions can de-excite vibrational levels at nucleocentric distance (r) $\leq$ 20 km. If frequent enough, collisions can kinetically quench vibrationally excited molecules, thereby reducing the radiative emission of vibrational bands near the nucleus surface – but this process is generally unimportant at larger nucleocentric distances (cf. (Crovisier et al., 1983; Weaver et al., 1984); (ii) collisions can excite vibrational levels. This process is generally negligible because of both the relatively high energy of vibrational levels and the low kinetic temperature of the inner coma; (iii) collisions can thermalize rotational levels in the innermost coma. This process is efficient, but for polar species it must compete with radiative relaxation and other effects and so is effective only at sufficiently high collision rates. Owing to their high cross sections with water, collisions with electrons are far more effective and can thermalize water rotational levels even in the intermediate coma, for r $\leq 10^4$ km (Xie and Mumma,

---

[9] Water is inactive at large heliocentric distances, permitting CO and other still volatile gases to dominate the inner coma and control collisional excitation of trace species.

1992a).

The coma is an environment characterized by low temperatures, from ~10 K to 200 K (for comets within 1au), and low molecular densities (from values of about 10^{12} cm^{-3} near to the nucleus surface of a moderately active comet to interplanetary values of about 1 cm^{-3} in the outer coma), so in such conditions, it is plausible to assume that neutral-neutral collisions cannot excite the vibrational levels of molecules for which $E_{vib} >> kT$. However, they can thermalize the rotational population of ground vibrational state, $(n_1n_2n_3) = (000)$, at the kinetic temperature of the gas, so it is possible to assume local thermodynamic equilibrium (LTE) in the ground vibrational state (Xie and Mumma, 1992a).

Further discussion will be provided in Chapter 5 and 7.

2.2 Emissions in the infrared spectral region: Water and organics

Water

Water in comets was detected directly for the first time in December 1985, when ro-vibrational lines of the ν_3 band of water were observed in comet Halley using high dispersion IR spectroscopy from NASA's Kuiper Airborne Observatory (KAO) (Mumma et al., 1986). In March 1986, water was again detected from the KAO (Larson et al., 1986; Weaver et al., 1986) and the IKS infrared spectrometer aboard Vega 1 detected the ν_1 and ν_3 bands of H_2O near 2.7 μm (Combes et al., 1988; 1986). Further water detections were obtained with the moderate resolution spectrometer of the Infrared Space Observatory (ISO) in comet C/1995 O1 (Hale-Bopp) (Crovisier et al., 1996).

Ground-based detections of cometary water were enabled by the advent of CSHELL at the NASA IRTF (Infrared Telescope Facility), the first 2-D array-based cryogenic infrared spectrometer to cover the wavelength region of 1-5.5 μm at high resolving power ($RP = \lambda/\delta\lambda \sim 30{,}000$). Using it, searches for H_2O first emphasized emission lines of the (111-100) vibrational hot-band near 2 μm, and single lines were first detected in C/1991 T2 (Shoemaker-Levy) and 6P/d'Arrest (Mumma et al., 1995). With an improved detector array in 1996, 13 H_2O lines were detected in comet C/1996 B2 (Hyakutake) and water production was quantified (1.7×10^{29} mol s^{-1}), (Mumma et al., 1996); the production rates were later revised slightly as improved fluorescence models were developed (Dello Russo et al., 2002). In the region near 4.7 μm, strong non-resonance fluorescence emissions of water hot bands (100-010) and (001-010) were detected in comet Hyakutake (Mumma et al., 1996) and were later emphasized in C/1995 O1 (Hale-Bopp) (Dello Russo et al., 2000). However, with Hale-Bopp and later comets, attention shifted to H_2O emissions in the 2.9 - 4.7 μm region, where water and other volatile species could be detected simultaneously. This method became a standard one for measuring water production rates in comets.

Today, the high resolution IR spectrograph GIANO mounted on the TNG telescope enables detection of the full 0.9-2.5 μm wavelength range in a single exposure, with resolving power ($\lambda/\delta\lambda$) approaching 50,000. Other high resolution spectrographs are available nowadays, for example iGRINS at the McDonald Observatory covers a portion of this range (H & K bands only, at $\lambda/\delta\lambda$ ~40,000), while iSHELL at NASA IRTF (0.8-5.5 μm, at $\lambda/\delta\lambda$ ~ 80,000) became available for on-sky use in 2016, and similar instruments such as CRIRES+ at the VLT will be commissioned in 2017. GIANO can cover the YJHK IR-bands in a single exposure with very high resolving power, and the results presented here represent the first application of these emerging instruments to a comet.

Organics

The most suitable infrared spectral region to study cometary volatiles is historically the region between 2.5 – 5 μm. This region spans the fundamental bands of the most abundant parent species, allowing development of cometary taxonomies based on primary composition. For example, species such as symmetric hydrocarbons (C_2H_2, C_2H_6, CH_4), simple oxygen-bearing species (H_2CO, CO, CH_3OH) and nitrogen-bearing species (NH_3, HCN), together with water, can be detected through their strong vibrational bands.

Spectrographs with high resolving power (R > 10,000) are essential to resolve the ro-vibrational lines present upon the cometary continuum stemming from sunlight reflected by dust (or from dust thermal emission), all of which are affected by telluric absorptions. As discussed for water, the commissioning of CSHELL/NASA-IRTF in 1992 opened the path to study such molecules at high spectral resolution. Despite the limitations of CSHELL imposed by its modest instantaneous spectral coverage and relatively low sensitivity, the instrument provided fundamental compositional information of comets at small heliocentric distances. Daylight observation capability enabled CSHELL observations on near-Solar comets, a unique capability among IR observatories. The commissioning of NIRSPEC at Keck 2 in 1999 allowed complete spectral surveys of faint comets and sensitive searches for trace species at closer heliocentric distances, advancing the knowledge base in cometary science considerably. The cross-dispersed NIRSPEC provides high spectral resolution combined with larger spectral coverage per order, multi-order sensing, and increased sensitivity due to the 10-m telescope (Keck 2) with respect the 3-m telescope (IRTF) for CSHELL. The advent of NIRSPEC allowed astronomers to obtain valuable information about Jupiter-family comets. Other instruments were commissioned around the year 2000; an important example is CRIRES at the Antu 8-m telescope (ESO-VLT). The instrument, today in upgraded phase, provided the highest spectral resolution available from ground based-observatories (R ~80,000), but lacking cross-dispersion.

Thanks to these instruments the past decades saw major advances in cometary science: the most abundant parent molecules were traced, mixing ratios with respect to water were obtained, nuclear spin temperatures were quantified, D/H was quantified in cometary water, and near nucleus extended sources were explored..

Recently, a detailed analysis of mixing ratios in 30 comets, observed from 1997 to 2013, is reported by (Dello Russo et al., 2016). The mixing ratios with respect to water of principal parent volatiles as CH_3OH, HCN, H_2CO, C_2H_2, C_2H_6 and CO are reported. The comparison of 30 objects conducted by (Dello Russo et al., 2016) showed that Jupiter-family comets are more depleted in volatile species with respect to water, than are long period comets. The mixing ratios of HCN, C_2H_6 and CH_4 showed a positive high correlation, while NH_3, H_2CO and C_2H_2 are moderately correlated each other and not correlated with the other detected species. CO showed a particularly uncorrelated behavior, probably due to its high volatility affecting its thermal evolution. These results are similar to those acquired and reported by the Mumma Team from 1991 onward (DiSanti et al., 2008; Mumma et al., 2003; Mumma and Charnley, 2011; Mumma et al., 1993).

Chapter 3

The European Extremely Large Telescope E-ELT

The European Extremely Large Telescope (E-ELT) is the future giant optical/near infrared ground-based telescope that will be built on top of Cerro Armazones in the Atacama Desert, Chile. The project is led by the European Southern Observatory (ESO) and the facility will begin operations as an integrated part of the Paranal Observatory in 2024 (https://www.eso.org/sci/facilities/eelt/).

The design includes a reflecting telescope with a 39.3-mt diameter segmented primary mirror, a 4.2-mt diameter secondary mirror and an innovative three-mirror design that includes advanced adaptive optics to correct for the turbulent atmosphere, giving exceptional image quality. The primary mirror will be composed of 798 hexagonal segments, each 1.45 meters across and 50 mm thick. A special correcting mirror in the telescope will be supported by more than 6,000 actuators that can distort its shape a thousand times per second.

The E-ELT telescope will be the largest optical/near infrared telescope in the world and will gather 13 times more light than the largest optical telescopes existing today. Its capability to correct for the atmospheric distortions (i.e., fully adaptive and diffraction-limited) will provide images 16 times sharper than those from the Hubble Space Telescope.

The E-ELT will vastly advance astrophysical knowledge by enabling detailed studies in different astrophysical areas and it will allow addressing many of the most pressing unsolved questions about our Universe.

The two first-light instruments that will be built are: ELT-CAM (MICADO) and ELT-IFU (HARMONI). MICADO is a diffraction-limited near-infrared imager with wavelength coverage from 0.8 to 2.5 μm and FoV of about 1 arcmin with the possibility of long slit spectroscopy with moderate resolving power R~5000-10000.

HARMONI is a single-field near-infrared wide-band integral field spectrograph covering a wavelength range of about 0.47 to 2.45 μm. HARMONI has the possibility to have a FoV from 10.0" x 5.0" to 1.0" to 0.5" and resolving powers of R~4000, 10000, and 20000. Together with these two instruments is included the adaptive optics systems MCAO (MAORY) required to deliver their science cases. The next three instruments proposed are: ELT-MIDIR (METIS), ELT-HIRES and ELT-MOS. These instruments are considered of equal scientific importance. ELT-MIDIR (METIS) will offer imaging, coronography and medium-resolution spectroscopy over the wavelength range from 3 to 19 μm, and high-resolution integral field spectroscopy in L and M bands from 3 to 5 μm. While METIS is well settled in terms of its scientific requirements and instrument concept, the E-ELT science community is still working to confirm the requirements for ELT-HIRES (high-resolution spectrometer), and ELT-MOS (multi-object spectrometer).

3.1 The HIRES spectrograph on E-ELT

High-resolution spectroscopy rapidly expanded in the past twenty years, enabling fundamental progress in most fields of astrophysics and in more general areas of fundamental physics. The huge collecting area of the E-ELT telescope will enable incredible results in the high spectral resolution domain and this capability has been studied since the early phases of the E-ELT program. Interest in the spectral high-resolution domain was focused on two instruments: CODEX, an ultra-stable optical (0.37-0.710 μm) high-resolution (R=120,000) spectrograph and SIMPLE, a Near-IR (0.84-2.5 μm) High Resolution (R=130,000) AO-assisted spectrograph.

Later, one single High Resolution Spectrograph (HIRES) was scheduled to start a phase-A study in 2014. This instrument merges the science cases and technical solutions proposed in the former phase-A studies for CODEX and SIMPLE.

In the following table the top-level technical requirements for HIRES, according to the various science cases, are reported:

Table 1. Top level requirements HIRES/E-ELT

	HR Mode	**MR Mode**	**HR AO-IFU mode**
Resolving Power	100000	10000 – 20000	100000
Numb. of simult. obj.	2 + λ lamp	1 – 10	IFU = 69 spaxel
Spectral coverage (μm)	0.37 – 2.5	0.37 – 2.5	0.37 – 2.5
Aperture on sky per obj	0.76"	0.86"	7 to 120 mas/spaxel
Slicing/dicing	37 fiber/obj	1 fiber/obj	1fiber/spaxel
Physical size each fiber	0.085 mm	0.57 mm	0.085 mm
Projected fiber size on IR detector	2.7 x 1.6 pixels	20 x 11 pixels	2.7 x q.5 pixels
Projected fiber size on VIS detector	5 x 3 pixels	37 x 20 pixels	Not appl.
Accuracy	10 cm s-1	n.a.	10 cm s-1
Stability (over 1 night)	10 cm s-1	n.a.	10 cm s-1
Throughput	> ESPRESSO @VLT	> ESPRESSO @VLT	> ESPRESSO @VLT
Polarimetry	yes	n.a.	n.a.

The light coming from the telescope is split into 4 distinct channel called UBV, RI, YJH and K. The HIRES architecture channels are shown in Figure 10.

Each channel is wavelength distinct and includes several optical interfaces that feed

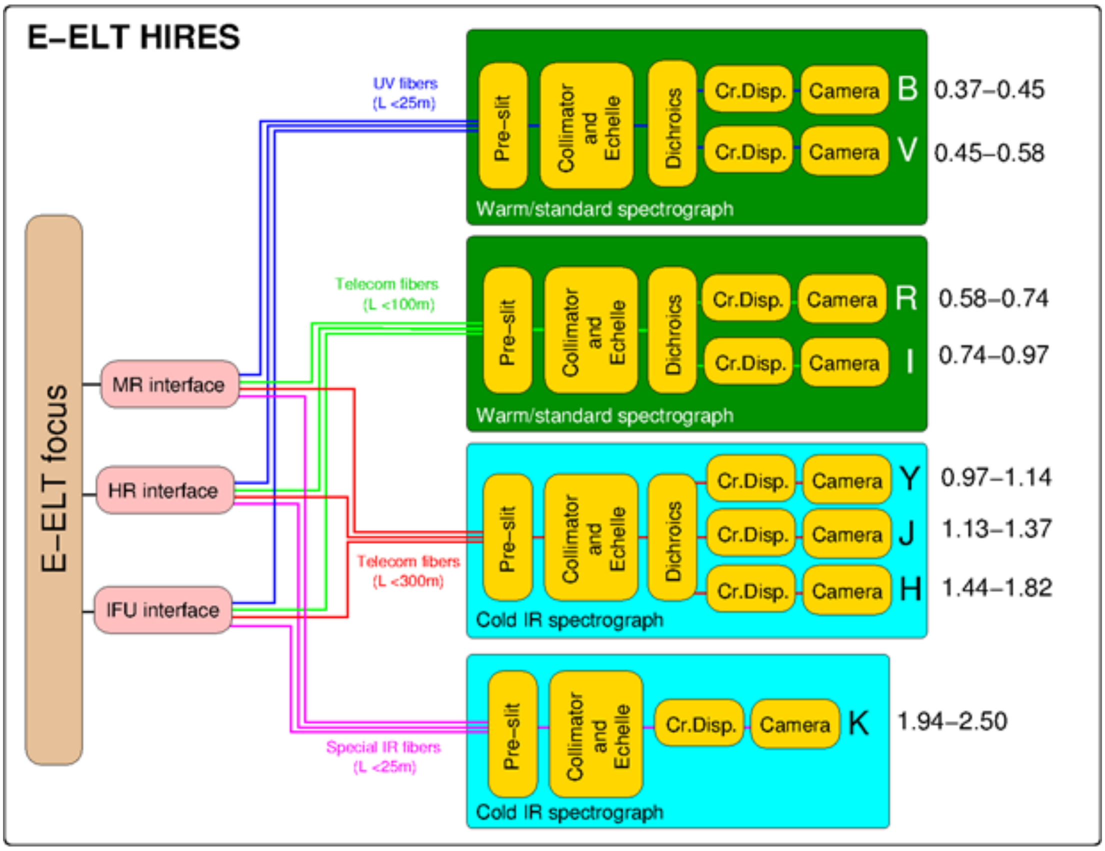

Figure 10. HIRES/E-ELT architecture. The four distinct spectrographs are reported. In the upper part the visible spectrographs (in green) are show. The UB (0.36 – 0.46 μm of spectral range) and the V echelles, (0.46 – 0.6 μm), connected with the blue optimized standard fibers and the R (0.60 – 0.74μm) and I (0.74 – 0.97μm) echelles connected with the red standard fiber are reported. For the near infrared spectrographs the Y (0.97 – 1.13 μm), J (1.15 – 1.37 μm), H (1.46 – 1.81 μm) module and the K (1.95 – 2.48 μm) module connected with special IR fibers are shown.

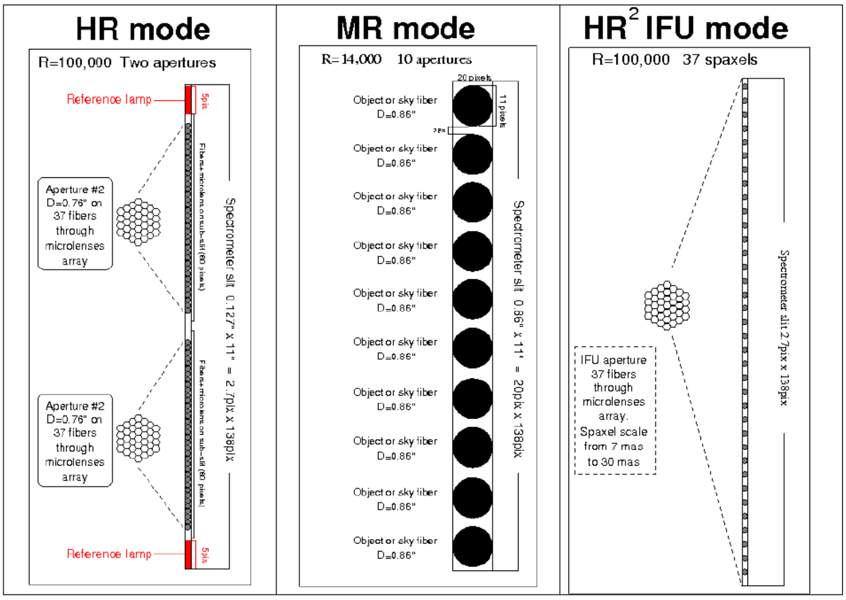

Figure 11. Schematic configuration of the 3 observing modes of HIRES-ELT. The left panel shows the HR mode, the middle panel describes the MR mode and the right panel reports the HR^2 IFU mode.

(through groups of fibers) a specific spectrograph module. Each telescope-interface and fiber bundle corresponds to an observing mode. All spectrometer modules have a fixed configuration, i.e. no moving parts. They include a series of parallel entrance slits, each generated from a separate set of fibers that discriminates the observing mode. The three basic observing modes are: HR mode, MR mode and HR^2 IFU mode. They are related to the top level requirements reported in Table 1 and are shown in Figure 11.

The HR mode consists of two apertures of 0.76" diameter on sky that include a bundle of 35 fibers for each aperture with resolving power of about 100000. The MR mode is composed by 10 fibers of 0.86" of diameter and resolving power from 10000 to 20000. With this mode, it will be possible to observe from 1 to 10 distinct objects. Finally the HR^2 IFU mode consist in an aperture from 7 mas to 120 mas composed by 69 fibers and resolving power of 100000.

3.1.1 HIRES/E-ELT and other present and future competitors

An extremely large telescope project competitor of E-ELT is the TMT (Thirty Meter Telescope). The TMT will be equipped with NIRES, a high-resolution echelle spectrograph covering the 1-5 μm with resolving power of about 100,000. Despite the new generation large telescope projects, other future high-resolution competitor spectrographs mounted on smaller telescopes are iSHELL/NASA-IRTF and CRIRES+/VLT. An upgrade for NIRSPEC/Keck is also expected.

In Figure 15 a and 15 b a comparison of resolving power and collecting area for nine spectrographs available now and in the next future are reported. Before 2017, and after the CRIRES removal from UT1 at ESO VLT in 2014, GIANO at INAF-TNG was one of the spectrographs available with high resolving power (50,000) able to detect the detailed structure of molecular ro-vibrational emissions. The other instruments available (CSHELL, NIRSPEC, and MIRADAS) have lower resolving power than GIANO. The advent of next generation spectrographs (iSHELL, CRIRES+, NIRSPEC-2, and HIRES) will provide a leap in resolving power, from 50,000 to 80,000-100,000 promoting the identification of hyper-fine structure of emission lines and vibrational bands.

In addition to the resolving power of the spectrograph, the collecting area of the telescope is another fundamental parameter connected with the light gathering power. Before the advent of the new extremely large telescope as E-ETL and TMT, the Keck 2 and the GTC (Gran Telescopio Canarias) were the two biggest telescopes available, each with a collecting area of about 85 m^2.

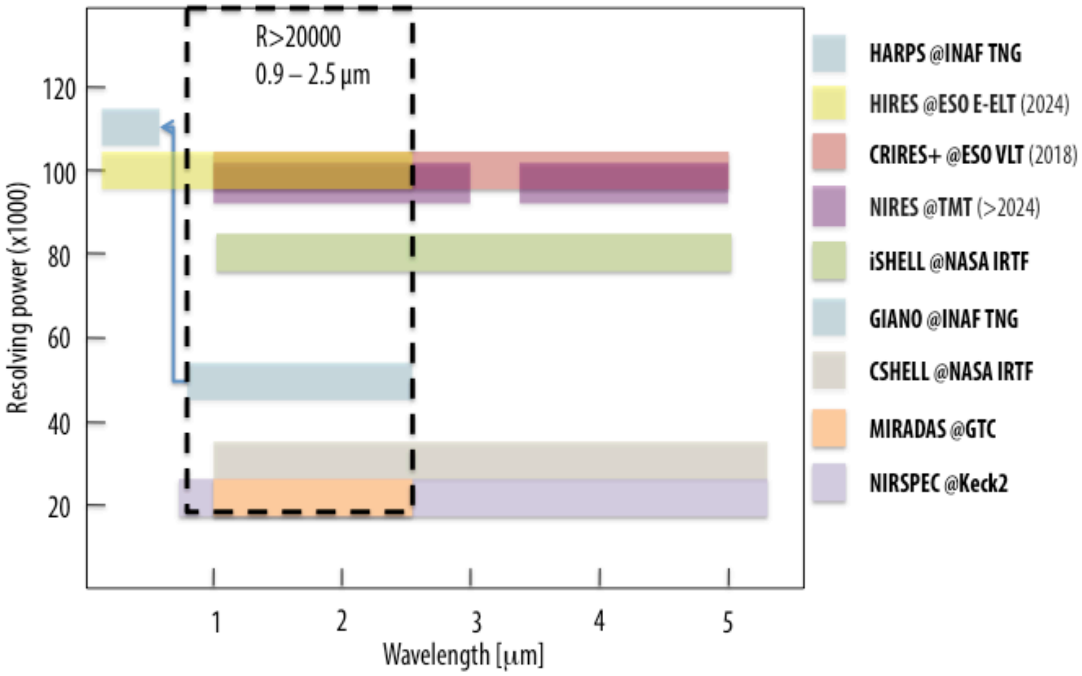

Figure 15 a.
Present and future scenario of high-resolution spectrographs$^{(c)}$. The graph reports some of the high-resolution spectrographs available now and in the near future. The wavelength coverage [µm] is shown on the x-axis and the instrument resolving power Rx1000 on the y-axis. The selected instruments are listed on the right side of the graph and the future instruments report the expecting starting year. The dotted area between 0.9 – 2.5 µm and with R> 20,000 is highlighted to compare the performances of HIRES with respect the other competitor instruments covering the same spectral region. (See also Figure 15 b)

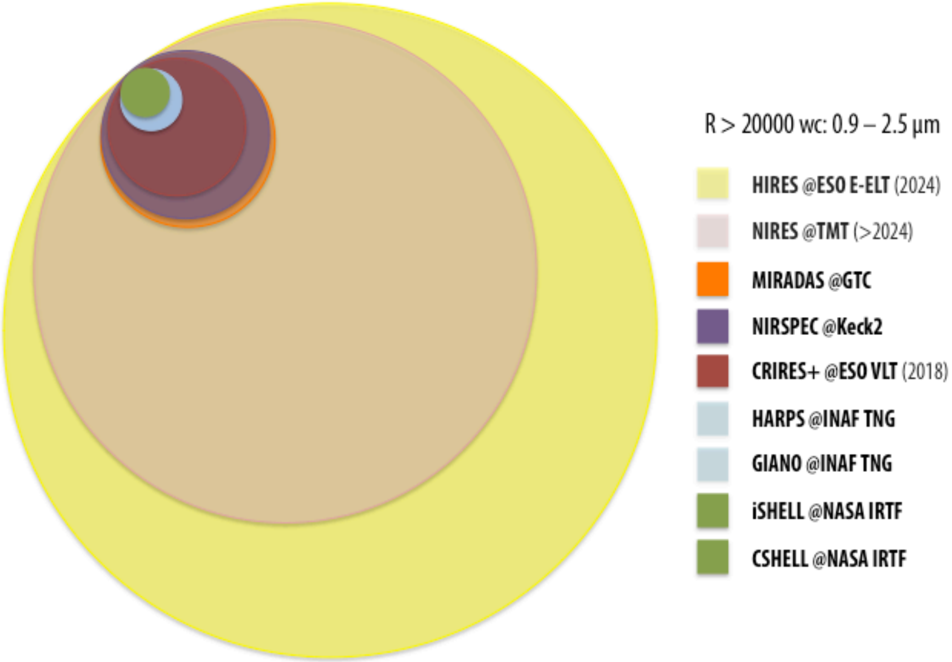

Figure 15 b.
Comparison among the present and the future collective area of telescopes hosting the high resolution spectrographs(c) listed in Figure 15 a. Note that CSHELL has been decommissioned. It is reported for comparison due to its important contribution.
(c)
HIRES @ESO E-ELT, D= 39 m, Wavelength Coverage: 0.3-2.5µm, Spectral resolution: 100,000
NIRES @TMT, D= 30 m, Wavelength Coverage: 1-5µm, Spectral resolution: 100,000
CRIRES+ @ESO VLT, D= 8.2 m, Wavelength Coverage: 1 - 5.3 µm, Spectral resolution: 100,000
GIARPS (GIANO + HARPS) @INAF TNG, D= 3.6 m, Wavelength Coverage: 0.9 - 2.5 µm (GIANO) 0.3 – 0.69 µm (HARPS) , Spectral resolution: 50,000 (GIANO) + 115,000 (HARPS)
iSHELL @NASA IRTF, D= 3.0 m, Wavelength Coverage: ~1 - 5 µm , Spectral resolution: 80,000
CSHELL @NASA IRTF, D= 3.0 m, Wavelength Coverage: ~1 - 5 µm , Spectral resolution: 30,000
MIRADAS @GTC, D= 10.4 m, Wavelength Coverage: 1 – 2.5 µm , Spectral resolution: 20,000
NIRSPEC @KECK 2, D= 10 m, Wavelength Coverage: 0.9 – 5.5 µm Spectral resolution: 20,000

The E-ELT primary mirror diameter will be 39-mt, so about 1000 m^2 of photon-collecting area, while the size of the TMT telescope will be about 30-mt of diameter, so ~650 m^2 of collecting area. The E-ELT collecting area will be almost one and half times larger than TMT. Moreover the E-ELT spatial resolution at diffraction limit will be 30% better than TMT-HIRES. The difference is almost the same between an 8-mt telescope and a 6-mt telescope, but with the new system of adaptive optics (MAORY) it will become even more decisive. The TMT telescope will have a FOV of 20 arcmin with plate scale of 2 arcsec/mm on the sky, covering a large field of view, while in comparison the E-ELT telescope will have a field of view of 10 arcmin with a plate scale of about 3.2 arcsec/mm on the sky. Despite the smaller field of view, the E-ELT telescope outperforms its competitors in collecting area and spatial resolution. Competitors, e.g. the TMT, will undoubtedly make important discoveries in many science fields, however the E-ELT surpasses them in collecting area and spatial resolution.

As it is possible to note from Figure 15a and 15b, the combination of HIRES spectrograph and E-ELT telescope performances will offer the highest spectral resolution and highest collecting area ever achieved.

3.2 The Science Case for HIRES spectrograph on E-ELT.

In the past 20 years, the 3-5 μm spectral region was largely investigated with previous instruments, e.g. NIRSPEC/Keck2, CRIRES/VLT, and CSHELL/NASA-IRTF, but in the near future it will be possible to strongly investigate wider and complementary spectral regions at improved spectral resolutions (e.g. $\lambda/\delta\lambda \sim 70{,}000$ - 100,000). iSHELL/IRTF began scheduled observing in Ocotber 2016.

Although the 3-5 μm spectral region samples most of the biologically important volatile species (e.g., H_2O, HDO, CO, HCN, H_2CO, CH_3OH, CH_4, C_2H_2, C_2H_4, C_2H_6, and NH_3), the 0.9 – 2.5 μm spectral region is an interesting complementary region to study cometary parent volatiles and product species. In the J-, H-, and K-bands, the red-system of radical CN (whose origin is still not clear, see further discussion on Chapter 7), water hot-bands and C_2 emissions are present and were detected, moreover emission lines of singlet-O_2 are expected. The L- and M- bands were carefully studied with previous high-resolution spectrographs giving precious hints on cometary compositions and mixing ratios. However, the higher thermal and cometary background imposes sensitivity limits on the 3-5 μm spectral region, while the 1-2.5 μm spectral window offers lower background and complementary molecular systems. The higher thermal background brings increased stochastic noise to the evaluation of SNR per line. In the 1–2.5 μm spectral region, the combination of a lower background and the high resolving power permits detection of many cometary emission lines at high sensitivity.

In preparation for the new high-resolution spectrographs and HIRES/E-ELT, we recently performed the first high-resolution spectral survey of comets in the 0.9- 2.5-μm range with GIANO/TNG, targeting C/2014 Q2 (Lovejoy), C/2013 X1 (Panstarrs), and C/2013 US10 (Catalina) (future observations are also expected). We detected eight ro-vibrational bands of H_2O (six for the first time) near 1.4 μm and 2 μm, strong emission from the red-system of CN near 1.1 μm, and many other emission lines whose precursors are now being identified (Faggi et al., 2016a; 2016b). The capability to cover with a single exposure the YJHK bands makes GIANO unique. The limits encountered with GIANO due to the smaller resolving power (RP ~50,000) and reduced collecting area (~ 10 m^2) – with respect to HIRES (RP~100,000 and area ~ 1200 m^2) – allow us to predict what can be achieved with a such powerful instrument in cometary science. The observations performed with GIANO established an understanding of the observing limits, empowering us to plan future studies with the next generation of spectrographs.

3.2.1 Comets and the solar system evolution: the origin of Earth's water and organics.

Our knowledge about the infant stages of our proto-planetary system is fragmentary, but cometary nuclei retain the least processed material from that era. The current properties of this material reflect the temperature, composition and processes that occurred during its formation, thus its study is fundamental to advance understanding of the planetary system’s formative phase. According to the *Nice* dynamical model (Gomes et al., 2005; Morbidelli and Rickman, 2015), introduced in Chapter 1.2, comets formed in two regions of the proto-planetary disk: between R_h ~5 and 15 au and beyond ~20 au.

The icy nuclei were subsequently dispersed due to dynamical instabilities among the giant planets, populating both the Oort cloud (OC) and the Kuiper belt (KB) reservoirs (but perhaps in different proportions (Eberhardt et al., 1995; Gladman and Chan, 2006; Morbidelli, 2008). So, the natural question that scientists ask is: do comets in the different dynamical families (JFCs, LPCs, HTCs) show distinct evidence of cosmogonic differences (isotopic ratios, spin temperatures and molecular abundances), as expected if this process endowed the KB and OC with bodies from both the inner and outer regions, but in different proportions?

The search for water and organics in different astrophysical environments (e.g., pre-stellar core, hot-core, hot-corinos, proto-planetary disks, planetesimals, exoplanet atmospheres, galaxies) and the study of them across the entire electromagnetic spectrum is one of the most challenging and interesting topics of astronomy. The importance of studying water and organic molecules is related to their biological relevance.

The chemical and physical properties of water were essential to the emergence of life on Earth; living organisms need a medium in which molecules can dissolve and chemical reactions can take place, and water is the universal polar solvent. Favorable water properties – such as high heat capacity, high latent heat, and the lower density in solid state than liquid state – facilitated the formation and persistence of life on Earth. Moreover, the definition of the circumstellar habitable zone is related to the mobility and stability of water, indeed it is defined as the range of distances from a star for which liquid water can persist on a planet's surface. Thus, Earth's location within the Sun's habitable zone derives from its mean surface temperature being intermediate to the high freezing and the much higher boiling points of water (273K and 373K, respectively, at 1 bar pressure).

The origin of water oceans and pre-biotic organic molecules on Earth (and also the origin of an ancient ocean on Mars (Villanueva et al., 2010), is unsolved. The proto-Earth formed as a dry planet close to the Sun but within the frost line where only metals and silicates can condense to form rocky planetesimals. The Moon's cratering record suggests that an impulsive event occurred 700 million years after planet formation – the so-called Late Heavy Bombardment that was likely triggered by migration of the giant planets. That migration destabilized and scattered planetesimals in the outer disk, causing a huge delivery of icy bodies to the inner part of the solar system (Gomes et al., 2005; Morbidelli, 2008). Many others were delivered to the Kuiper belt and Oort cloud reservoirs.

Water is the most abundant native ice in cometary nuclei, with the aggregate CHON ices (CO_2, CO, O_2) comprising a close second, so they clearly delivered such material, but how much and of what kind (Bockelée-Morvan et al., 2004; Hartogh et al., 2011; Mumma et al., 1993)? Investigations of cosmogonic indicators are necessary to test the hypothesis that small icy bodies delivered water and prebiotic organics to early Earth. Isotopic ratios (e.g., water D/H, $^{13}C/^{12}C$, $^{15}N/^{14}N$), nuclear spin temperatures, and chemical abundances in comets are key to identifying temperatures, molecular abundances and physical processes that occurred 4.6 billion years ago in the comet-forming regions of the proto-planetary disk (Figure 8, Chapter 1.4).

3.2.2 Cosmogonic indicators in comets:

3.2.2.1 Isotopic Ratios

Investigation of isotopic fractionation in water and other organic molecules is a powerful tool for testing the physical conditions in comet-forming regions, and the possible delivery of water and organics to early Earth. For example, the deuterium enrichment (D/H) in a primary volatile is a perdurable parameter linked with the temperature at which cometary ices formed (cf. Meier et al., 1998).

Whether ion-molecule processing or hydrogenation on grains controlled formation of a pre-cometary primary volatile, those that formed in the region between ~5 and 15 au are expected to have a lower deuterium enrichment than those formed beyond ~20 AU. Thus, the present value of the D/H ratio in cometary volatiles acts as a cosmogonic thermometer that indicates the heliocentric distance at which they formed. Comparison of the D/H ratios in water and other species (e.g., CH_4, C_2H_6, HCN, etc.) is essential, considering that some species may have experienced different chemical pathways and evolution in the proto-planetary disk. The ratio of D/H in cometary water has now been measured in fourteen comets (Figure 12a). D/H enrichment in two of three KB comets was consistent with the value in Earth's oceans (VSMOW, $=1.55 \times 10^{-4}$) (Hartogh et al., 2011; Lis et al., 2008), but the value in 67P/Churyumov-Gerasimenko was much higher (3 VSMOW) (Altwegg et al., 2015). Six OC comets showed D/H values twice higher than VSMOW, suggesting that these comets experienced a common birth region, but three other OC comets (C/2012 S1 ISON, 153P/Ikeya-Zhang, C/2009 P1 Garradd) show values approaching VSMOW.

Recently, the apparition of two Oort cloud comets, C/2012 F6 Lemmon around March 2013 and C/2014 Q2 Lovejoy around January 2015, provided two new interesting measurements of D/H ratio in water. The D/H values retrieved in those comets are $(D/H)_{Q2} = (1.4 \pm 0.2) \times 10^{-4}$ and $(D/H)_{F6} = (6.5 \pm 1.6) \times 10^{-4}$. Such D/H values are really different considering that both comets came from the same current reservoir. Excluding a different excitation process of HDO in the coma, this result suggests that they may have formed in different places or at different times in the proto-solar nebula (Biver et al., 2016).

All eleven OC values are consistent with the extreme range measured for KB comets, represented by 103P/Hartley 2 and 67P/Churyumov-Gerasimenko. However, significant systematic errors affect this comparison when individual production rates are based on a single rotational line – as is the case for most (mm and sub-mm) measurements. Future IR measurements with the new high-resolution spectrometers as iSHELL/NASA IRTF, CRIRES+/ESO-VLT and HIRES/E-ELT will remove this uncertainty by quantifying multiple lines of H_2O and HDO simultaneously (for HDO, the proposed multi-line measurements will be the first such at any wavelength!).

Comets retain the isotopic signature of their formation process, so sensitive studies of organic volatiles and their isotopologues can test whether all primary volatiles in a given comet shared a common production process (as did HCN and water in Hale-Bopp (Meier et al., 1998)). The D/H ratio in carbon-rich molecules is not well known in comets; upper limits were obtained only for the D/H ratio in methane in 3 comets: C/2001 Q4 (NEAT)(Kawakita et al., 2006), C/2004 Q2 (Machholz) (Bonev et al., 2009), and C/2007 N3 (Lulin) (Gibb et al., 2012). Comparison of D/H in multiple species will test important ideas concerning uniformity of chemical and dynamical processing in the early solar system.

Together with the deuterium enrichment, isotope enrichments of light elements provide a complementary and essential tool to study origin and chemical evolution of proto-solar nebula. Stable isotope ratios in CHONS, e.g. $^{12}C/^{13}C$, $^{14}N/^{15}N$, $^{16}O/^{18}O$ etc., retrieved in comets are indicators of processes experienced in the primitive stage of proto-ice formation as radiation exposure, temperature, transport, etc. The detection of isotopic species and the retrieval of their isotopic abundance ratios is a challenging task. Measurements of isotopes are difficult because the emissions of such low abundant compounds (i.e., ^{13}CN, $HC^{15}N$, ^{18}OH, etc) are weaker than the "normal" species (i.e., CN, HCN, OH, etc.).

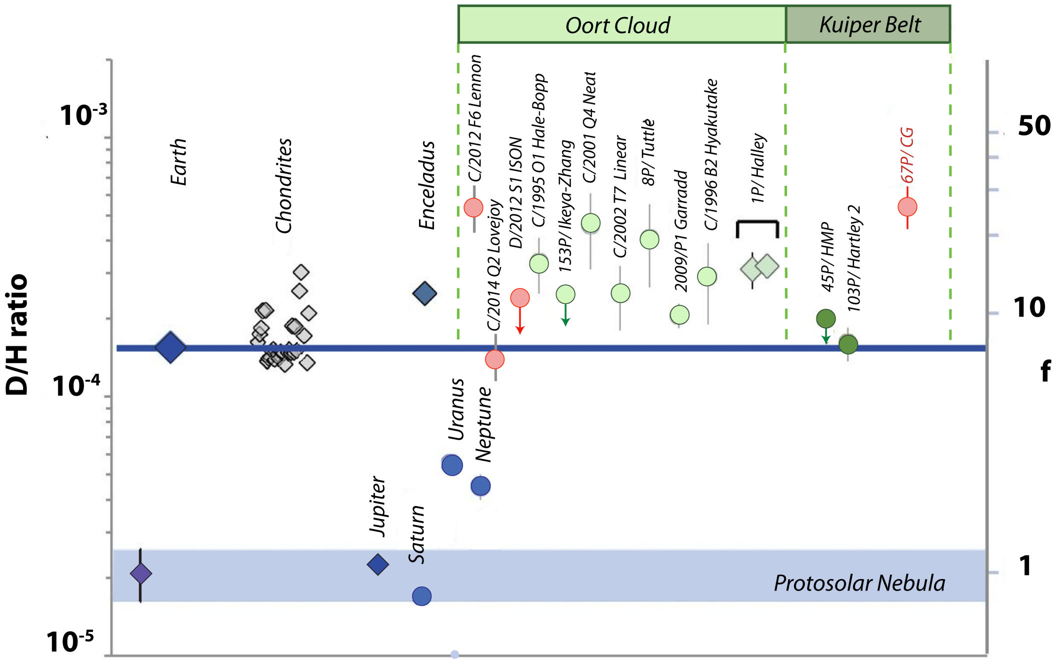

Figure 12a.
D/H ratio in cometary water$^{(a)}$ and across the solar system, with respect to the Proto-solar value (PSV). Earth's ocean water (VSMOW) is enriched ~7-fold with respect to the PSV. Updated from Altwegg et al. 2015, adding the new D/H value obtained in C/2012 S1 ISON, C/2014 Q2 Lovejoy and C/2012 F6 Lemmon.

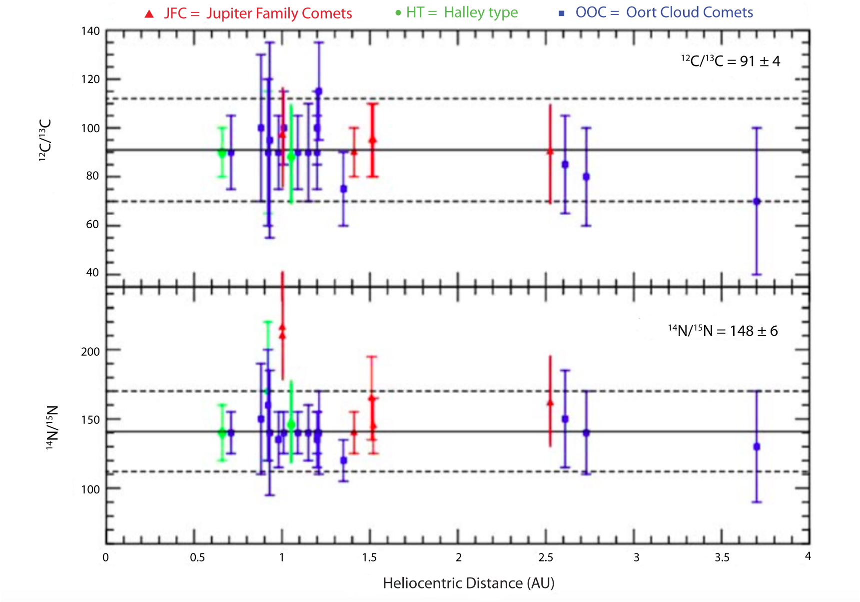

Figure 12b.
Carbon and nitrogen isotopic abundances derived from CN measurements performed in 18 comets of different families.
On the x-axis the heliocentric distance (au) is reported for 24 measurements.
Plot is taken from (Jehin et al., 2009) and (Manfroid et al., 2009).

(a) 12F6 and 14Q2, Biver et al., 2016 IRAM and Odin, 12S1, Gibb et al., 2016 CSHELL@NASA-IRTF; 67P, Altwegg et al. 2015 ROSINA@ROSETTA; 09P1, Bockelée-Morvan et al. 2012 HERSCHEL; 103P, Hartogh et al. 2011 HERSCHEL; 45P, Lis et al. 2013 HERSCHEL; 8P, Villanueva et al. 2008 CRIRES@VLT; 01Q4, Weaver et al. 2004 STIS@HST; 02T7, Weaver et al. 2003 STIS@HST; 95O1, Meier et al. 1998 JCMT; 96B2, Bockelée-Morvan et al. 1998 CSO; 1P, Eberhardt 1995 NMS@GIOTTO.
(b) Blue squares indicate the 11 Oort Cloud Comets.

In the optical wavelengths region isotopic emissions are sometimes blended with lines of the main species, while in the near-IR an accurate subtraction of telluric features is necessary (Jehin et al., 2009). Moreover, high signal to noise ratio and high resolving power are essential to detect them. Finally, retrieval of abundance ratios depends on the accuracy of fluorescence emission models.

Carbon isotopic ratio was measured for the first time in comet 1P/Halley with the ion mass-spectrometer (IMS) on board of Giotto mission. However the simultaneous determination of $^{14}N/^{15}N$ and $^{12}C/^{13}C$ ratios was achieved for the first time in comet Hale-Bopp from sub-millimeter emissions of HCN (Jewitt et al., 1997). The derived values are about $^{14}N/^{15}N = (323 \pm 46)$ and $^{12}C/^{13}C = (111 \pm 12)$ in agreement with the terrestrial value of about 272 and 89 respectively. But further observations on comet Hale-Bopp provided new determinations of the carbon and nitrogen isotopic ratios through the CN violet system (Arpigny et al., 2000). The retrieved $^{12}C/^{13}C$ ratio was consistent with the telluric value and with the previous retrieved value from HCN, while the $^{14}N/^{15}N$ ratio was about ~140, showing a disagreement with respect to the telluric value. In the last decade many measurements were performed in order to understand the interesting low value observed in the nitrogen isotopic ratio from CN. The discrepancy between the values retrieved from CN and HCN was resolved with the observations of comet 17P/Holmes both in optical and radio wavelength ranges (Bockelée-Morvan et al., 2008) giving to HCN the role of parent of CN. This observed excess of nitrogen isotopic abundance in comets with respect to the terrestrial value indicates that comets experienced important fractionation involving N-bearing species during their primitive stage of proto-ice formation (Jehin et al., 2009). By contrast, the homogeneity of carbon isotopic abundance observed in comets (Figure 12b) suggests that the C-bearing volatiles experienced little fractionation (or perhaps none) in the proto-planetary disk (Jehin et al., 2009).

3.2.2.2 Nuclear Spin Isomers and Spin Temperature

Molecules that contain H-atoms in spatially symmetric locations (H_2O, NH_3, C_2H_2, CH_4, etc) have Hamiltonian symmetries associated with exchange of identical nuclei, and thus the total nuclear spin angular momentum is a quantum mechanical constant. Spin isomers show slightly different energy levels; they don't interact radiatively under electric-dipole selection rules and spin-conversion is strictly forbidden, leading to a hypothesis that their relative abundance (and so the nuclear spin temperature, T_{spin}, related to the energy defect in their spin ladders) remains largely unchanged for billions of years (Mumma and Charnley, 2011)[37]. If so, T_{spin} might be a cosmogonic parameter that indicates the formation temperature of that species. Studies of abundance ratios of nuclear spin isomers in cometary primary volatiles can provide valuable hints on comet-forming regions. For example, the ortho-para ratio (OPR) obtained for water and ammonia in six OC comets (Figure 13) implied a common value of T_{spin} (~30K, (Mumma and Charnley, 2011).

From ground-based observatories, investigation of spin isomeric ratios in methane (E/A, A/F) can be obtained only for comets with Doppler shifts > 9 km/s (due to telluric absorptions) and FoM > 0.07 (see Figure 14). Spin isomeric ratios in methane were obtained in four comets (C/2001 Q4 (Neat), C/2004 Q2 (Machholz), C/2007 W1 (Boattini) and C/2007 N3 (Lulin) (ref. 24, and references therein) and three of them showed a common value (T_{spin} ~30K), in agreement with water and ammonia. Does this agreement indicate a common forming region?

A debate on the reliability of OPR as a cosmogonic thermometer, preserving the pristine formation conditions, is ongoing (Shinnaka et al., 2016a). Although the common agreement (T_{spin} ~30K) amongst three chemical species suggests that it is cosmogonic, recent laboratory work suggests that the sublimation process and/or UV irradiation may change the ortho-to-para ratio (OPR) in water (Buntkowsky et al., 2008).

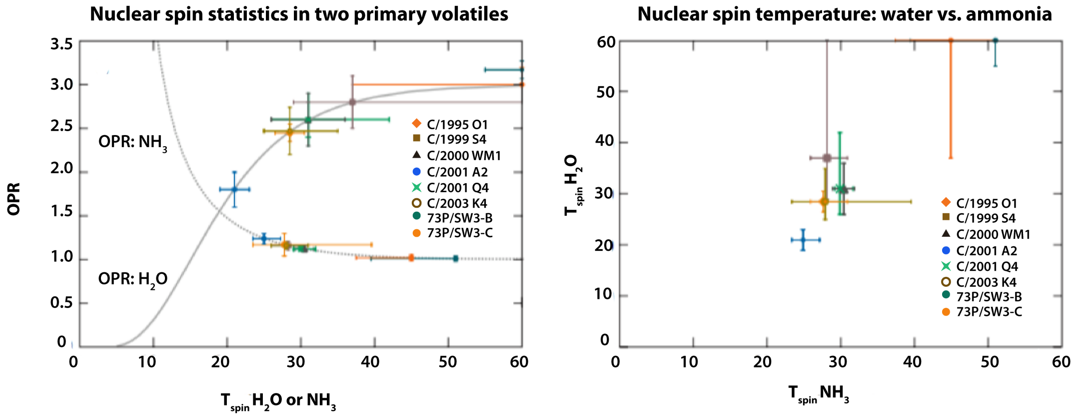

Figure 13. The spin isomeric ratio (OPR) and nuclear spin temperature (T_{spin}) measured for water and ammonia in 8 comets (six from the Oort Cloud and two fragments of the Jupiter family comet 73P/SW-3) of KB origin (Mumma & Charnley 2011 and references therein). Left: The measured OPR values are placed on theoretical curves that connect them to the corresponding nuclear spin temperature (H_2O after Mumma, Weaver & Larson 1987). Right: a comparison of spin temperatures derived for NH_3 and H_2O demonstrates agreement among six OC comets (~30K); the values for KB comet 73P-B/C are consistent with statistical equilibrium. Graphics from Mumma & Charnley, 2011.

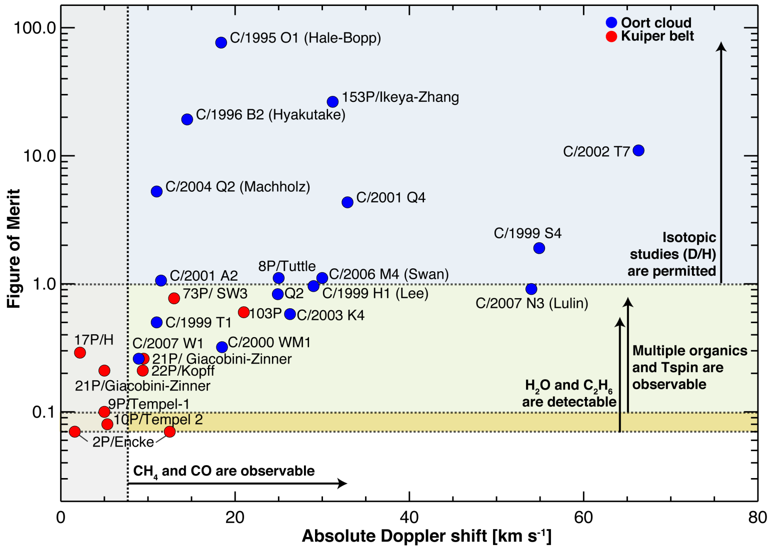

Figure 14.

Detectability of D/H in water and organics. Shown detectability limits are based on measurements obtained in Goddard's comet database observed with (NIRSPEC, CRIRES and CSHELL). Using iSHELL, CRIRES + and HIRES we expect to increase the sensitivity for D/H measurements.

The situation is not yet clear, and moreover spin conversion in ammonia (NH_3) and methane (CH_4) have not been well characterized by laboratory experiment. Will other species show comparable values of T_{spin}? The higher sensitivity and spectral advantages of iSHELL, CRIRES+ and HIRES will enable higher accuracy measurements of T_{spin} in H_2O, NH_3, and CH_4, and extension to T_{spin} in species whose nuclear spin measurement was marginal using last-generation spectrometers (e.g., C_2H_2, H_2CO). Measurements of nuclear spin isomers in a primary volatile (e.g., NH_3) and its putative product species (NH_2) can be achieved simultaneously for the first time, with such high resolution spectrometers, testing their lineal relationship and the origin of NH_2 from a single source.

3.2.2.3 Molecular abundances

Chemical abundances detected in cometary nuclei record the processing experienced in primitive stages of the protoplanetary disk, where the local temperatures and radiation fields (**Fig. 1**) defined conditions that influenced the ultimate chemical complexity of the emerging organic mix. At low temperatures ($T \leq 30$ K), hydrogen atoms are retained on grain surfaces along with CO and methane, permitting gas-grain chemistry to play a fundamental role, with the grain acting as a catalyst for chemical reactions. The mechanism of 'freeze-out' behaves as a selector for accreting hypervolatile species on grain surfaces (e.g., CO, CS, N_2, C_2, C_2H_2) and hydrogen addition then becomes a leading process for enhancing molecular complexity (Charnley and Rodgers, 2008).

With iSHELL, CRIRES + and HIRES we will push the detection limits downward by another factor of three compared with last-generation IR spectrometers, providing more stringent upper limits – or detections. These high-resolution spectrometers will provide simultaneous detections and accurate abundances for the four hydrocarbons (CH_4, C_2H_2, C_2H_4, C_2H_6) to test the gas-grain chemical pathway for carbon reduction ($C_2H_2 : C_2H_4 : C_2H_6$), and of radical CN in order to constrain the HCN problem. Other volatiles will be quantified simultaneously to test the reduction of CO into H_2CO, CH_3OH, and CH_4. The dominant species (H_2O) or its <u>direct</u> proxy (OH prompt emission, OH*) is measured in every instrument setting, permitting highly accurate abundance ratios in every case.

Chapter 4

GIANO/TNG for the present and HIRES/E-ELT for the future: Comet C/2014 Q2 Lovejoy

4.1 Comet C/2014 Q2 Lovejoy

Terry Lovejoy, using a 0.2 meter Schmidt-Cassegrain telescope, discovered this namesake comet on 17th August 2014. Comet C/2014 Q2 Lovejoy (hereafter Lovejoy) is a long period comet (14,035 yrs) with aphelion near 1165 au (1/a=0.0017171 au^{-1}) and perihelion near 1.29035 au (Nakano Note, NK2831). The Tisserand parameter (0.246, with respect to Jupiter) identifies the comet as being from the Oort cloud, and its present (small) value of aphelion corresponds to the inner Oort cloud. It is not known whether comet Lovejoy is now making its first perihelion passage since emplacement in the Oort cloud. During its approach to the Sun, the comet made a close passage to Earth at 0.46885 au on 7th January 2015, and was still favorably placed during our observations. In Figure 16 the orbit of comet C/2014 Lovejoy is shown from different perspectives.

4.2 Observations of comet C/2014 Q2 Lovejoy with GIANO/TNG

We conducted astronomical observations of comet Lovejoy with GIANO, the new near-IR high-resolution spectrograph mounted at the Naysmith-A focus of the TNG (Telescopio Nazionale Galileo) in La Palma, Canary Island, Spain. GIANO provides cross-dispersed echelle spectra at a resolving power of $\lambda/\Delta\lambda \sim 50{,}000$ over the 0.95 – 2.45 μm spectral range, in a single exposure (50 orders). Spectral coverage is complete for wavelengths less than 1.72 μm, i.e. from order 45 to order 81. At longer wavelengths (orders 44 to 32) a few small windows fall outside the detector, making the effective coverage ~75% for the final order (32).

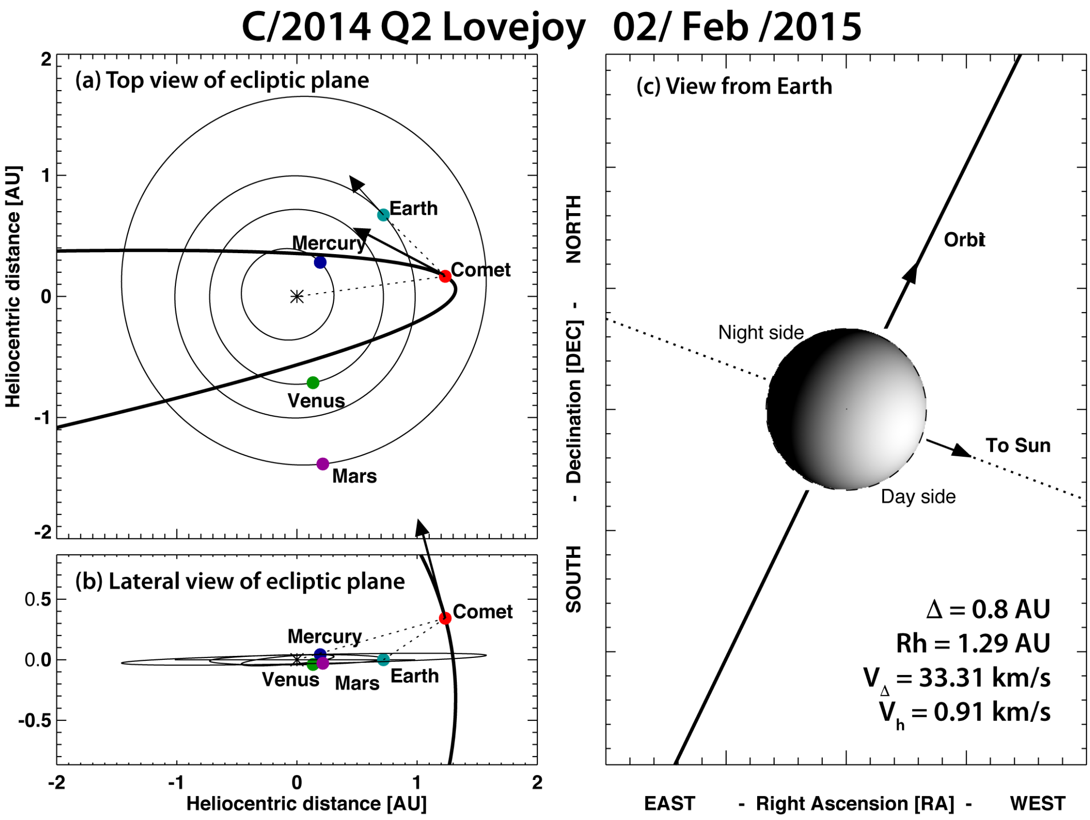

Figure 16
Panel (a) and (b) show the orbit and position of comet C/2014 Q2 Lovejoy, during the observing date, with respect two different perspective views: the top view and the lateral view of the ecliptic plane. In panel (c) the projection as observed from Earth is shown.

The instrument is fed by two IR-transmitting fibers (85 μm diameter) that each cover 1" angular diameter on the sky (~727 km at 1 au). The two fibers are spaced at a fixed separation (centre-to-centre) of about 250 mm, i.e. 3" in the sky plane. GIANO is equipped with a 2048 x 2048 HAWAII-2 PACE detector. Details of the instrument parameters are given in Table 2.

We observed comet Lovejoy near perihelion from 2015 January 31 to 2015 February 02, when the comet was at an heliocentric distance (R_h) of 1.29 au and at a geocentric distance of about 0.8 au (perihelion was UT January 30.07 at R_h = 1.29035 au). The large geocentric

Doppler shift (~33 km/s) shifted cometary emission lines away from their corresponding terrestrial atmospheric absorption lines. Here, we present results obtained from data collected on February 02.

Table 2. GIANO's parameters

Detector, HgCdTe	HAWAII-2 PACE 2048x2048
Pixel size	18 µm, 0.25 arcsec on sky
Gain	2.2 e-/ADU
Readout Noise	5 e-/pixel
Dark Current	0.05 e-/s/pixel
Saturation level	~18000 ADU/pixel
Spectral Coverage	0.95 - 2.45 µm
Spectral Sampling	2 pixels at R~50,000
Spatial Sampling	4 pixels for 1 arcsec fiber

The presence of two fibers allows GIANO to acquire spectra of point astrophysical objects and sky simultaneously; the sky can later be subtracted, thanks to the nodding mode AB. We observed the flux standard star Hip 029216, an O6 star with M_V=7.55, obtaining spectra of both star and sky and we removed sky emissions (mainly lines of OH Meinel bands) from the stellar data by subtracting A and B frames. However, the comet was an extended source and its angular dimension at a geocentric distance of 0.8 au exceeded the fiber spacing (3 arcsec) – the coma overlapped the second fiber. Nodding AB on comet did not allow us to acquire spectra of the object and the sky separately and simultaneously; indeed the A and B beams sampled different areas of the cometary coma when nodded. We adopted the observational strategy shown in Figure 17. By placing the nucleus in (first) the A and (then) the B beams, we acquired simultaneous spectra of the nucleus and two different portions of the coma, that hereafter we term "nucleus", "coma-up " and "*coma-down*" positions.

On Feb. 2, we acquired comet spectra in 5 nod pairs (AB cycles), in each cycle using 300 s of integration time with the nucleus region centered in fiber A and 300 s with it centered in B; later we acquired sky frames (using the same integration time), shifting the telescope by 800 arcsec in right ascension (RA). Calibration lamps (halogen for flat-field and U-Ne for wavelength calibration) and dark frames were also acquired. Observational details are summarized in Table 2.

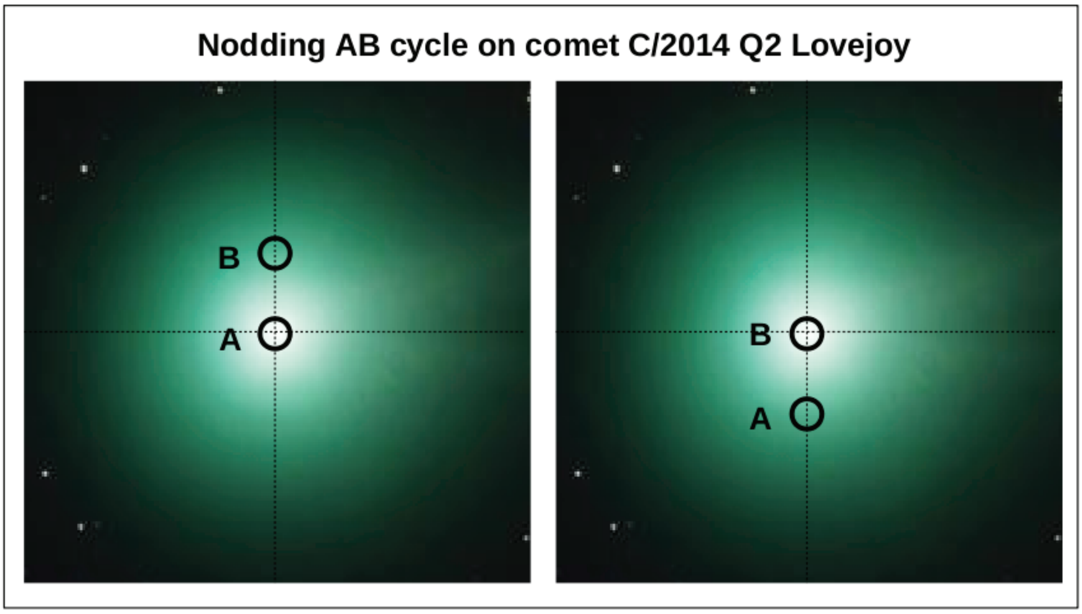

Figure 17. The two panels show the observational setup and nod strategy adopted when observing comet Lovejoy. The 1 arcsec diameter fibers, called A and B, are spaced by 3 arcsec in the sky plane. During the telescope pointing, one fiber is centered on the photometric nucleus of the comet and the second samples the coma 3 arcsec off the nucleus. The nodding permits sampling of three different regions: the upper part of the coma (B fiber on left panel), the nucleus (A fiber on left panel and B fiber on right panel) and the lower part of the coma (A fiber on right panel). The appropriate combination of these samples allowed us to achieve three different positional samplings of the comet.

4.3 Data Reduction and Flux Calibration

A typical GIANO echellogram is shown in Figure 3, Panel A. The echellogram frame grasps 50 orders, from order 32 (at bottom) to order 81 (at top). Each order shows the output of two fibers, so for every order we should expect two arc-shaped tracks.

Table 3. Observing Parameters

Object	Date / Time (UT hr:mn)	Int. Time (s)	N exp.	R_H (au)	Δ (au)	Δ (km/s)
C/2014 Q2 Lovejoy	2015 Jan 31 21:00	300	3 nodding AB	1.29	0.77	32.78
Hip 029216	"	-	-			
Flat	"	60	5			
Sky	"	300	7 stare			
U-Ne Lamp	"	300	1			
Dark	"	300 & 60	10 & 10			
C/2014 Q2 Lovejoy	2015 Feb 01 21:00	300	5 nodding AB	1.29	0.79	33.07
Hip 029216	"	300	3 nodding AB			
Flat	"	60	5			
Sky	"	300	7 stare			
U-Ne Lamp	"	300	1			
Dark	"	300 & 60	10 & 10			
C/2014 Q2 Lovejoy	2015 Feb 02 21:00	300	5 nodding AB	1.29	0.81	33.31
Hip029216	"	300	3 nodding AB			
Flat	"	60	10			
Sky	"	300	11 stare			
U-Ne Lamp	"	300	1			
Dark	"	300 & 60	10 & 10			

However, the output of each fiber is split in two by an image-slicer, so each order is actually composed of four arc-shaped tracks, as seen more clearly in the zoom-panels (Figs. 2-B, 2-C, 2-D).

For clarity, we named "track 1" and "track 2", the two tracks extracted from fiber A and "track 3" and "track 4" the two tracks extracted from fiber B. In total, there are 200 arc-shaped tracks. Each spectral order (group of 4 tracks) contains a part of the spectrum falling inside a wavelength sub-range. Wavelength ranges for each order are listed in Appendix A and a few examples are shown in Figure 18A for clarity (boxes B, C, D). The zoom of box B (Figure 18B; orders 68, 69, 70 and 71) shows fluorescent emission of the 0-0 vibration band of ($A^2\Pi - X^2\Sigma^+$) red-system of radical CN near 1.1 μm. The zooms of box C (Figure 18C; orders 53, 54, 55 and 56) and box D (Figure 18D; orders 39, 40, and 41) show fluorescent emission lines of eight combination bands of H_2O in the 1.4 μm and 2.0 μm wavelength regions, respectively.

The 2-D spectra have been processed using *GIANO tools*, a collection of routines available in any basic installation of IRAF (Image Reduction and Analysis Facility developed by the NOAO), along with some additional ad-hoc scripts developed and adapted by Massi and GIANO team[10] for reducing GIANO spectra.

The routine *GIANO tools* performs bad-pixel correction of flat-field, reference lamp, science, and calibration frames. We first form a pair of mean dark frames (300 s and 60 s) from the individual dark frames taken at 300 s and 60 s (Table 2), and the appropriate mean dark frame is then subtracted from each data frame (comet, star, sky, flat, lamp) to remove dark current levels pixel-by-pixel. *GIANO tools* then divides each dark-corrected lamp, science, and calibration frame by the normalized flat-field frame. Finally, *GIANO tools* extracts and wavelength-calibrates the 200 1-D spectra from each frame.

---

[10] http://www.tng.iac.es/instruments/giano/

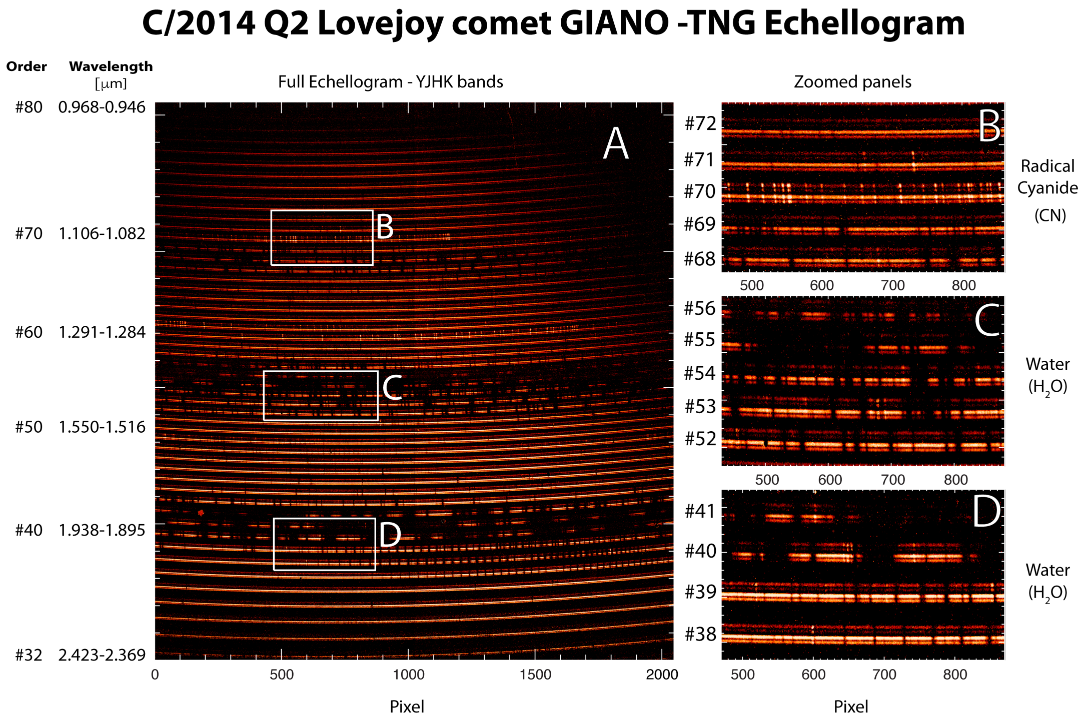

Figure 18.
Panel A: GIANO echellogram of comet Lovejoy acquired on UT 2 February 2015. The panel shows the full echellogram covering 50 orders. Pixel column number (x-axis) and order number and wavelength range (y-axis) are labeled. The order number increases from the bottom (#32) to the top (#80). Wavelength decreases from left to right within each order, and decreases from bottom to top across the echellogram. Each order contains a group of 4 arc-shaped tracks. The upper 2 tracks (3, 4) of each group correspond to image slices of fiber B and the lower 2 tracks (1, 2) to fiber A (slices); in this frame the photometric nucleus of comet was centered on fiber A, where strong cometary continuum is seen in all orders. Absorption features of terrestrial atmospheric gases appear throughout the echellogram (e.g., at the top and bottom of H band), along with many sky emission lines of OH (Meinel bands) that fill the fibers uniformly so are equally bright in tracks 1 & 2 and 3 & 4. We outline regions in which we detected cometary water and radical CN. Cometary H_2O lines are brighter near the nucleus (tracks 1 & 2) but also appear in the off-nucleus position (3 & 4). The lines of radical CN (a product species) are equally bright in tracks 1 & 2 and 3 & 4. Zoomed Panels B-D: Pixel column and order numbers are shown on the x- and y-axis, respectively. Panel B shows zoomed box B from Panel A (near 1.1 µm) in which radical CN and probably water are detected. Panels C and D show the water vibrational bands near 1.4 µm and 2 µm detected in boxes C and D (panel A).

The cleaned 1-D spectra were processed using custom software developed by Villanueva and Faggi to flux-calibrate the GIANO spectra. We flux-calibrated the 200 1-D spectra (extracted from a GIANO echellogram), using an improved version of the advanced GENLN3 terrestrial model (Edwards, 1992; Villanueva et al., 2015). The model synthesizes the transmittance and radiance spectra of Earth's atmosphere across the GIANO spectral range (0.9 - 2.5) µm for the specific observing conditions, allowing us to reproduce and subtract absorption features that are present in the standard star and/or cometary continuum in order to properly calibrate the cometary spectra. The GENLN3 model creates the synthetic spectrum that accounts for telluric lines of H_2O, CO_2, CO, O_3, N_2O, CH_4, O_2, NH_3, and C_2H_6, and convolves the fully resolved synthetic spectra of our atmosphere to the GIANO spectral resolution.

In order to flux-calibrate our spectra we evaluated the expected fluxes [W cm^{-2} μm^{-1} s] of the standard star (Hip 029216) at the top of Earth's atmosphere, based on the calibrated magnitudes of the star in J, H and K center bands; we linearly interpolated the values across all the GIANO spectral range, and we convolved this expected flux with a second order polynomial function representing the efficiency function. Then, we multiplied the convolved synthetic spectrum of Earth's atmosphere (transmittance model) by the flux of the standard star convolved with the polynomial function and we used it to achieve the best fit of the measured standard star spectrum.

The fitting process yields the conversion efficiency (G) from stellar flux density (W cm^{-2} μm^{-1}) to counts (ADU/s) per pixel across each spectral order. The cometary spectra were then calibrated using the obtained conversion efficiencies. In Appendix B, we list the mean value of efficiency functions (G, in units of [W cm^{-2} μm^{-1}]/ ADU s^{-1}) for each track and for each order. After the flux-calibration we fitted the cometary spectra with the terrestrial synthetic atmosphere model in order to properly remove the absorption features affecting the continuum and achieving in this way molecular residual spectra.

Next, the calibrated residual molecular 1-D spectra (and simultaneously the calibrated cometary spectra (before the continuum subtraction) and the modeled continuum spectra) were combined according to the cometary area they sampled (i.e., the nucleus area was sampled alternatively by fiber A (with tracks 1 and 2) and by fiber B (with tracks 3 and 4).

Thus, we combine spectra from tracks 1 and 2 for fiber A with those from tracks 3 and 4 for fiber B to produce a molecular residual spectrum for the nucleus sampled area.

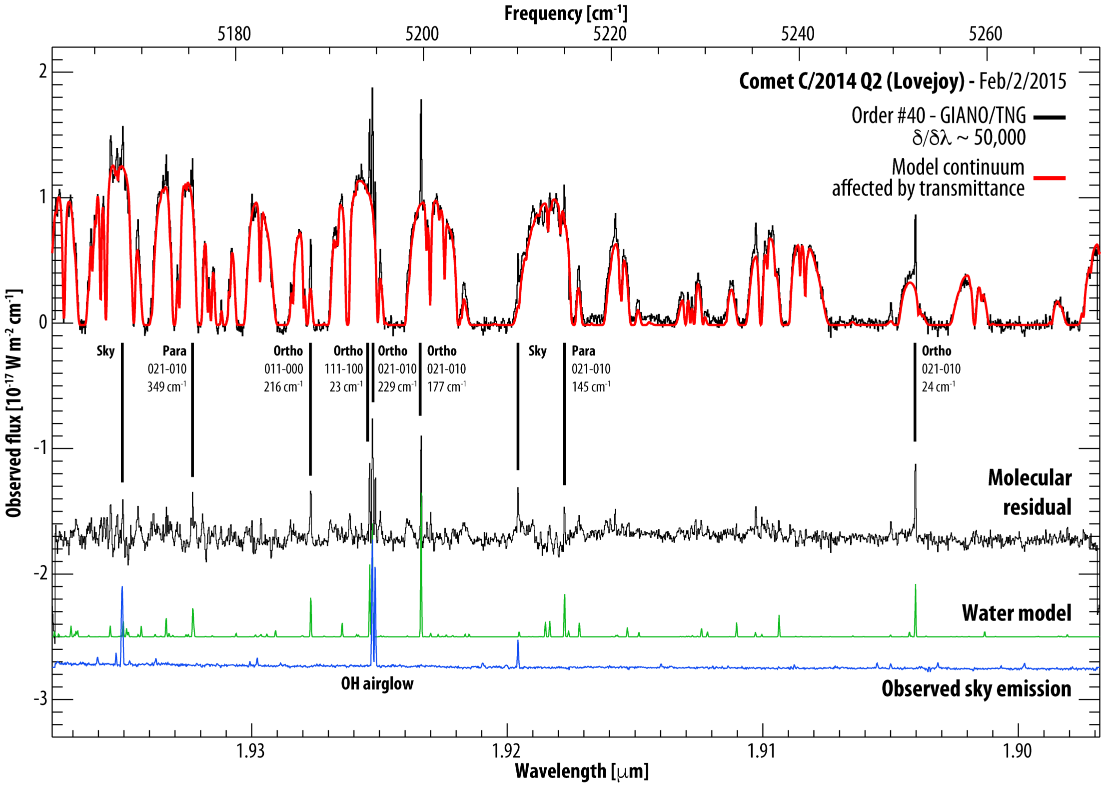

Figure 19a. Here, we illustrate the reduction and identification process by showing cometary spectra from order 40 of a GIANO echellogram. The observed fluxes [10^{-17} Wm^{-2}/cm^{-1}] are shown vs. wavelength (frequency). The scale of the x-axis is shown in frequency [cm^{-1}] at top, and in wavelength [mm] at bottom. The topmost trace compares the calibrated cometary spectrum (black) with the (normalized and superimposed) model of continuum affected by terrestrial transmittance (red), while their difference (the residual spectrum) is shown in the next lower trace. The lowest two traces are a synthetic model of cometary water fluorescence (green, (Villanueva et al., 2012b)) and the observed sky emission (blue). The latter three spectra are shown shifted downward along the y-axis relative to the measured cometary spectrum, for clarity. We identified cometary emission lines by comparing the residual cometary spectrum with the spectra of modeled water fluorescence and measured sky emission (see labels above the cometary residual spectrum). Each label identifies the responsible nuclear spin isomer (ortho, para), quantum numbers for the vibrational band, and the rotational energy in the ground state.

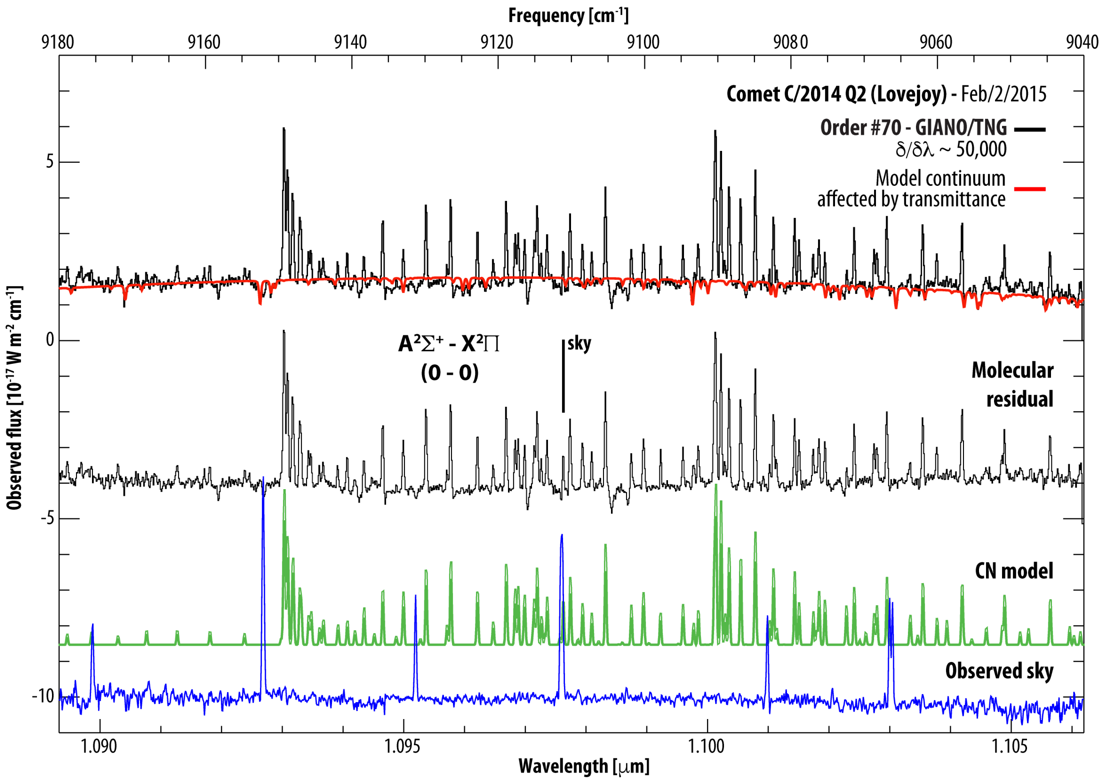

Figure 19b. Cometary spectra from order 70 of a GIANO echellogram is shown. The observed fluxes [10^{-17} Wm^{-2}/cm^{-1}] are shown vs. wavelength (frequency). The scale of the x-axis is shown in frequency [cm^{-1}] at top, and in wavelength [mm] at bottom as in Figure 19a. The topmost trace compares the calibrated cometary spectrum (black) with the (normalized and superimposed) model of continuum affected by terrestrial transmittance (red), while their difference (the residual spectrum) is shown in the next lower trace. The lowest two traces are a synthetic model of cometary CN fluorescence (green, and the observed sky emission (blue). As in Figure 19a the latter three spectra are shown shifted downward along the y-axis relative to the measured cometary spectrum, for clarity. We identified cometary emission lines from the 0-0 band of CN the red-system by comparing the residual cometary spectrum with the spectra of modeled CN fluorescence and measured sky emission (see labels above the cometary residual spectrum).

Similar processes were performed to obtain spectra for *coma-up* and *coma-down* regions. An example of flux-calibrated cometary spectra and the process of continuum subtraction are shown in Figure 19a and Figure 19b, top plot.

The cometary spectrum (black) and modeled continuum (red; as affected by terrestrial atmospheric transmittance) are shown.

An example of cometary molecular residual (after continuum subtraction), of the modeled spectrum for fluorescent water emission, necessary to identify and characterize the detected lines, and of the observed sky spectrum, useful to show the sky emission lines are shown in the bottom part of Figure 19a and Figure 19b for water and CN detection respectively.

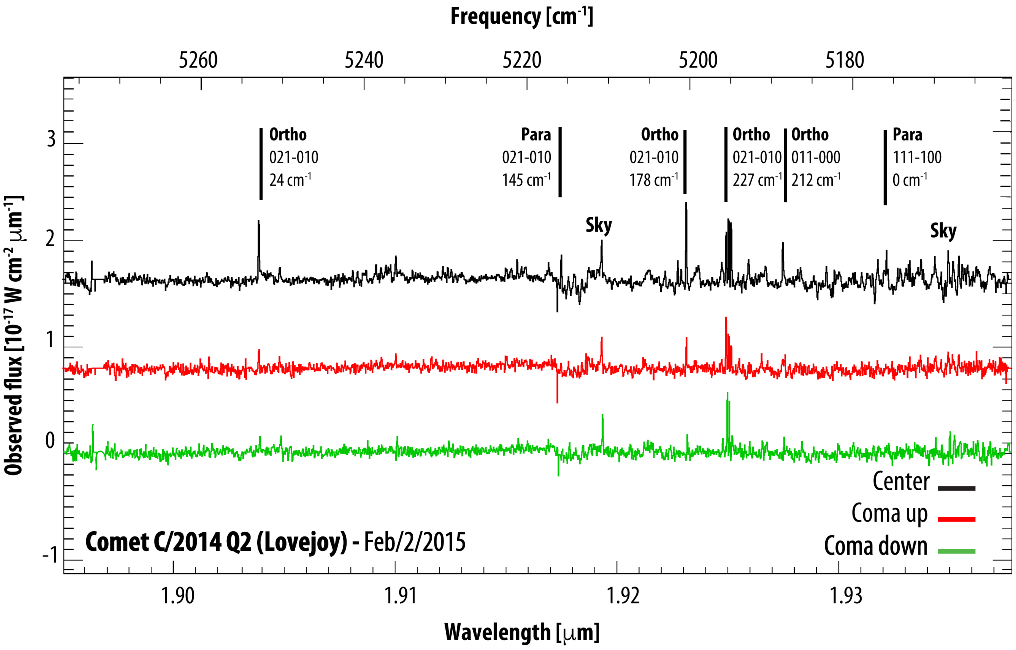

Figure 20. Molecular residual of cometary spectra (after subtraction of continuum affected by terrestrial transmittance) from order 40 of GIANO echellogram are shown. The scale of the x-axis is shown in frequency [cm^{-1}] at top, and in wavelength [μm] at bottom. The three traces are the molecular residuals for the center (black), upper part (red) and lower part of the coma (green). The zero level applies to the coma *center* spectrum, while the *coma-up* and *coma-down* residuals are shown shifted by +1 and -1 unit along the y-axis relative to the *center* residual spectrum, for clarity. Cometary emission lines are identified by comparing residual spectra with spectra of the modeled water fluorescence and of the measured sky emission (see Fig. 3). The cometary lines are strongest in the center spectrum, as expected for a primary volatile released from the nucleus.

In Figure 20, we also show residual spectra of the 3 sampled cometary areas for order 40 of GIANO echellogram : the *center* (i.e., *nucleus-centered)* spectra, the *coma-up* spectra, and the *coma-down* spectra; we proceeded with the water fluorescence analysis using these spectra. A detailed analysis of noise, reported in Appendix C, showed that the measured noise is in agreement with the expected noise.

Chapter 5

Water Fluorescence Analysis

In the medium cometary coma, the rotational population of ground vibrational level of H_2O is maintained at LTE by electron collisions and the main vibrational excitation process is radiative excitation by direct solar radiation. Once excited, water molecules can emit photons at IR wavelengths through a rapid cascade called fluorescent emission, either to the ground vibrational state (so-called *resonance fluorescence*) or to various intermediate energy levels (*non-resonance fluorescence*) with relative efficiencies given by their branching ratios[11]. Fluorescent emission is the main phenomenon observed for primary volatiles in cometary comae at infrared wavelengths (OH prompt emission is an important direct proxy for water emission). [At radio and sub-mm wavelengths, the principal emission mechanism is thermal emission from excited rotational levels in the ground vibrational state.] High-resolution spectrometers such as GIANO can detect these fluorescent emission lines. Using such data and powerful theoretical models, it is possible to characterize the chemical composition of cometary comae with high precision.

We detected 52 water lines in the 2.0 μm and 1.4 μm regions of the GIANO echellogram (Figure 21). These lines represent 8 vibrational water bands. In the 2.0 μm region (orders 39-40-41), we detected two bands in non-resonance fluorescence (111-100) and 021-010) and one band (011-000) in resonance fluorescence, whereas in the 1.4 μm region (orders 53-54-55-56) we detected three non-resonant bands (201-100, 111-010, and 210-010), and two resonant bands (200-000 and 101-000).

---

[11] In the outer coma, collisions cannot maintain the rotational states in LTE. Instead, their populations are set by the balance between solar pumping and subsequent spontaneous decay (known as fluorescence equilibrium).

We used an advanced quantum mechanical fluorescence model for vibrational bands of H_2O to analyze the water emission lines observed in comet Lovejoy. The model evaluates fluorescence efficiencies (g-factors, s^{-1}) using realistic solar spectral fluxes shifted to a comet's heliocentric velocity at the time of observation[12] (Villanueva et al. 2012). Results are given in Table 4.

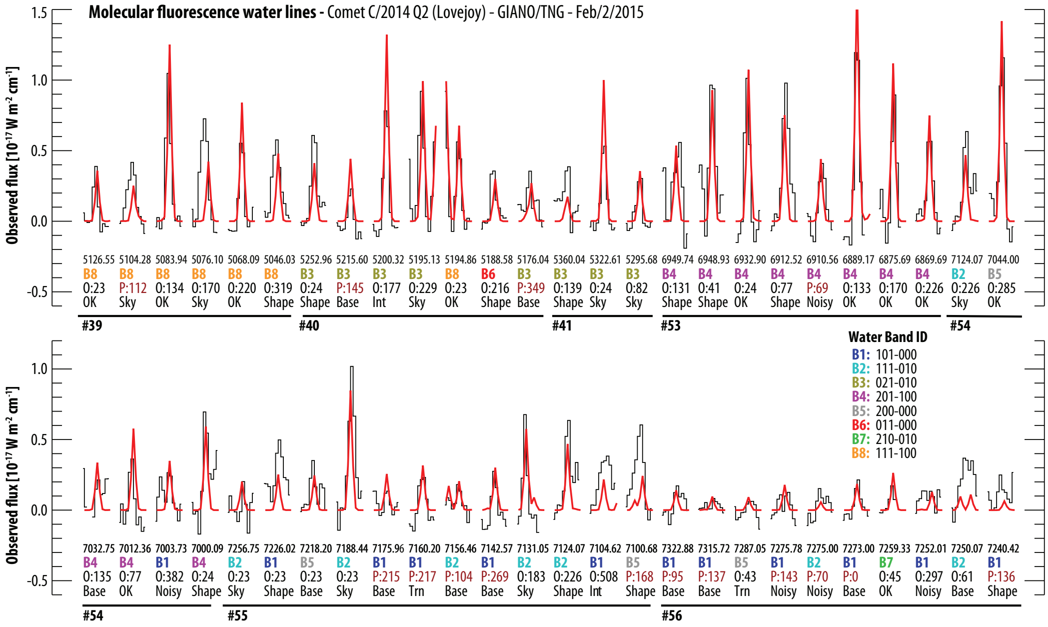

Figure 21. The 52 detected lines of water emission in the 1.4 μm and 2.0 μm regions span seven orders of the GIANO echellogram. The observed positions and intensities of individual lines (black) are compared with predictions of the water fluorescence model (red). On the y-axis the observed line flux [10^{-17} Wm^{-2} cm^{-1}] is shown. On the x-axis the order ranges (horizontal bars, bold) are reported. together with a detailed description of each line. Under each line we show the rest wavenumber [cm^{-1}], the vibrational band ID (B1-B8, see legend at right, lower panel), the nuclear spin isomer (O for ortho, P for para) and the lower energy level [cm^{-1}] (e.g., O:135), and a 'quality' label. The labels are: *OK* for a well fitted line, *Noisy* for a line with a noisy continuum, *Trn* for a line with <10% transmittance, *Base* for a line with baseline problems, *Shape* for a line with misfit in shape, and *Int* for a line with misfit in intensity.

---

[12] Fluorescence efficiencies (g-factors) can depend on the Doppler shift in cometary gas relative to the Sun, especially in spectral regions with crowded Fraunhofer lines (e.g., the CN violet system) or where the solar spectrum contains spectral lines of the same species as sought in the comet (e.g., CO). This effect takes two forms: the "Swings effect" stems from the frequency shift produced by heliocentric velocity of the comet's motion (Swings, 1941), while the "Greenstein effect" stems from the shift in frequency due to the motion of molecules in the cometary coma (Greenstein, 1958). The latter effect is usually considered negligible.

A careful and detailed study of every detected line led us to discard lines affected by the following issues:

- Contamination by residual sky emission:

  Sky lines can be present in our cometary spectra for two systematic reasons, even if the sky emission does not vary with time: First, we took data with the comet centered first in the A-fiber and then in the B-fiber. Taking data in this ABAB mode will generally ensure a mismatch in the sky emission since the air masses of sequential (A, B) frame pairs differ by the same amount and in the same relative sense. Although both fibers are sampled simultaneously, we chose not to subtract the on- and off-nucleus spectra, because the nucleus-centered coma emission would then be reduced by the off-nucleus coma flux. Accordingly, sky frames were acquired after comet observations, with the telescope shifted by 800 arc-sec in Right Ascension from the comet position. This approach prevents exact cancellation of sky emission, instead leaving a positive or negative residual owing to the difference in air mass during integration on sky and on comet[13]. Moreover, the principal sky emissions (OH Meinel bands) vary with time, introducing a second factor that limits sky cancellation of such emission even if taken at the same air mass but at different times. Most recent analysis of OH Meinel bands system, detected with GIANO, is reported by (Oliva et al., 2013; 2015).

---

[13] OH airglow emission lines dominate sky spectra in GIANO's spectral range. We are able to identify them thanks to precise line lists, but a good quantum mechanical model for OH chemiluminescent emission in our atmosphere is not available. Sky emission lines also vary with time and with altitude, so the only way to identify and remove them from a cometary spectrum is by making direct sky observations.

- Baseline problems:

  Baseline issues can be introduced by diverse effects such as imperfect sky subtraction or imperfect modeling of the cometary continuum convolved with the synthesized terrestrial atmospheric transmittance.

- Misfit in shape:

  The presence of embedded emission lines from other molecules (or even from H_2O) could cause the measured shape of a cometary line to differ from that predicted by the fluorescence model.

- Misfit in intensity:

  The non-perfect evaluation of some fluorescence model parameters could contribute to a misfit between predicted and measured intensity.

We included only lines that were labeled as *"OK"*, *"Noisy"*, or *"Trn"* (Figure 21) when evaluating fluxes at top of the atmosphere, column densities, and production rates for ortho-water and para-water (see Figure 22). The *"Noisy"* label means that these lines are embedded in a noisy continuum and the *"Trn"* label means that the transmittance evaluated for that line was <10%. A quantitative description for each of the 52 detected lines is given in Figure 21 and reported in Table 4. The label *"Base"* indicates a line with baseline problems, "*Shape*" a line with misfit in shape, and *"Int"* a line with misfit in intensity.

Table 4. Parameters for Spectral Lines of H_2O detected in C/2014 Q2 (Lovejoy).

ν (cm^{-1})	**Band ID n_{up}-n_{low}**	**Line ID J, k_a, k_c**	**Ortho, Para**	**E_{rot} (cm^{-1})**	**g-factor (10^{-8}s^{-1})**	**Trans. (%)**	**Flux TOA (10^{-18} W m^{-2})**	**Q $_{H2O}$ (10^{29} s^{-1})**
5126.55	111-100	000-101	O	23	1.18	32	1.21 ± 0.31	3.39 ± 0.87
5104.28	111-100	101-202	P	112	0.98	30	2.75 ± 0.38	Sky
5083.94	111-100	202-303	O	134	1.72	75	1.49 ± 0.14	3.00 ± 0.28
5076.10	111-100	211-312	O	170	0.57	77	1.55 ± 0.14	Sky

5068.09	111-100	313-414	O	220	0.90	96	6.19 ± 0.90	2.58 ± 0.38
5046.03	111-100	404-505	O	319	0.50	98	1.11 ± 0.12	Shape
5252.96	021-010	000-101	O	24	2.55	17	5.47 ± 0.34	Shape
5215.60	021-010	212-313	P	145	0.93	49	3.14 ± 0.11	Base
5200.32	021-010	211-312	O	177	2.36	58	1.60 ± 0.99	Int
5195.13	021-010	313-414	O	129	1.85	56	2.95 ± 0.10	Sky
5194.86	111-100	202-101	O	23	1.31	62	1.11 ± 0.91	3.34 ± 0.27
5188.58	011-000	202-321	O	216	1.80	17	2.98 ± 0.32	Shape
5176.04	021-010	312-413	P	349	0.59	55	8.89 ± 0.10	Base
5360.04	021-010	404-303	O	139	0.99	21	3.10 ± 0.22	Shape
5322.61	021-010	202-101	O	24	2.51	41	1.70 ± 0.11	Sky
5295.68	021-010	211-212	O	82	0.75	49	7.67 ± 0.91	Sky
6949.74	201-100	220-221	O	131	0.71	78	2.07 ± 0.36	Shape
6948.93	201-100	111-110	O	41	1.28	75	2.68 ± 0.38	Shape
6932.90	201-100	000-101	O	24	1.37	81	1.75 ± 0.35	3.11 ± 0.62
6912.52	201-100	111-212	O	77	1.20	64	3.61 ± 0.44	Shape
6910.56	201-100	101-202	P	69	0.67	68	8.01 ± 0.42	2.94 ± 0.16
6889.17	201-100	202-303	O	133	2.04	88	2.28 ± 0.31	2.87 ± 0.40
6875.69	201-100	211-312	O	170	1.26	91	1.38 ± 0.30	2.88 ± 0.65
6869.69	201-100	313-414	O	226	0.88	88	1.38 ± 0.31	4.39 ± 0.99
7124.07	111-010	313-414	O	226	1.18	42	3.02 ± 0.35	Sky
7044.00	200-000	221-330	O	285	3.35	44	5.07 ± 0.63	3.80 ± 0.47
7032.75	201-100	404-303	O	135	0.42	84	6.32 ± 0.33	Base
7012.36	201-100	313-212	O	77	0.68	87	4.50 ± 0.31	1.80 ± 1.27

7003.73	101-000	313-432	O	382	0.57	62	1.10 ± 0.44	3.10 ± 1.60
7000.09	201-100	202-101	O	24	1.04	58	1.93 ± 0.47	Shape
7256.75	111-010	202-101	O	23	1.52	14	2.11 ± 0.78	Sky
7226.02	101-000	000101	O	23	37.4	1	1.95 ± 0.25	Shape
7218.20	200-000	110-101	O	23	2.69	9	8.96 ± 0.18	Base
7188.44	111-010	000-101	O	23	1.60	54	3.81 ± 0.31	Sky
7175.96	101-000	303-322	P	215	0.66	41	4.40 ± 0.42	Base
7160.20	101-000	303-404	P	217	12.4	3	1.17 ± 0.65	2.50 ± 1.40
7156.46	111-010	110-211	P	104	0.49	44	8.04 ± 0.38	Base
7142.57	101-000	312-413	P	269	8.11	4	4.58 ± 0.42	Base
7131.05	111-010	211-312	O	183	1.01	47	3.53 ± 0.28	Sky
7124.07	111-010	313-414	O	226	1.18	42	3.02 ± 0.35	Shape
7104.62	101-000	431-532	O	508	0.98	23	5.01 ± 0.63	Int
7100.68	200-000	111-220	P	168	1.17	28	6.90 ± 0.53	Shape
7322.88	101-000	312-211	P	95	4.31	3	5.29 ± 0.39	Base
7315.72	101-000	321-220	P	137	2.27	5	3.87 ± 0.29	Base
7287.05	200-000	221-110	O	43	2.92	3	4.00 ± 0.42	3.33 ± 3.50
7275.78	101-000	312-313	P	143	1.19	15	2.06 ± 0.86	4.67 ± 1.95
7275.00	111-010	303-202	P	70	0.36	16	1.43 ± 0.82	3.95 ± 0.16
7273.00	101-000	101-000	P	0	9.62	2	1.62 ± 0.66	Base
7259.33	210-010	221-110	O	45	0.46	51	3.99 ± 0.21	2.16 ± 1.16
7252.01	101-000	422-423	O	297	1.23	11	3.62 ± 0.95	5.19 ± 1.93
7250.07	200-000 111-010	221-212 212-111	O P	61	0.65	33	4.36 ± 0.40	Base
7240.42	101-000	221-220	P	136	6.53	1	4.31 ± 0.10	Shape

5.1 Rotational temperatures

We observed comet Lovejoy with the two 1" angular diameter fibers (about 700 km diameter at the comet) placed at a fixed center to center distance of 3" (about 2100 km at the comet on Feb 2). This means that we observed three different regions in the medium coma, each sampled by a circular beam of 700 km diameter: one region targeted the photometric center and two regions sampled the coma at ± 2100 km from the photocenter (see Figure 1 for observation set-up).

The rotational temperature (T_{rot}) of a molecule is the temperature that defines the population distribution of rotational levels in the ground vibrational state. In the medium coma (50 km $\leq r \leq 10^4$ km), electron collisions maintain the ground ro-vibrational states at local thermodynamic equilibrium (LTE). The population distribution P_i of rotational levels is described by the following equation, according to the Boltzmann statistic:

$$P_i = \frac{\omega_i e^{-E_i / k_B T_{rot}}}{Z(T_{rot})} \qquad (3)$$

where ω_i is the statistical weight of level i[14], E_i is the energy of the level i, and $Z(T_{rot})$ is the rotational partition function[15]. We used two different methods to evaluate T_{rot}: *the slope analysis* and the *correlation analysis* (Figure 22).

The *slope analysis* method extrapolates T_{rot} for the rotation population in the ground vibrational state considering the relation between F_{obs} / F_{pred}, the observed to predicted flux ratio, and $<E_{pump}^{(000)}>$ the mean value of rotational state energies in the ground vibrational state.

---

[14] Each energy level can be composed of a number of degenerate (equal-energy) quantum states; this number is statistical weight ω_j of level i.

[15] Where: $Z(T_{rot}) = \sum_i \omega_i e^{-E_i / k_B T_{rot}}$

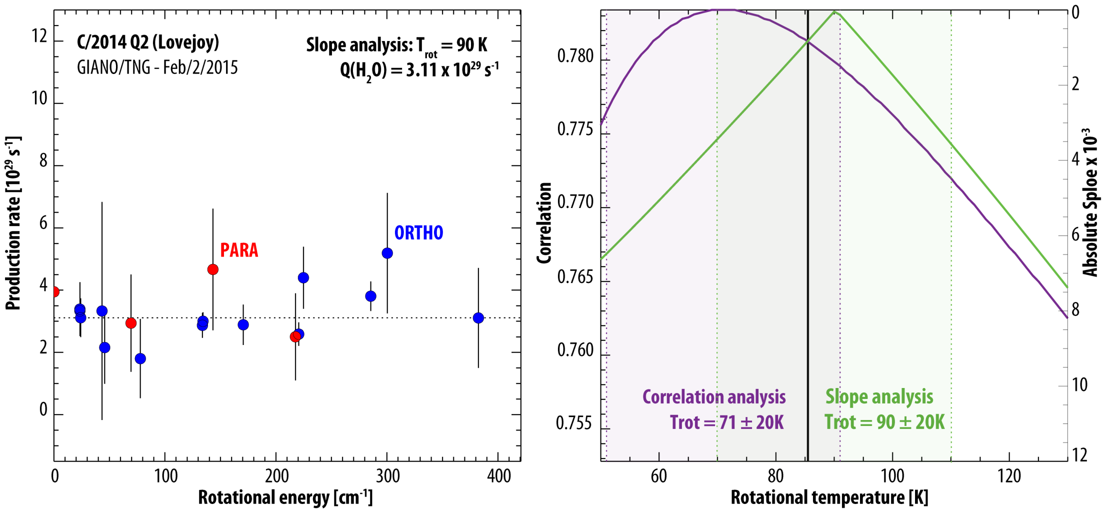

Figure 22. Determination of the rotational temperature of H_2O in comet Lovejoy for the lines that were labeled as *"OK"*, *"Noisy"*, or *"Trn"* .
Left: The slope analysis method. The x-axis represents the mean lower rotational energy [cm^{-1}] of the principal pumping transitions and the y-axis represents the water production rate [$Q(H_2O)$, units of 10^{29} s^{-1}] extracted from an individual line. A specific value of T_{rot} is assumed, and the summed g-factor for each line is recalculated for that value; a linear fit to the data provides a slope. The process is continued at 1 K intervals, over the range 50-150 K. The water production rates [ortho (blue) and para (red)] are evaluated by assuming the abundance ratio of ortho- and para-water was 3, i.e. the measured values of water production rate for the full-water model. The graphic shows the line-by-line values of $Q(H_2O)$ returned for T_{rot} = 90 K, and the linear fit (dotted line; slope = zero).
Right: Comparison of the slope and correlation analyses. The x-axis represents the rotational temperature T_{rot} [K]. The scale for the correlation coefficient appears on the left y-axis and the scale for absolute values of slope appears on the right y-axis. The graphic shows the comparison between T_{rot} derived from the slope method (green) and from the correlation method (purple).

The predicted fluxes (i.e. the modeled g-factors) depend on T_{rot}. The line flux (W m^{-2}) of optically thin ro-vibrational lines is described by the following formula:

$$F_{ul} = \frac{\Omega}{4\pi} h\nu_{ul} g_{ul} \langle N \rangle \tag{4}$$

where Ω is the solid angle corresponding to the field of view, ν_{ul} is the frequency (cm^{-1}), g_{ul} is the g-factor (i.e. the cometary fluorescence emission rate, photon s^{-1}), and <N> is the column density (m^{-2}). The g-factors, are given by:

$$g_{ul} = A_{ul} \frac{\sum_{j,v=0} n_j g_{ju}}{\sum_j \sum_v A_{ul}} \tag{5}$$

where A_{ul} is the (Einstein) spontaneous emission coefficient from upper level 'u' to lower level 'l', n_j is the fractional population of level 'j', and g_{ju} are the excitation rates due to solar pumping ($g_{pump}= g_{ju}$), defined in the following equation:

$$g_{pump} = \frac{J_v B_{lu} \omega_l e^{-hcE_{low}/kT_{rot}}}{Z(T_{rot})} \tag{6}$$

Here, J_v is the realistic solar flux received by the comet at frequency ν, B_{lu} is the Einstein coefficient for absorption, ω_l is the degeneracy of the lower state and E_{low} is the energy of the lower state (Villanueva et al., 2011b).

The line fluxes are related to the populations of rotational levels in the upper vibrational state E_{up} and reflect the temperature dependent distribution of the ground state (000). In general, a single rotational upper state is pumped from several different rotational levels in the ground vibrational state $E_{pump}^{(000)}$. The average energy of these lower rotational levels (weighted by their relative contributions to the upper state population) approximates the 'mean' energy of the ground state from which they populate the upper state when pumped. At the correct rotational temperature, the ratio between the measured flux and g-factor of the line should be independent of $<E_{pump}^{(000)}>$. The retrieved rotational temperature is most accurate when a wide range of rotational energy states is sampled.

The quantity described by Flux [Wm^{-2}] / g-factor [W mol^{-1}] is proportional to the column density (see equation 4). Since the production rate of a molecule is proportional to the column density, a linear fit of Q [s^{-1}] vs $<E_{pump}^{(000)}>$ should produce a diagram with slope zero within the errors on Q[16]. This diagram is shown in Figure 22, left panel.

The evaluation of an accurate rotational temperature is essential to achieve reliable production rates and, in the slope analysis, this is obtained by comparing all the observed line fluxes (corrected to top of Earth's atmosphere) with respect to the modeled line fluxes, varying the assumed value for T_{rot} until an agreement is found within the errors, across all the observed lines. From the slope analysis the retrieved rotational temperature is about $T_{rot} = (90 \pm 20)$ K. The confidence limits for T_{rot} were evaluated by the statistical error of the ($F/g(T_{rot})$ vs E_{up}) slope. The confidence limits for the slope were selected considering the higher uncertainty between the stochastic error and the variance error (standard error). The stochastic error describes the uncertainty produced by photon noise while the variance error describes the spread of the derived quantities around the slope line. We obtained a stochastic error for the slope zero of about ±0.004 that corresponds to an interval of about ±20K in temperature. For the correlation analysis the limits were assumed to be the same as for the slope analysis.

The *correlation analysis* is based on the comparison between the water model and the observed spectrum[17]. The OPR=3 is assumed, so the unique free parameter is the rotational temperature T_{rot}. The purpose of this method is to evaluate the correlation coefficient between the observed and the synthetic spectrum, thus identifying the (most probable) temperature that produces the best correlation.

The temperature-correlogram plot (Correlogram Factor vs. T_{rot}) is shown in Figure 22 (right panel). The sharper the correlation curve is, the better T_{rot} can be constrained by the correlation analysis. From the correlation analysis the retrieved rotational temperature is

---

[16] A value of T_{rot} lower than its optimal value will produce a positive slope. This means that for lines with relatively low rotational energy, the modeled g-factors are overestimated, while for high-values of rotational energy they are underestimated.

[17] The retrieval code synthesizes a modeled water spectrum for each value of T_{rot}, using the modeled g-factors. After convolution with the resolving power of the instrument, this synthetic spectrum is compared with the observed spectrum.

about T_{rot} =(71± 20) K. The comparison of T_{rot} from the slope and the correlation analyses can also be compared visually (right panel, Figure 22).

5.2 Water production rate

We used the slope-zero rotational temperature obtained from the slope analysis (90 K ± 20 K) to evaluate the total production rate of water in comet Lovejoy.

We assume that water molecules sublimate at the nucleus surface at a constant rate and expand into the coma with Spherical Symmetry and with Uniform Velocity (the SSUV model). The production rate obtained from a single measured line (Q_i [s^{-1}]) is evaluated as follows:

$$Q_i = \frac{4\pi\Delta^2 F_i^{TOA}}{g_i\tau(hc\nu)f(x)} \tag{7}$$

where: Δ [m] is the geocentric distance, F_i^{TOA} [W m^{-2}] is the flux of the i-th line, at top of the terrestrial atmosphere (corrected for the terrestrial transmittance at the Doppler-shifted line frequency), g_i [photons s^{-1} mol^{-1}] is the g-factor related to the i-th line at temperature T_{rot}, t [s] is the molecular lifetime, (hcn) is the energy (in Joules [J]) of a photon with wave number n(cm^{-1}), and f(x) represents the fraction of total molecules contained in the beam for the SSUV model, where x is the scaled, projected displacements of the edges of the aperture from the cometary nucleus.

A detailed description of all lines is reported in Table 4. The column labeled as Q(H_2O) lists the total water production rate obtained from each observed line, assuming that the nuclear spin species are in statistical equilibrium (OPR = 3.0).

The total water production rate derived from our measurements (assuming ortho to para ratio equal to 3) is Q(H_2O) = (3.11± 0.14) x 10^{29} s^{-1}. The production rates derived for ortho-water and para-water separately are Q(H_2O)^{ORTHO}=(2.33 ± 0.11) x 10^{29} s^{-1} and

$Q(H_2O)^{PARA} = (0.87 \pm 0.21) \times 10^{29}\ s^{-1}$. These values are the weighted mean of Q's obtained from individual line measurements and the uncertainties were determined by comparing the standard deviation from the mean of production rates with the error due to photon noise, and taking the higher value.

The $Q[s^{-1}]$ values, derived from each individual observed line and those taken from different ro-vibrational lines of different bands, showed a general agreement (similar to those in Figure 22). This reinforces the self-consistency of the data processing algorithms and the fluorescence models used in this investigation.

5.3 Ortho-Para ratio (OPR)

As introduced in Chapter 3, in general a molecule that contains identical atoms in spatially symmetric locations shows isomeric symmetries associated with the total nuclear spin angular momentum. With identical hydrogen atoms (H) in spatially symmetric locations, the H_2O molecule shows the intrinsic property to exist in two distinct species (ortho and para), depending on the orientation of nuclear spins of its H atoms.

Each hydrogen atom in water has a magnetic moment, which is associated with the proton's spin of value 1/2. When the spins are parallel, there is a paramagnetic state called *ortho*-H_2O with a total nuclear spin I=1. This is the triplet state $[(\uparrow\uparrow), 1/\sqrt{2}(\uparrow\downarrow + \downarrow\uparrow), (\downarrow\downarrow)]$, i.e. with three symmetric spin states characterized by nuclear spin projected values $M_I = (+1, 0, -1)$. When the spins are anti-parallel there is the nonmagnetic state called *para*-H_2O with total nuclear spin $I = 0$ and the component along a defined axis $M_I = 0$. This state is described by one anti-symmetric spin state $1/\sqrt{2}(\uparrow\downarrow - \downarrow\uparrow)$.

Even though both spin isomers species are water, the ortho and para forms of water are two distinct molecules with distinct energy levels. The difference between the lowest para energy level and the lowest ortho energy level is about 23.8 cm^{-1} (~34 K), meaning that the ratio between the total populations of ortho and para states (the OPR) depends on the temperature (T_{spin}) at which the molecules were formed. For example at temperature T= 0 K the equilibrium ratio of water isomers is all para, because the lowest para energy level (000) is 23.8 cm^{-1} below the lowest ortho level. For temperature T > 50 K the statistical equilibrium value is achieved and the ratio of ortho and para water is 3:1.

The probability of permutation between ortho to para water is almost zero, indeed it is possible to have a conversion between them only via molecule breaking and later reformation[18], or by interaction with a strong non-uniform magnetic field such as is experienced during a collison with another paramagnetic species. Exchange transitions between the two water spin states, whether radiative or collisional, are forbidden by quantum mechanical selection rules. This leads to the idea that the relative abundance of the nuclear spin species remains largely unchanged for billions of years (Mumma and Charnley, 2011; Mumma et al., 1987). If so, the spin temperature would reflect the formation temperature of the molecule.

The idea to retrieve an OPR for water in the cometary coma is linked with the measure of the chemical formation temperature of water in the early phase of the solar system formation. The OPR in cometary water was measured for the first time in 1P/Halley (Mumma et al., 1987; 1988), and the low values of T_{spin}, found in the pre-perihelion evaluation (~35 K) and post-perihelion evaluation (> 40 K), suggested that the conditions of the formative stage of our planetary system were preserved.

There is a strong debate on reliability of the OPR property as signature information about the original temperature of the molecule's formation. It is almost evident that H_2O molecules preserve the nuclear spin during their long residence in the interior of a comet

---

[18] Another possibility has been studied by Limbach et al. 2006, in which the spin conversion can happen on ice surfaces. This leads to thinking that the measured OPR in cometary coma, for gas released from a cold icy nucleus, could reflect the nucleus surface temperature.

and probably during the sublimation process, but our knowledge about the nuclear spin conversion is still meager. Although this debate is strong, the evaluation of T_{spin} is an important diagnostic in order to study the origin of cometary material. From our measurements we achieve an OPR = (2.70 ± 0.76), but the confidence limits are not small enough to enable a critical test of the nuclear spin temperature.

5.4 Fiber's Growth Factor: variability between nucleus and coma spectra.

To derive the global production rate a detailed study of nucleus outgassing is necessary, i.e. how does the gas dynamically propagate in the coma. Species that are released directly from the nucleus are called *primary molecules.* They can produce *product species* by photo-dissociation and/or photo-ionization processes. Gas generated by these two mechanisms show different radial distribution in the coma and an analysis of spatial distribution is essential to discriminate between them. For spherically symmetric release, a primary molecule shows a column density that varies according to the Haser model as $(e^{-\rho/L})/\rho$, where ρ is the nucleocentric distance projected along the line of sight and L is the molecular (destruction) scale length. In the approximation of $\rho \ll L$, the column density has a behavior of $1/\rho$. For a product species the variation of column density with respect to ρ is much flatter, and may even increase with ρ when dissociation of the parent species begins. Examples of anisotropies and asymmetries in the gas distributions due to non-isotropic outgassing have been observed with radio or long-slit IR and UV spectroscopy. Indeed, the picture presented here is simplistic, but space dictates omission of additional details.

With long-slit spectroscopy it is possible to estimate the global production rate, through a detailed analysis of the spatial profiles for observed molecules in the coma, compensating for 'slit losses' (caused by atmospheric seeing) by employing the so called "Q-curve" methodology (Dello Russo et al., 1998; Villanueva et al., 2011a).

The 'seeing' is the effect produced by the turbulence of Earth's atmosphere that introduces blurring and twinkling on astronomical objects. This effect produces a spread of flux from a point source causing the loss of flux in the central part of the object. The flux from a star (or comet) is then less sharply peaked and thus somewhat less intense in the nucleus region than it would be were seeing absent. A circular aperture that is smaller than the point-spread-function (PSF) will thus measure a reduced flux from the object. This effect is called 'slit or aperture loss'.

The usual "Q-curve" analysis, developed for long-slit spectroscopy, corrects for 'slit losses' by multiplying the measured nucleus-centered Q (obtained with equation (3.5)) by a *Growth Factor* (Q_{scale}) derived by spatial profile analysis. The method is based on the evaluation of apparent production rates at regular intervals along the slit, assuming uniform symmetric outflow (Q_0, Q_1, Q_2,… Q_n). Each value is called a "Spherical Production Rate" because spherically symmetric outflow is assumed when relating the local flux measurement to an apparent production rate (the up- and down-slit profiles are first averaged to remove asymmetries[19].

The *"Nucleus-centered Production Rate"* (Q_{NC}) is the production rate measured in the region close to the nucleus, $Q_{NC}= Q_0$,. The *Terminal Production Rate* is defined as the value of Q evaluated far from the nucleus, along the slit, $Q_{Term} = < <Q_2>, <Q_3>,\ldots,<Q_n> >$. The increase of the mean values of Q from the nucleus-centered position to the terminal position defines the 'Growth Factor' that is quantified by the ratio of the *Terminal Production Rate* and the *Nucleus-centered Production Rate* as shown in the following formula:

$$Q_{scale} = \frac{Q_{Term}}{Q_{NC}} = \frac{\langle Q_2, Q_3, \ldots, Q_n \rangle}{\langle Q_0, Q_1 \rangle} \qquad (8)$$

---

[19] The mean value of $< Q_j >$ taken at symmetric positions with respect the center position Q_0 (i.e. Q_{-i} and Q_i) allows to correct for non symmetric outflow.

The usual retrieval method for long-slit spectroscopy to evaluate the final production rate is not applicable for fiber-fed spectroscopy. Indeed it is not possible to perform the standard analysis of *spherical production rate* in the region close to the nucleus and then the evaluation of *terminal production rate,* recovering the *Growth Factor* (Q_{scale}) in order to estimate the total production rate corrected for seeing.

In our observation method, the nodding on comet with two fibers allows us to sample three different regions of the comet (the *coma up,* the *nucleus,* and the *coma down*), as shown in Figures 1 and 3. After symmetrizing, we have only two points representing the values of column densities in the nucleus-centered region, and in the coma centered 3" away from the nucleus, instead of a complete spatial profile. However, experience with long-slit spectrographs shows that the terminal value is invariably reached by 3" from the nucleus. We obtained the following estimation of column densities: $\sigma^{CENTER} = (6.29 \pm 0.27) \times 10^{20}$ [mol m^{-2}] and $\sigma^{2100} = (1.36 \pm 0.10) \times 10^{20}$ [mol m^{-2}] at 55 K (σ^{2100} is the mean of σ^{DOWN} and σ^{UP}, where $\sigma^{DOWN} = (0.94 \pm 0.13) \times 10^{20}$ [mol m^{-2}] and $\sigma^{UP} = (1.78 \pm 0.16) \times 10^{20}$ [mol m^{-2}] at T_{rot}= 50 K and 60 K respectively, obtained with slope analysis). Application of the SSUV model to these column densities using appropriate parameters then permits determination of a Growth Factor for the fiber-fed case. The expected SSUV f(x) for a 1" aperture at the center is $f^{CENTER} = 0.00533$, and $f^{2100} = 0.00073$ at 3" from the nucleus. Consequently, $Q_{scale} = (\sigma^{2100} / f^{2100}) / (\sigma^{CENTER} / f^{CENTER}) = 1.6$.

We also considered a method for obtaining Q_{scale} from the mean nucleus-centered column density (and Q_{NC}) if we assume a value for the PSF introduced by 'seeing'. Then, the amount of the flux lost by the 'seeing' effect is obtained from the following formula:

$$Q_{Scale}^{FIBER} = \frac{\sum_{FiberFoV} ModeledFluxTOA}{\sum_{FiberFoV} ObservedFlux} \qquad (9)$$

This represents the ratio between the value of the cometary modeled flux at top of the atmosphere integrated in the fiber field of view (Figure 23, panel A), and the observed flux ('seeing' affected), integrated over the fiber field of view (Figure 23, panel B).

We report the comparison between the *Growth Factor* (Q_{scale}) for the GIANO fiber-fed spectrograph and a long-slit spectrograph[20] in Figure 6. Considering a typical seeing of 0.8" for the site, we estimate a value of Q_{scale} for the GIANO fibers of $Q_{scale}^{Fiber} = 1.6$; consistent with the loss observed between the center and up/down fibers.

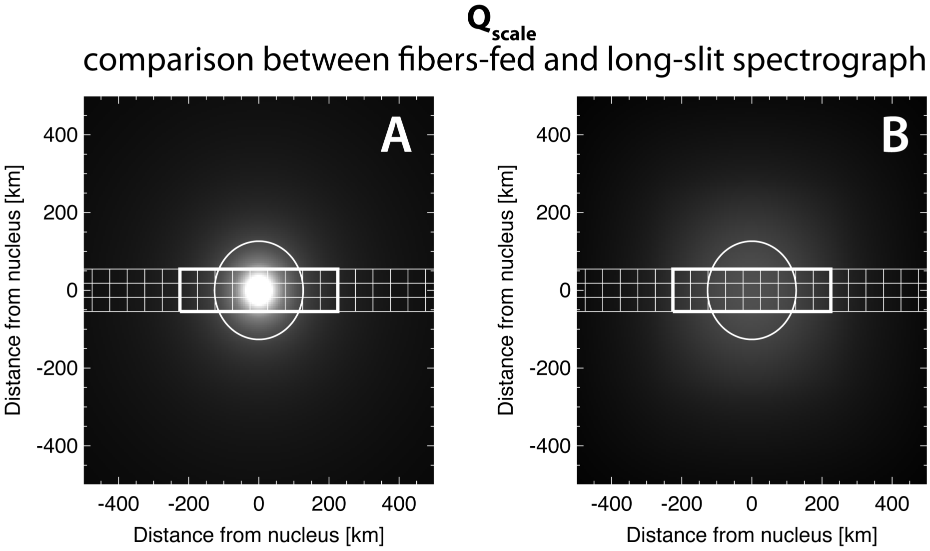

Figure 23. Determination of *Growth Factor* (Q_{scale}) and comparison of long-slit and fiber-fed spectroscopy methods. In both panels, the x- and y-axes represent the distance from the photometric nucleus [km]. Left: Cometary 2-D model of expected outgassing with isotropic outflow, for a comet like C/2014 Q2 Lovejoy. The integration areas for long slit and fiber-fed spectrographs are represented by the square and the circle. Right: The effect of seeing on modeled outgassing data. The ratio between the modeled flux sampled by the fiber FoV in panel (A) with respect to the observed flux (seeing affected) sampled by the fiber FoV in panel (B) defines the Fiber Growth Factor. The same ratio integrated in the long-slit FoV gives the comparison value for long-slit spectroscopy.

---

[20] The comparison has been done for NIRSPEC, the long-slit IR spectrograph at the W. M. Keck Observatory, Mauna Kea, Hawai`i.

Chapter 6

Quantum mechanical model of CN and isotopes

To create a quantum mechanical fluorescence model it is necessary to follow the next steps:

- Create the energy level structure.
- Define an initial rotational population for the ground state.
- Compute the pumping rates and the emission efficiencies.

In the next subsections we will explain each step.

6.1 Description of molecular structure, quantum numbers and energy levels

According to the quantum mechanical valence theory, a free radical is defined as an atom, molecule or ion, with one or more unpaired valence electrons (Herzberg, 1950), so with non zero spin (S)[21]. Radicals can form in the cometary coma during the splitting off a parent molecule in product species by photo-dissociation as described in chapter 1.3.

The radical Cyanide (CN) is a diatomic molecule belonging to the $C\infty v$ point group symmetry, so it has one $C\infty$ rotational symmetry axis (that is the inter-nuclear axis of the molecule) and infinite σ_v vertical reflexion planes of symmetry, all of which contain the $C\infty$ axis (it has no σ_h planes of symmetry). CN is a linear diatomic molecule; it vibrates only along the inter-nuclear axis so has only one vibrational mode identified by the quantum number **v** that can take the values of 0, 1, 2, 3,… (it has $n = 2$ atoms, so 6 degrees of freedom consisting in 3 translational modes, 2 rotational modes and $(3*n - 5) = 1$ vibrational mode). The rotational structure is described by three quantum numbers that

---

[21] This definition is not comprehensive. Following it, chemically stable molecules with unpaired electrons (O_2, NO, NO_2, etc.) are considered free radicals while other molecules with short life-time and high reactivity are not considered free radicals in their singlet state (C_2, C_3, CH_2, etc.). Another definition was adopted by physical chemists; it considers a free radical to be any “transient species”- that is any species with short lifetime in the gas-phase. This definition includes molecules such as C_2, C_3, CH_2, etc. in their singlet state, but it excludes stable molecules such as O_2 and NO.

identify each energy level: the rotational quantum number **N,** the total angular momentum **J**, and the parity **p**. In Figure 24a and 24b the vibrational mode and the angular momentum vectors with relative quantum numbers are shown. An example of the first rotational energy levels for the Red System $A^2\Pi$ - $X^2\Sigma^+$ is shown in Figure 24c.

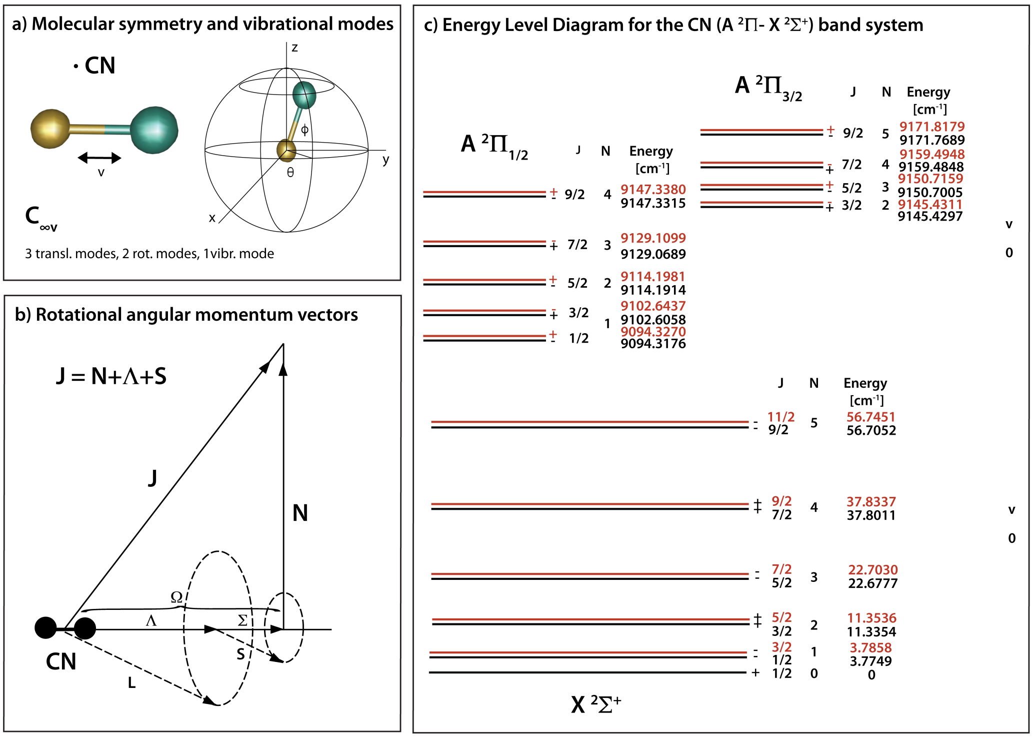

Figure 24. Molecular Structure, ro-vibrational properties, and energy levels for CN. Panel (a): CN molecular symmetry and relative motion of atoms associated with the vibrational mode are illustrated. On the right side of the panel a schematic visualization of molecular motion in a cartesian reference system is shown. Panel (b): Angular momenta vectors are reported. Rotational angular momentum (related to N quantum number) and total angular momentum (J, related to angular (L) momentum and spin (S) projections along the molecule symmetry axis). Panel (c): Ro-vibronic energy levels in v=0 of the ground ($X^2\Sigma^+$) and electronically excited ($A^2\Pi$) states of CN.

The ground state $X^2\Sigma^+$ of CN has electronic orbital angular momentum L = 0 and total spin S = ½ , so the total electronic angular momentum along the inter-nuclear axis Ω (defined as $\Lambda + \Sigma$) takes the value of ½, with degeneracy (2S+1) given by the allowed spin projections along the internuclear access (for $\Sigma = S$, S-1, S-2, …-S). Introducing the coupling between the rotational and the electronic motion we obtain the total angular momentum for the molecule identified by quantum number J = Ω + N = N ± ½ . The rotational quantum number N can take the integral values 0, 1, 2, 3, …, so J can take the values 1/2, 3/2, 5/2, 7/2,… . The electronic excited state $A^2\Pi$ has orbital angular momentum L = 1, so Ω can take the values 3/2 or 1/2 that identify the $A^2\Pi_{1/2}$ and $A^2\Pi_{3/2}$ states (also called F1 and F2); Ω equals 1/2 or 3/2, respectively. Each energy level is identified by N, J and the parity p that can take values + or -. The parity quantum number (**p**) defines the property of the electronic wave function to change sign (or not) with respect to reflexions about one of the infinite σ_v planes of symmetry.

The values of energy levels, Einstein coefficient (A) and oscillator strengths for both the Red System $A^2\Pi$ - $X^2\Sigma^+$ and the Violet System $B^2\Sigma^+$- $X^2\Sigma^+$ were taken from the recently published line list for the main isotopologue $^{12}C^{14}N$ (J. S. A. Brooke et al., 2014).

In Table 5 an extract of the line parameters is reported as an explanatory example.

Table 5. CN Red and Violet Systems line list

$A^2\Pi$ - $X^2\Sigma^+$ (0 - 0)										
J'	J"	F'	F"	p'	p"	N'	N"	ν_{obs} [cm^{-1}]	ν_{cal} [cm^{-1}]	Res [cm^{-1}]
1.5	2.5	1	1	e	e		2	9082.9833	9082.9702	0.01313
2.5	3.5	1	1	e	e		3	9079.9152	9079.8980	0.01723
3.5	4.5	1	1	e	e		4	9076.3599	9076.3587	0.00119
4.5	5.5	1	1	e	e		5	9072.3558	9072.3561	0.00032
5.5	6.5	1	1	e	e		6	9067.8942	9067.8947	0.00046
J'	J"	F'	F"	p'	p"	N'	N"	E" [cm^{-1}]	A [s^{-1}]	f
1.5	2.5	1	1	e	e		2	11.353	7.69E+3	9.31E-5

2.5	3.5	1	1	e	e		3	22.703	1.15E+4	1.57E-4
3.5	4.5	1	1	e	e		4	37.833	1.41E+4	2.05E-4
4.5	5.5	1	1	e	e		5	56.745	1.60E+4	2.4E-4
5.5	6.5	1	1	e	e		6	79.436	1.75E+4	2.74E-4

The ro-vibrational line intensities S_{vJ} of an electronic transition for a diatomic molecule a proportional to the square of the transition dipole moment (TDM) matrix elements.

$$S_{vJ} \propto \left| \left\langle \Psi_{v'J'}(r) \,|\, R_e(r) \,|\, \Psi_{v''J''}(r) \right\rangle \right|^2 \qquad (10)$$

where $R_e(r)$ is the electronic transition dipole moment defined as:

$$R_e(r) = \left\langle \Psi_{el}^{'}(r) \,|\, \mu(r) \,|\, \Psi_{el}^{''} \right\rangle \qquad (11)$$

where $\mu(r)$ is the electric dipole moment operator. In the work of (J. S. A. Brooke et al., 2014) the transition dipole moment (TDM) functions were calculated for both the red and the violet electronic systems. Vibrational transition dipole matrix elements were computed using the LEVEL code developed by (Le Roy and Henderson, 2007). The code takes as input the TDM functions and the Rydberg-Klein-Rees internuclear potential functions providing the matrix elements for a suitable range of v and J. The range of v and J was selected in order to cover the previous experimental line positions, $\boldsymbol{v_{obs}}$, observed by (Ram et al., 2010) with different spectroscopic techniques: v = 0 – 22 and for the $A^2\Pi$ state, v = 0 – 15 for the $B^2\Sigma^+$ state and v = 0 – 15 for the $X^2\Sigma^+$.

Using the experimental line positions, the TDM functions, and spectroscopic constants as inputs, the program PGOPHER (Western, 2010) was used to compute the line positions, ***E”*** [cm^{-1}] and $\boldsymbol{v_{cal}}$ [cm^{-1}], the Einstein coefficients, ***A*** [s^{-1}], and the f-values, ***f***, (J. S. A. Brooke et al., 2014):

- Ro-vibrational energy levels are usually described by the following formula:

$$\mathrm{E}_{\mathrm{v,J}} = \omega_e\left(v+\frac{1}{2}\right) - \chi_e\omega_e\left(v+\frac{1}{2}\right)^2 + B_eJ(J+1) - D_eJ^2(J^2+1) - \alpha_e\left(v+\frac{1}{2}\right)J(J+1)$$

  where ω_e is the harmonic vibrational frequency, $\chi_e\omega_e$ is the vibrational anharmonicity, B_e is the rotational constant, D_e is the centrifugal distortion constant and α_e is the vibration-rotation interaction constant (Herzberg and Huber, 1950).

- Einstein coefficients of spontaneous emission and f-value are obtained from the line strengths using the following relations:

$$\mathrm{A}_{\mathrm{J'J''}} = 3.13618932\times10^{-7}\nu^3\frac{S_{J'J''}}{(2J'+1)} \qquad f = 1.29919368\frac{1}{\nu^2}\frac{(2J'+1)}{(2J''+1)}A_{J'J''} .$$

The retrieval was performed for all observed vibrational bands of the $A^2\Pi$ - $X^2\Sigma^+$ and the $B^2\Sigma^+$ - $X^2\Sigma^+$ electronic transition systems, and also for the purely ro-vibrational bands observed for the $X^2\Sigma^+$ - $X^2\Sigma^+$ system. The rotational dependence of the vibrational transition dipole matrix (Herman-Wallis effect) and the transformation of the matrix elements from the Hund case (a) to the Hund case (b)[22] were taken into account in the LEVEL code. We adopted the line lists for three isotopologues $^{12}C^{14}N$, $^{13}C^{14}N$ and $^{12}C^{15}N$ given by (J. S. A. Brooke et al., 2014)).

The ro-vibrational structure of the energy levels of CN and its isotopes were recreated as a multi-dimensional array (E), indexed by quantum numbers. This multi-dimensional array stores the values of energy for the lower and the upper states of each transition *i* and it was built by extracting the necessary information from the line lists as follows:

---

[22] The resultant of the angular momenta in a molecule is designed as J = S+Λ+N. If the spin S and the electronic orbital angular momentum Λ are equal to zero, then J = N and the molecule is a simple rigid rotator with one quantum number J. This happen for $^1\Sigma$ states. In all the other cases with S ≠ 0 and Λ ≠ 0 the angular momenta can couple in different ways that were studied by Hund. In the Hund case (a) the coupling between the electronic motion (identified with S and Λ) and the rotational motion of the nuclei is assumed to be weak. The electronic motion is strongly coupled with the internuclear-axis of the molecule connecting the two nuclei. (Figure 8.1b). The Hund case (b) consists in the case in which the spin vector S ≠ 0 and is not strongly coupled with the inter-nuclear axis. This can happen both when Λ = 0 and when Λ ≠ 0 but it is weakly coupled with S.

$$E(eS_i'', v_i'', N_i'', F_i'', p_i'') = Ei''$$

$$E(eS_i', v_i', N_i', F_i', p_i') = E_i'' + \nu_i$$

6.2 The initial population of rotational levels and the Partition function

Once we obtain the structure of energy levels of the CN molecule, the next step in order to develop a fluorescence quantum mechanical model is to define the initial population for the vibrational ground state. We assume an initial equilibrium population distribution defined by the Maxwell-Boltzmann statistical distribution. Assuming the thermal equilibrium at a certain temperature T, the population distribution of rotational levels is described by the following formula:

$$P_i = \frac{\omega_i e^{-E_i / K_B T}}{Z(T)} \qquad (12)$$

where ω_i is the statistical weight of level i, that is characterized by the total nuclear spin I_{nucl} and the total angular momentum (J) quantum numbers as $\omega_i = (2I_{nucl}+1)*(2J+1)$. The statistical weight of level i is $\omega_i = 3(2J_i+1)$ for the CN molecule, $\omega_i = 4(2J+1)$ for the isotope $^{13}C^{14}N$ and $\omega_i = 2(2J+1)$ for $^{12}C^{15}N$. E_i is the energy of the level i [cm^{-1}], k_B is the Boltzmann constant [cm^{-1} s] and Z(T) is the molecular partition function. The molecular partition function is defined as $Z(T) = Z(T_{el})Z(T_{vib})Z(T_{rot})$; its computation is difficult and requires a comprehensive knowledge of all the electronic, vibrational and rotational modes. Since cometary atmospheres are cold (T< 300 K) only the lowest ro-vibrational energy levels are populated, so the total partition function can be written as in the following formula, extracting the information from the line list:

$$Z(T) = \sum_i \omega_i'' e^{-E_i'' / K_B T} \qquad (13)$$

where ω''_i is the statistical weight of the lower state energy level of the line i with energy E''_i

6.3 Computation of fluoresce pumping and g-factors

After creating the energy levels structure and populating it, knowledge of the selection rules is essential to computing the pumping rates and emission efficiencies (g-factors) for the system. The quantum numbers and the symmetry properties of the CN molecule, introduced in chapter 6.1, determine the spectrum of the diatomic molecule itself. The selection rules are obtained from the evaluation of ***R,*** the matrix elements of the electric dipole moment:

$$R = \int \psi'^{*} \mu \psi'' d\tau = \iiint \psi'^{*}_{ele} \psi'^{*}_{vib} \psi'^{*}_{rot} \mu \psi''_{rot} \psi''_{vib} \psi''_{ele} \, d\tau_{ele} d\tau_{vib} d\tau_{rot} \neq 0 \qquad (14)$$

where ψ' and ψ'' are the wave functions of the upper and the lower energy levels and where μ is the electric dipole moment. When the value of the transition moment of R is different from zero the transition between the two levels is allowed, otherwise it is forbidden. The result of the integral depends on quantum numbers that describe the wave functions, and their relation for non-vanishing ***R*** defines the selection rules. In the Born-Oppenheimer approximation the overall wave function is written as the product of electronic, vibrational, and rotational wave functions $\psi=\psi_{ele}\psi_{vib}\psi_{rot}$, so there are separate selection rules for the rotational, vibrational and electronic levels.

The rotational selection rules are:

- for the total angular momentum J: $\Delta J = J' - J'' = 0, \pm 1$; J = 0 not ↔ J = 0
- for the parity p: + ↔ - ; + not ↔ +; - not ↔ -

when the nuclear spin of the two nuclei is non zero, as in the case of CN in which $I_{12C} = ½$ and $I_{14N} = 1$, the total angular momentum is $F = J + I_1 + I_2$ and the correct selection rules are the analogue of those for J : $\Delta F = F' - F'' = 0, \pm 1$; F = 0 not ↔ F = 0.

The electronic selection rules are:

- for the electronic orbital angular momentum Λ: $\Delta\Lambda = \Lambda' - \Lambda'' = 0, \pm 1$
- for the spin S: $\Delta S = S' - S'' = 0$

The selection rule for the spin implies that transitions between electronic states with different multiplicity, or equally different spin value, are forbidden. For the S state defined by S=0, additional rules for the symmetry properties apply: $\Sigma^+ \leftrightarrow \Sigma^+$; $\Sigma^- \leftrightarrow \Sigma^-$; $\Sigma^+ \leftrightarrow \Sigma^-$.

The vibrational selection rule:

- for the vibrational quantum number v: $\Delta v = v' - v'' = \pm 1$

This rule is valid if the transition occurs in the same electronic level. If the transition involves an electronic transition the vibrational selection rule does not apply.

The most valuable characteristic of a spectral line list is that the selection rules are contained in the list itself. The selection rules are identified by the existence, or not, of a spectral line, so of a transition. Simply reading the line list iteratively, we can compute the pumping rate and the emission efficiencies by extracting from the list the information needed. For each line of the atlas the solar pumping rate was evaluated with the following formula:

$$g_{pump}(l') = \frac{\sum_{l''} J_s(v_s) B_{12} \omega'' e^{-E''/K_B T}}{Z(T)} \tag{15}$$

where *l* indicates a set of quantum numbers for the lower states *l”* = (eS_i”, v_i”, N_i”, F_i”, p_i”) or upper states *l’* = (eS_i’, v_i’, N_i’, F_i’, p_i’). B_{12} is the Einstein coefficient for induced absorption[23] [$J^{-1}s^3cm^{-3}$], and is related to the Einstein coefficient for stimulated emission B_{21} [$J^{-1}s^3cm^{-3}$] and spontaneous emission A_{21} [$J^{-1}s^3cm^{-3}$] through the following formula:

$$B_{12} = B_{21}\frac{\omega'}{\omega''} \quad \text{and} \quad B_{21} = \frac{A_{21}}{(8\pi h v^3)} \tag{16}$$

where ω’ is the degeneracy of the upper state and ω” of the lower state, ν is the frequency [cm^{-1}] and *h* is the Planck constant ($6.62607004 \times 10^{-34}$ [J s]). $J_s(\nu_s)$ is the solar flux at the

---

[23] for B_{12}, B_{21} and A_{21}, the subscripted index “12” is referred to the lower level, *1*, and upper level, *2*. We change notation of upper and lower energy levels in the Einstein coefficients because using the apexes ‘ and “ was confusing to distinguish the difference between upper and lower order.

Doppler-shifted frequency of the line $\nu_s = (1 - u/c)\nu$, where u is the velocity of the comet with respect to the Sun [cm s^{-1}] and c is the speed of light [cm s^{-1}]. To compute $J_s(\nu_s)$ we adopted a high resolution flux-calibrated solar spectrum generated by the combining the empirical line-by-line solar transmittance spectrum (Hase et al., 2006) with the theoretical solar model for continuum irradiance (http://kurucz.harvard.edu/). In the past decades a multitude of observations of solar spectrum were obtained, mainly from space spectrographs on satellites but also from ground based observatories. Only satellite-borne spectrometers allowed the collection of a complete solar spectrum in the infrared spectral regions, free of the contamination produced by telluric atmospheric absorptions. The ATMOS-FTS instrument (Atmospheric Trace Molecule Spectroscopy Fourier transform spectrometer) on NASA's Space Shuttle (Abrams et al., 1996) and the ACE-FTS (Atmospheric Chemistry Experiment Fourier transform spectrograph) on SCISAT-1 (Hase et al., 2006) are examples of space-borne spectrometers that collected huge amounts of data. These space-based observations together with the ground-based spectral survey performed at Kitt-Peak Observatory (Wallace and Livingston, 2003), provided a comprehensive amount of spectral data, from 600 to 15000 cm^{-1}. (Hase et al., 2010) created an empirical line-by-line list for the solar spectrum, merging the information from all the collected observations. Thanks to the high sensitivity and the increased signal-to-noise ratio of the ACE-FTS data[24], the atlas identified many weak absorption features - greatly increasing our knowledge of the solar spectrum. The solar spectra collected in this database are provided as transmittance spectra and are not flux calibrated. Fortunately theoretical models of solar spectra show excellent success in evaluating the solar continuum irradiance, but they do not adequately reproduce all absorption features present in the real solar spectrum. So the

---

[24] As described in (Hase et al.2010) the resolving power of the ACE-FTS is less than ATMOS resolving power about a factor of 2. However, ACE-FTS produces solar spectra with much higher signal-to-noise ratio due to the large number of available ACE spectra.

combination of real observed solar transmittance spectra with the theoretical solar irradiance can provide a real high-resolution flux-calibrated solar spectrum. Among the several models, the Kurucz theoretical solar irradiance model is considered the best (Kurucz, 2009). Following (Villanueva et al., 2011b), we multiplied the observed transmittance spectrum provided by (Hase et al., 2010) with the accurate continuum irradiance model of Kurucz, thereby obtaining a flux-calibrated solar spectrum in the GIANO wavelength regions. The fluorescence emission rates (g-factors) for each line *i* are computed from the pumping rates and the evaluation of the branching ratio:

Table 6. Computed g-pump and g-factor for the principal bands of the Red- and Violet-Systems of CN at T = 100K

Frequency [cm^{-1}]	Wavelength [μm]	Band v_{up}-v_{low}	g-pump(a) (Black Body) [s^{-1}]	g-pump(b) (Solar Spectr.) [s^{-1}]	g-factor(c) [s^{-1}]
X– X					
2046.06860	4.89	1 – 0	7.39893E-05	6.01868E-05	5.83049E-02
2020.27039	4.95	2 – 1	2.44332E-17	2.11017E-17	1.88501E-02
1994.07666	5.01	3 – 2	8.77966E-30	7.38336E-30	5.53420E-03
1966.75524	5.08	4 - 3	4.09835E-42	3.31281E-42	1.39206E-03
A – X					
9112.35367	1.10	0 – 0	8.14963E-02	7.81244E-02	5.71131E-02
10899.58527	0.92	1 – 0	5.84483E-02	5.65319E-02	4.16103E-02
7071.03416	1.41	0 – 1	8.52537E-15	9.47426E-15	1.89977E-02
10619.47491	0.94	2 – 1	7.45876E-15	7.07029E-15	1.02854E-02
6841.39430	1.46	1 – 2	1.94463E-27	2.17810E-27	9.91392E-03
B – X					
25802.99977	0.39	0 – 0	1.31079E-01	5.36814E-01	5.03600E-02
25877.86856	0.39	1 – 1	2.39486E-15	1.03069E-15	3.35679E-03
23760.31929	0.42	0 – 1	1.87367E-14	2.45038E-14	3.16959E-03
23868.40998	0.42	1 – 2	1.03960E-27	1.09851E-27	4.42462E-04
27926.75792	0.36	1 – 0	8.30321E-03	4.26645E-03	4.33029E-04

g-pump computed considering a model of Black Body at 5770 K.
g-pump computed considering a real solar spectrum (Hase + Kurucz)
g-factor computed from g-pump obtained with real solar spectrum

$$g_i = g_{pump}(l')\cdot\frac{A_{21}}{A_{tot}(l')} \qquad A_{tot}(l') = \sum_i A_{21} \tag{17}$$

In Table 6 the computed pumping rates and g-factors for the principal vibrational bands are reported.

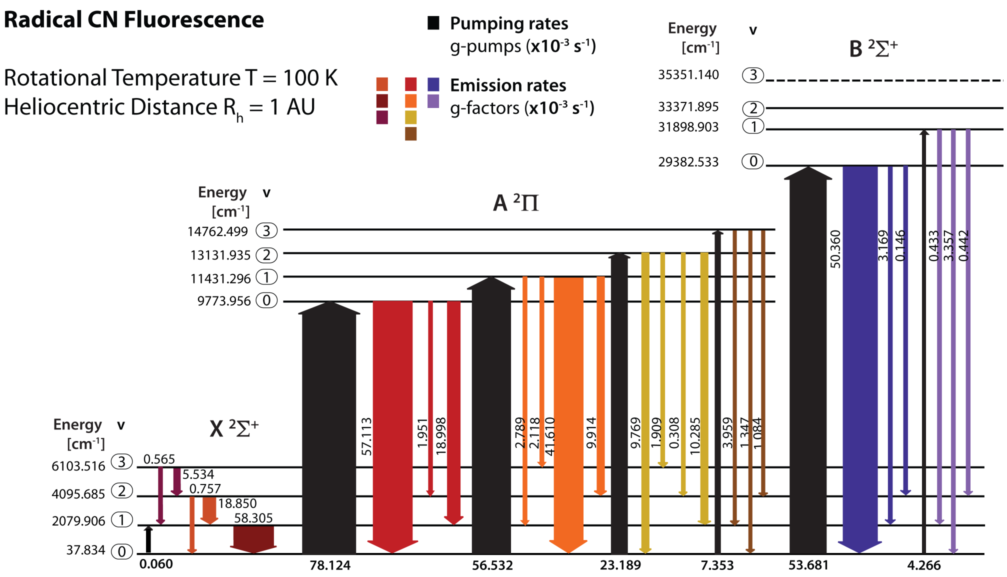

Figure 25
Full non-resonance fluorescence diagram for CN in a comet evaluated at 1 au and with rotational temperature at 100 K is shown. Pumping rates are shown in black and are calculated considering a realistic Solar model. Emission rates, shown in the different colors (red/brown/yellow/purple/violet), are calculated by the multiple cascades down to the ground-vibrational level, considering the level-by-level branching ratios. The graph shows only pumps and emissions with vibrational rates higher than 10^{-3} s^{-1} .

We report the computed pumping both for the real solar spectrum and for a theoretical Black Body irradiance model at T = 5770 [K], as explanatory examples, to show the power of using a real solar spectrum. The fluorescence g-factors reported in the Table 6 are computed from pumping by the real solar spectrum. In Figure 25 the pumping rates for the main vibrational bands and the fluorescence emission rate for the CN radical are shown as complementary descriptions.

Chapter 7

CN Fluorescence Analysis

The principal vibrational excitation process for radical CN molecules is by direct absorption of solar radiation. Once excited, the CN molecules emit photons at IR wavelengths through fluorescence cascade, either to the ground vibrational state (*resonance fluorescence*) or to various intermediate energy levels (*non-resonance fluorescence*) with relative emission efficiencies given by their branching ratios.

As already discussed in Chapters 2 and 5, collisions are usually considered responsible for thermalizing rotational levels in the intermediate coma (50 km < r < 10^4 km). Optical trapping of pure rotational emissions can extend the thermalized region significantly (e.g., for H_2O). Owing to the two 1″ angular diameter fibers of the GIANO spectrograph placed at a fixed center-to-center distance of 3″, we sampled a nucleus-centered area of about ~700 km diameter and an area placed at about ~2100 km far from the nucleus, at the comet on February 2. We assumed the rotational population in the ground vibrational level of radical CN to be maintained at LTE (see below for further discussion).

With GIANO we detected many CN fluorescent emission lines. Using the collected spectral data and the powerful theoretical model described in Chapter 6, it was possible to characterize CN in comet Lovejoy with high precision.

We detected 45 strong lines of the vibrational (0-0) band of CN red system near the 1.09 μm spectral region, along with many other emission lines across the echellogram: strong ro-vibrational lines of the (1-1) band near 1.13 μm, of the (0-1) and the (1-2) bands near 1.4 μm, and weaker features of the (1-3) band near 2.06 μm. The observed vibrational bands and the corresponding GIANO spectral orders are listed in Table 7. Here, I will present the detailed analysis of spectral lines of the (0-0) vibrational band of the CN Red-System, detected in order 70 of the GIANO echellogram. A complete analysis of all spectral orders (70, 68, 54, 53, 37) in which CN emission lines are present is being prepared for publication (Faggi et al, 2017 in prep).

Table 7. Spectral Bands of the $A^2\Pi$ - $X^2\Sigma^+$ Red System of CN Detected in comet C/2014 Q2 (Lovejoy).

Frequency [cm^{-1}]	Wavelength [μm]	Band v_{up}-v_{low}	GIANO Spectral Order
9112.354	1.09	0 – 0	70
8857.569	1.13	1 – 1	68
7071.034	1.41	0 – 1	54
6841.394	1.46	1 – 2	53
4853.368	2.06	1 – 3	37

A quantitative description of 45 emission lines of the (0-0) vibrational band detected in order 70 (near 1.09 μm) appears in Table 8. The first column reports the frequency of the observed line, and the second column shows the identification (N, J, p) of the contributing transitions (see Chapter 6 for details). On the left side of the second column, the percentage contributed by a modelled transition to the measured detected intensity at GIANO's resolving power is reported. The third column (E_{rot}, cm^{-1}) represents the effective lower state rotational energy of the observed emission; it is obtained from the mean energy of lower states (weighted by their fractional intensity contributions) of modelled transitions that contribute to the detected line. The last four columns represent respectively the emission efficiency (g-factor, s^{-1}), the transmittance affecting the detected emission, the implied flux at the top of the atmosphere [W m^{-2}], and the CN production rate obtained from that emission using the best-fit rotational analysis [s^{-1}] (see §7.1).

Table 8. The $A^2\Pi$-$X^2\Sigma^+$ Red-System of CN. Parameters for spectral lines of the 0-0 band detected in C/2014 Q2. (Lovejoy).

k (cm^{-1})	**Line ID (a) [%] $(N, J, p)_{up}$ $(N, J, p)_{down}$**	**E_{rot} (cm^{-1})**	**g-factor ($10^{-4}s^{-1}$)**	**Tran.**	**Flux TOA ($10^{-18}W\ m^{-2}$)**	**Q $_{CN}$ ($10^{25}s^{-1}$)**
9150.2594	14.7% (8, 7.5, f) (7, 7.5, e) 18.0% (8, 7.5, f) (7, 6.5, f) 16.2% (6, 5.5, f) (5, 4.5, f) 16.9% (6, 5.5, f) (5, 5.5, e) 16.3% (7, 6.5, f) (6, 6.5, e) 18.0% (7, 6.5, f) (6, 5.5, f)	80.57	23.73	0.98	18.63	1.82
9150.1523	11.4% (5, 4.5, f) (4, 3.5, f) 13.8% (5, 4.5, f) (4, 4.5, e) 11.0% (8, 7.5, f) (7, 7.5, e) 13.5% (8, 7.5, f) (7, 6.5, f) 12.1% (6, 5.5, f) (5, 4.5, f) 12.6% (6, 5.5, f) (5, 5.5, e) 12.2% (7, 6.5, f) (6, 6.5, e) 13.4% (7, 6.5, f) (6, 5.5, f)	69.80	31.65	0.98	21.13	1.55
9149.8658	16.2% (9, 8.5, f) (8, 8.5, e) 22.4% (9, 8.5, f) (8, 7.5, f) 19.4% (5, 4.5, f) (4, 3.5, f) 23.3% (5, 4.5, f) (4, 4.5,e) 18.6% (8, 7.5, f) (7, 7.5, e)	88.50	18.55	0.99	14.01	1.75
9149.0692	18.6% (10, 9.5, f) (9, 9.5, e) 28.7% (10, 9.5, f)(9, 8.5, f) 30.9% (4, 3.5, f) (3, 3.5, e) 21.9% (4, 3.5, f) (3, 2.5, f)	92.35	13.43	0.99	8.68	1.50
9148.0938	36.3% (11, 10.5, f) (10, 9.5, f) 40.3% (3, 2.5, f) (2, 2.5, e) 23.3% (3, 2.5, f) (2, 1.5, f)	82.78	9.43	0.99	7.49	1.84
9146.9301	71% (2, 1.5, f) (1, 1.5, e)	3.78	4.17	0.85	4.69	2.61
9146.7361	19.2% (12, 11.5, f) (11, 11.5, e) 36.5% (12, 11.5, f) (11, 10.5, f) 12.9% (2, 1.5, f) (1, 0.5, f) 31.5% (2, 1.5, f) (1, 1.5, e)	140.56	8.69	0.92	5.36	1.43
9141.6439	66.7% (1, 0.5, e) (1, 0.5, f)	3.78	2.98	0.99	2.20	1.71
9139.3559	67.4% (2, 1.5, e) (2, 1.5, f)	11.34	4.50	0.99	1.96	1.01
9136.8023	70.4% (3, 2.5, e) (3, 2.5, f)	22.69	7.11	0.99	5.20	1.70
9133.9896	61.3% (4, 3.5 e) (4, 3.5, f)	34.19	10.06	0.67	5.27	1.22
9130.8784	75.5% (5, 4.5, e) (5, 4.5, f)	56.71	10.19	0.96	7.04	1.60
9127.5130	77.1% (6, 6.5, e) (6, 5.5, f)	86.12	10.96	0.99	6.95	1.47

9123.8699	76.4% (7, 6.5, e) (7, 6.5, f)	133.91	7.41	0.97	4.23	1.33
9119.9229	81.8% (8, 7.5, e) (8, 7.5, f)	136.10	10.65	0.99	7.19	1.57
9117.4272	69.8% (9, 9.5, e) (8, 8.5, e)	198.83	6.98	0.99	2.82	0.94
9116.1279	76.4% (8, 8.5, e) (7, 7.5, e)	174.62	7.05	0.99	5.72	1.89
9115.8537	60.6% (9, 8.5, e) (9, 8.5, f)	144.79	13.66	0.99	9.25	1.58
9115.6960	83.4% (9, 8.5, e) (9, 8.5, f)	170.12	9.92	0.99	8.26	1.94
9115.1080	96% (4, 3.5, f) (5, 4.5, f)	89.15	3.53	0.99	2.54	1.68
9114.3892	82.1% (7, 7.5, e) (6, 6.5, e)	146.48	6.96	0.99	4.07	1.36
9111.1717	84.8% (10, 9.5, e) (10, 9.5, f)	207.91	8.93	0.99	5.87	1.53
9109.4989	99.7% (5, 5.5, e) (4, 4.5, e)	40.97	5.68	0.88	4.75	1.95
9108.2436	100% (5, 4.5, f) (6, 5.5, f)	79.39	3.93	0.94	3.18	1.89
9106.3587	52.2% (11, 10.5, e) (11, 10.5, f) 39.4% (4, 4.5, e) (3, 3.5, e)	160.18	12.60	0.99	7.74	1.43
91028378	100% (3, 3.5, e) (2, 2.5, e)	11.35	4.66	0.99	2.56	1.28
9101.1854	41.9% (6, 5.5, f) (7, 6.5, f) 51.7% (12, 11.5, e) (12, 11.5, f)	215.63	8.83	0.82	5.45	1.44
9098.8576	99% (2, 2.5, e) (1, 1.5, e)	15.03	4.03	0.98	2.40	1.39
9093.6801	100% (7, 6.5, f) (8, 7.5, f)	136.09	4.41	0.98	4.16	2.20
9091.3559	16.5% (2, 2.5, f) (2, 2.5, e) 10.7% (2, 2.5, f) (2, 1.5, f) 27.2% (4, 4.5, f) (4, 4.5, e) 11.1% (4, 4.5, f) (4, 3.5, f) 23.1% (3, 3.5, f) (3, 3.5, e) 11.5% (3, 3.5, f) (3, 2.5, f)	25.41	28.68	0.98	17.94	1.46
9091.2769	25.2% (2, 2.5, f) (2, 2.5, e) 16.3% (2, 2.5, f) (2, 1.5, f) 41.6% (4, 4.5, f) (4, 4.5, e) 16.9% (4, 4.5, f) (4, 3.5, f)	26.84	18.81	0.97	11.76	1.46
9090.5805	16.1% (1, 1.5, f) (1, 1.5, e) 16.8% (1, 1.5, f) (1, 0.5, f) 50.0% (5, 5.5, f) (5, 5.5, e) 17.1% (5, 5.5, f) (5, 4.5, f)	39.30	17.71	0.99	11.48	1.51
9089.4769	77.4% (6, 6.5, f) (6, 6.5, e)	79.43	12.22	0.99	8.85	1.69
9087.8959	79.6% (7, 7.5, f) (7, 7.5, e)	105.90	11.82	0.97	7.87	1.55
9085.9003	60.3% (8, 8.5, f) (8, 8.5, e)	145.25	15.51	0.95	10.03	1.51

9083.4112	83.8% (9, 9.5, f) (9, 9.5, e)	170.17	10.24	0.95	6.84	1.56
9080.5145	84.9% (10, 10.5, f) (10, 10.5,e)	207.97	9.08	0.99	5.17	1.33
9079.9158	67.8% (2, 2.5, e) (3, 2.5, f)	22.69	4.92	0.99	3.70	1.76
9076.3802	64.3% (3, 3.5, e) (4, 3.5, f)	41.79	6.44	0.84	3.78	1.37
9072.3790	41.7% (4, 4.5, e) (5, 5.5, e) 58.2% (4, 4.5, e) (5, 4.5, f)	57.58	7.11	0.98	4.42	1.45
9067.9197	46.0% (5, 5.5, e) (6, 6.5, e) 54.0% (5, 5.5, e) (6, 5.5, f)	79.41	8.16	0.97	5.73	1.64
9063.0065	49.3% (6, 6.5, e) (7, 7.5, e) 50.7% (6, 6.5, e) (7, 6.5, f)	105.88	8.28	0.97	5.61	1.59
9057.6299	12.3% (3, 3.5, f) (5, 4.5, f) 45.8% (7, 7.5, e) (8, 8.5, e) 41.9% (7, 7.5, e) (8, 7.5, f)	126.78	9.33	0.93	6.74	1.69
9051.8386	56.4% (8, 8.5, e) (9, 9.5, e) 43.6% (8, 8.5, e) (9 8.5, f)	170.15	7.41	0.86	4.44	1.40
9045.5965	58.3% (9, 9.5, e) (10, 10.5, e) 41.7% (9, 9.5, e) (10, 9.5, f)	207.95	6.55	0.94	3.46	1.24
(a) The spectral lines with percentage >10% are reported in the second column of the table.						

Sky emission lines do not contaminate CN emission lines in order 70 of GIANO echellogram (cf. Chapter 4), so we used all 45 emission ‘lines’ to retrieve a best-fit rotational temperature and production rate. As an example, we next show the retrieval obtained for the nucleus-centered region of comet Lovejoy.

7.1 Rotational Temperature

The rotational temperature (T_{rot}) of the CN molecule was evaluated following the same procedure as for water: through the slope analysis and the correlation analysis (cf. Chapter 5). T_{rot} is the temperature that describes the population distribution of rotational levels in the ground vibrational state; its retrieval is essential to obtain a correct production rate. In the medium coma (50 km $\leq$ r $\leq$ 10^4 km), we assumed that the ground ro-vibrational states of CN are well described by local thermodynamic equilibrium (LTE) at a defined temperature.

For H_2O, it was established that electron collisions, coupled with optically thick pure rotational transitions, control the rotational population in the intermediate coma, rendering it equilibrated with an effective temperature (Xie and Mumma, 1992b). For CN, the mechanism(s) that control its rotational distribution must be considered with care[25].

For now, the goodness (or not) of the fit will suffice to determine whether or not the assumption of LTE is valid. The population distribution P_i of rotational levels, according to the Boltzmann statistic, is described by the equation 3 in Chapter 6. Following equation 4 in Chapter 5, it is possible to retrieve a total CN production rate from an individual line by comparing the modeled line intensities (g-factors) with the observed line fluxes.

The observed line fluxes depend directly on the population of rotational levels in the upper states and indirectly on the temperature dependent distribution within the ground state. At the correct rotational temperature (T_{rot}), the ratio between the measured flux and g-factor of the line should be almost the same for all the detected lines, so it should be independent of E_{rot}. The retrieval of the rotational temperature is most reliable when a wide range of rotational energy states is sampled. The two methods allowed retrieval of the rotational temperature and production rate.

Figure 26 a shows results from the slope analysis and correlation analysis methods applied to the 45 detected CN lines of the (0-0) vibrational band. The left panel reports the line-by-line slope analysis excitation method, in which the measured CN line intensities are compared with the modeled g-factors computed with the quantum mechanical fluorescence model developed by Faggi et al (2017, in prep). By comparing the 45 observed line fluxes with the modeled fluxes for different assumed rotational temperatures, the best-fit solution

---

[25] The rotational distribution could be explained for example owing to the fluorescence equilibrium process produced by an extremely high pumping rate and relatively low excitation rate with electrons. However the relative importance varies with respect the distance from the nucleus.

(slope zero) provides a measure of T_{rot} (246 ± 12 K); the 45 Q's for this solution agree with the mean Q within their line-by-line errors, confirming the goodness-of-fit.

The confidence limits for the slope were selected considering the higher uncertainty between the stochastic error and the variance error (standard error) (cf., chapter 5). The stochastic error describes the uncertainty produced by photon noise while the variance error describes the spread of the derived quantities around the slope line. For this solution, the stochastic error for the slope (± 1.02×10^{-7}) corresponds to an interval of about ± 12 K in temperature [the dotted lines show slopes with magnitude 1.02×10^{-7} s^{-1}/cm^{-1} (Fig. 26, top left panel)]. For the correlation analysis the limits were assumed the same as for the slope analysis.

The complementary excitation method (the correlation analysis) and slope analysis method are compared in the upper right panel of Figure 26 a. The correlation analysis defines the most probable temperature as one that provides the best (maximum) correlation among intensities in the measured and synthetic spectra in this case, returning a best-fit value of $T_{rot} \sim (228 \pm 12)$ K. For the correlation analysis the confidence limits were assumed the same as for the slope analysis, determined by the higher uncertainty between the stochastic error and the variance error in evaluating confidence limits for the slope. Combining results from the two methods provides a weighted mean rotational temperature of (237 K ± 12) K.

Interestingly, the rotational temperature of the radical CN retrieved in comet Lovejoy is higher compared with the temperatures found in the cometary coma, that usually ranges from 50 to 150 K (see e.g. water measurements reported in (Gibb et al., 2002)). However, product species such as radical CN are distributed relatively farther from the nucleus compared with parent species (e.g. water) (cf., Chapter 1); for this reason, they are characterized by flatter spatial profiles.

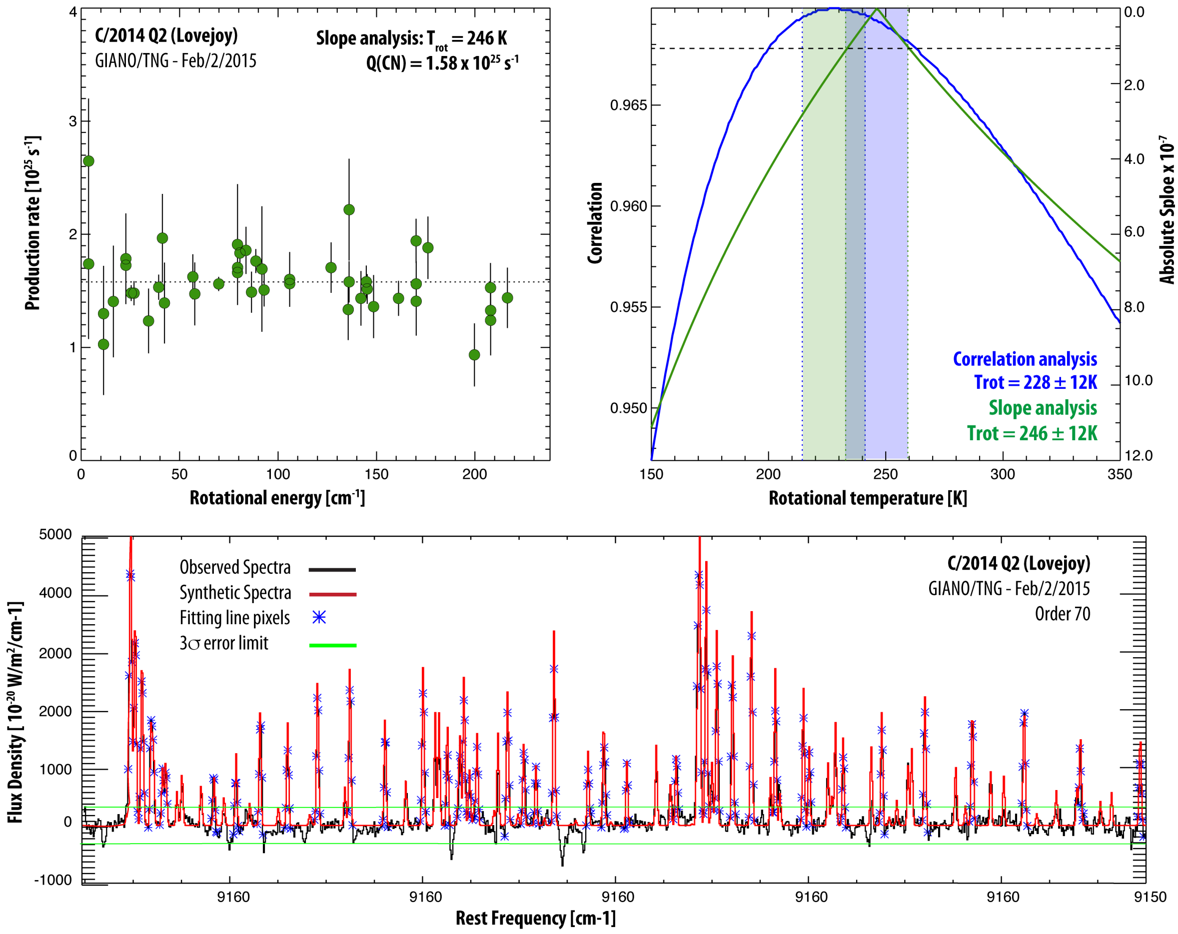

Figure 26 a.

Determination of the rotational temperature of CN in comet Lovejoy.

Upper Left: The slope analysis method is shown. The x-axis represents the mean lower rotational energy E_{rot} [cm^{-1}] of the principal pumping transitions that contribute to excitation of an observed line. The y-axis represents the cyanide production rate [Q(CN), units of 10^{25} s^{-1}] inferred for that line from the synthetic fluorescence model at T_{rot}. If all lines provide the same estimated value for Q(CN), the slope of this graphic will be zero, and the value of T_{rot} assumed for that fit has described the rotational population adequately. [Methodology: A test value of T_{rot} is assumed and the summed g-factor for each line is calculated for the value assumed; a linear fit to the data provides a slope. The process is continued at T = 1 K intervals, over the range 50-350 K. The graphic shows the line-by-line values of Q(CN) (green dots) returned for T_{rot} = 246 K, and the linear fit (dotted line; slope = zero). The slopes with absolute value 1.02×10^{-7} corresponding to the 1-σ limits in the best-fit slope (= 0.0) are also shown.

Upper Right: Comparison of best-fit values for T_{rot} obtained from the slope and correlation analyses. The x-axis represents the rotational temperature T_{rot} [K]. The scale for the correlation coefficient appears on the left y-axis and the scale for absolute values of slope appear on the right y-axis. The best-fit T_{rot} values correspond to the maximum coefficient in the correlation analysis (blue) and to the null value in the slope analysis (green). The derivation of confidence levels is described in the text.

Bottom: The spectrum of comet Lovejoy (black) is compared with a synthetic spectrum (red) obtained from the quantum mechanical fluorescence model using the best-fit value for T_{rot} (246 K) obtained from the slope analysis method. The difference spectrum (measured – synthetic), is shown below (blue).

So, probably most of the radical CN molecules emissions sampled in our beam reside far from the nucleus where the kinetic temperatures are higher than in the near-nucleus coma where most of the primary volatiles sampled by a pencil beam of small diameter lie. Kinetically fast H-atoms are produced and thermalized at these greater distances from the nucleus, introducing higher collisional heating there; consequently, higher temperatures are expected for CN than for H_2O (Bockelée-Morvan et al., 2004; Xie and Mumma, 1992b).

These high rotational temperatures could also be favored by the very strong pumping rates from the electronic ground state ($X^2\Sigma^+$) to the excited states ($A^2\Pi$ and $B^2\Sigma^+$) (e.g, Chapter 6). The subsequent fluorescence cascade into the ground state produces a net pumping of the rotational levels into higher-energy states. This process competes with radiative cooling of such levels via pure rotational transitions, assisted by the high escape-to-space probability of the emitted quanta (unlike the case for H_2O, the medium is probably optically thin to sub-mm quanta emitted by rotational decay of CN, owing to the low CN density). The Einstein spontaneous emission coefficient A is proportional to frequency as J^3, so it increases as the energy of levels increases until a balance is obtained between fluorescence pumping and radiative cooling (fluorescence equilibrium, cf. Weaver and Mumma 1984). It could also be possible that such high temperature could partially be the result from formative conditions of CN radical in the cometary coma. The photo-dissociation of a precursor species (e.g. HCN, C_2N_2, etc.) can produce radical CN in excited ro-vibrational states; moreover some energy released by the dissociation is taken by the products partly in the form of kinetic energy. At this writing, insufficient laboratory data exist to assess the details of this partitioning – it remains a need to further interpret aspects of the fragment CN in terms of the possible precursor species.

In retrieving the rotational temperature, our fluorescence model is not an equilibrium model that considers both radiative and collisional effects. A Monte-Carlo simulation in the sampling beam along the line of sight will be needed to compute all these effects - including the variation in kinetic temperature with respect to the distance from the nucleus.

Nevertheless, the excellent agreement between the observed cometary spectrum and the fluorescence model (see Figure 26, bottom panel) validates the assumption of LTE for characterizing the ground state rotational distribution in terms of a temperature (T_{rot}). Future discussions will be presented in a paper on CN analysis for comet Lovejoy.

7.2 CN, ^{13}CN, C^{15}N production rates

Production rates for CN and upper limits for its isotopologues were evaluated using the best-fit rotational temperature derived from slope analysis. In Table 8, a detailed description of the 45 detected lines and their production rates is reported. Considering the slope analysis rotational temperature (T_{rot} = 246 K), we obtained a total CN production rate of Q(CN) = (1.567 ± 0.026) x 10^{25} [s^{-1}] from the A-X (0-0) band near 1.09 μm; using the same rotational temperature we retrieved 3-σ upper limits for its isotopologues: Q(^{13}CN) < 6.33 x10^{23} [s^{-1}] and Q(C^{15}N) < 6.27 x10^{23} [s^{-1}]. These values are obtained from the weighted mean of the individual line production rates and the uncertainties are selected by comparing the standard deviation from the mean of production rates with the error due to photon noise, and taking the higher value. For the sake of completeness, in Figure 26 b the cometary spectrum of comet Lovejoy in order 70 of GIANO echellogram, together with the model of continuum affected by terrestrial transmittance and the synthetic spectra for fluorescent CN, C^{15}N and ^{13}CN emissions, necessary to identify and characterize the detected lines, are shown.

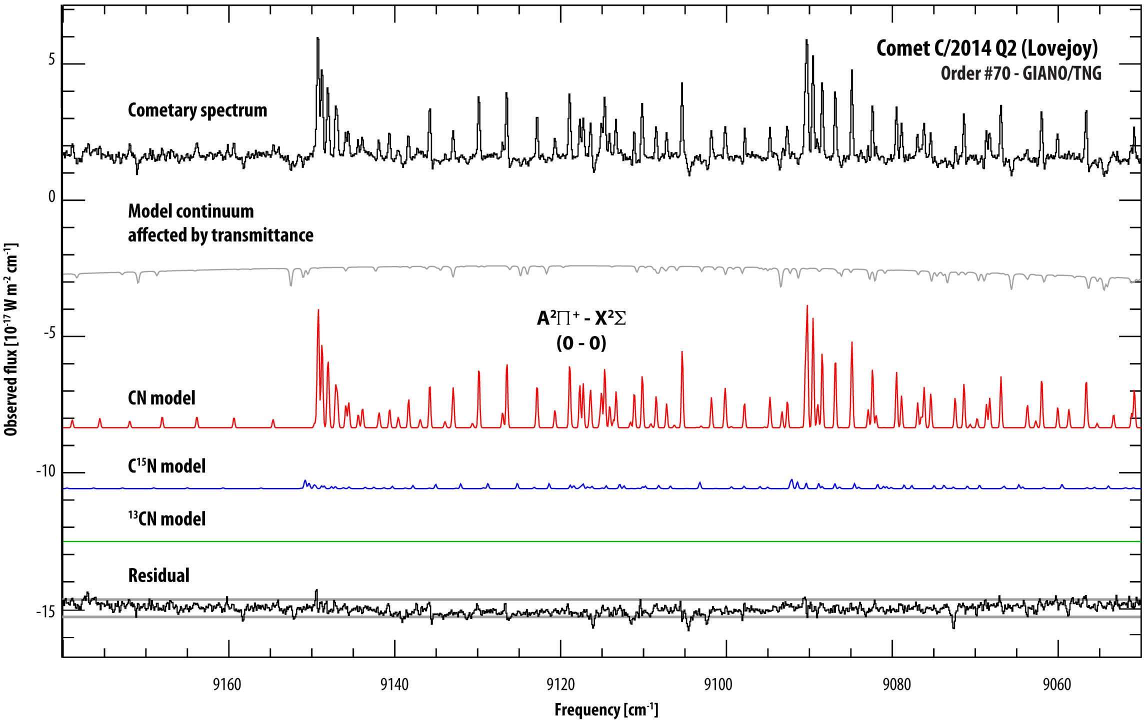

Figure 26 b.

Cometary spectra from order 70 of a GIANO echellogram is shown. The observed fluxes [10^{-17} Wm^{-2}/cm^{-1}] are shown vs. frequency [cm^{-1}]. The topmost black trace shows the calibrated cometary spectrum, the lower gray trace represents model of continuum affected by terrestrial transmittance. The lower colored three traces are the synthetic models of cometary CN fluorescence and isotopes used to fit the cometary spectrum (CN is in red, $C^{15}N$ is in blue and ^{13}CN is in green). These latter three synthetic spectra are shown shifted downward along the y-axis relative to the measured cometary spectrum, for clarity. We identified cometary emission lines from the 0-0 band of CN the red-system by comparing the molecular residual cometary spectrum (after transmittance subtraction) with the spectra of modeled CN fluorescence and isotopes.

7.3 Isotopic ratios $^{12}C/^{13}C$ and $^{14}N/^{15}N$

Isotopic fractionation in comets (cf., Chapter 3) is a powerful tool for constraining the primitive conditions of proto-solar nebula. Pre-cometary material and the assembled nucleus experienced diverse physical conditions and went through different chemical evolutionary processes, whose fingerprints remain stored even today in their nuclei composition as cosmic fingerprints (see Figure 8, Chapter 1).

The carbon and nitrogen isotopic ratios retrieved (from CN and C_2) in 18 comets with 24 heliocentric distances showed a trend of uniform values of $^{12}C/^{13}C$ ratio around the terrestrial value ~90, and an agreement of $^{14}N/^{15}N$ ratio values around ~148 showing a profound discrepancy between cometary and telluric values (Fig. 12b, chapter 3, after (Jehin et al., 2009).

The values retrieved from our measurements of the CN Red-system in comet Lovejoy are not sufficiently accurate to test these values. For further discussion, see Chapter 8.

7.4 CN mixing ratio

The interpretations of production rate measurements fro daughter species bumps into many issues regarding models of kinematic outgassing. In 1957, Leo Haser introduced a simple formulation of cometary outgassing, in which the primary cometary gases are released from the nucleus at a constant rate, in a spherically symmetric fashion about the nucleus, and flow outward in a radial expansion with constant velocity. The distribution of secondary species, whose density is described by equation 1 in §1.3.2, was considered as the product of photo-dissociation of a primary molecule. The model limitation consists in considering an outward spherical expansion also for product species that are produced by the extended source of parent molecules (Keller and Lillie, 1974). In reality velocities of product species are randomly distributed (in the center-of-mass frame of the parent molecule, which is however moving outward from the nucleus) and only a Monte Carlo model can describe the distribution of product species, correctly.

However, with these simple assumptions and considering the dependence of numerical density distributions of fragments in the coma with respect to the heliocentric distance and the nucleocentric distance[26] it is possible to describe the fragment distribution in the coma (Yamamoto, 1981). Defining $\lambda_p = v_p\tau_p$ and $\lambda_d = v_d\tau_d$ the molecular scale lengths for the parent and the daughter specie respectively (with outflow velocities v_p and v_d) and assuming

---

[26] Numerical density of parent species: $n_p = r^{-2}\, Rh^{-2}$
Numerical density of first product species: $n_d = r^{-1}\, Rh^{-4}$
Where r is the nucleocentric distance and Rh the heliocentric distance.

the condition in which the cometary nuclear radius is << λ_p, λ_d, the molecular density described in equation 1 in §1.3.2 can be used (Keller and Lillie, 1974). The theoretical column density evaluated as the integration of numerical density along the line of sight, can be written analytically with respect to the nucleocentric projected distance as function of the zero order and second kind Bessel function. A further integral on the surface beam provides the number of daughter molecules seen in the FOV (Keller and Lillie, 1974). These calculations provided the first step in the (Yamamoto, 1981) evaluation of "f(x)" the normalized fraction of molecules in the beam, essential to correct our production rate.

We adopted the Yamamoto formulation to retrieve f(x) and correct for the radical CN production rate in the nuclear center region, where the conditions of using equation 1 in §1.3.2 were valid. We could not correct for the fiber "aperture loss", as we did for the water retrieval, evaluating the Qscale, because a detailed molecular outgassing model for radicals in the coma was required in order to evaluate the rescaled f(x) in the off nucleus positions (*coma up* and *coma down*).

In order to test HCN as a parent precursor of radical CN, we adopted the lifetime of the CN parent as τ_p = 70,000 [s] (e.g., HCN lifetime (Magee-Sauer et al., 1999)) and considering the lifetime of the CN product about τ_d = 220,000 [s] (McKay et al., 2014), our retrieval for the fraction of molecules sampled in the 1" fiber beam is: $f(x)^{CENTER} = 1.34 \times 10^{-5}$. Through the slope analysis we obtained a CN column density of about $\sigma^{CENTER}(CN) = (3.31 \pm 0.05)\times10^{16}$ [mol m^{-2}] thus the total radical CN production rate according with the correct $f(x)^{CENTER}$ is $Q^{tot}(CN) \sim 2.23\times10^{27}$ [mol s^{-1}].

However, to identify the parent scale length that reproduce the observed CN abundance we also adopted the Festou vectorial model (http://www.boulder.swri.edu/wvm/). The model assumes the following hypothesis:

(i) most of the coma is collisionless,

(ii) the product species are formed by photo-dissociation of primary volatiles, and

(iii) part of the energy released in the photolysis of the parent is converted into kinetic energy for the daughter molecule that is ejected into the coma in any direction. Introducing as input parameters the primary and product life times, τ_p and τ_d respectively, the retrieved production rate corrected for the fraction of molecules in the beam [Q^{tot}(CN)], the heliocentric (R_h) and geocentric (Δ) distances, and the excitation rate (g-factor, 4.57 x 10^{-2} [photon/s/mol]), we derive a 1D theoretical column density over a nucleocentric distance of about 10^6 km.

In order to correct for seeing loss, following the approach in Chapter 5, we create a theoretical 2D outgassing function based on Festou theoretical column density, describing the flux at top of the atmosphere, and we convolved it with a 2D-gaussian PSF function describing the effect of the seeing (see Figure 23, Chapter 5). The ratio between the theoretical flux with respect to the seeing-affected flux, sampled by the fiber FoV, defines the amount of flux lost by the seeing-effect. We derived a seeing correction of about ~1.035, leading us to conclude that the total CN production rate is about Q(CN) ~2.3 x 10^{27} [mol s^{-1}].

From cyanide production rate we derived the relative abundance with respect to water as described in equation 2 in §1.3.2:

$$\frac{Q_{CN}}{Q_{H_2O}} \times 100\% = 0.46\%$$

Chpater 8

Conclusions

8.1 Summary of results

The collected data allowed us to obtain the following results:

Water:

- We detected 52 water lines in the 2 μm and 1.4 μm regions of the GIANO echellogram. These lines belong to 8 vibrational water bands. In the 2 μm region, across orders #39, #40, #41, we detected two bands of non-resonance fluorescence (111-100 and 021-010) and one band (011-000) of resonance fluorescence. In the 1.4 μm region, across orders #53, #54, #55, #56, we detected three non-resonant bands (201-100, 111-010, and 210-010), and two resonant bands (200-000 and 101-000).
- Through the slope analysis method we obtained a rotational temperature T_{rot} = (90 ± 20) K. This is the temperature in the ground ro-vibrational state that best fitted (with slope zero) the ratio of observed and predicted fluxes (F_{obs} / F_{pred}) with respect to the mean value of rotational state energies in the ground vibrational state.
- For T_{rot} = 90K, we achieved a total water production rate of $Q(H_2O)= (3.11 \pm 0.14) \times 10^{29}\ s^{-1}$ from the nucleus-centered measurement, , before seeing corrections are applied. The production rates obtained for ortho-water and para-water are $Q(H_2O)^{ORTHO}=(2.33 \pm 0.11) \times 10^{29}\ s^{-1}$ and $Q(H_2O)^{PARA}= (0.87 \pm 0.21) \times 10^{29}\ s^{-1}$, respectively.
- To correct for 'fiber losses' due to atmospheric seeing, we evaluated the Growth Factor for a fiber-fed spectrograph (see Chapter 5). Our evaluation ($Q_{scale}{}^{GIANO}$=1.6)

allowed us to obtain a seeing-corrected water production rate of Q(H_2O)= (4.98 ± 0.22) x 10^{29} s^{-1}, in agreement with (Paganini et al., 2015).

- From our measurements of ortho- and para-water production rates we computed an OPR = (2.70 ± 0.76). The confidence limits obtained with our para-H_2O retrieval were not small enough to enable an accurate test of the nuclear spin temperature.

Radical CN:

- We detected 45 emission lines of (0-0) band of radical CN Red System ($A^2\Pi$ – $X^2\Sigma^+$) near 1.09 μm, in order #70 of GIANO echellogram. Multiple emissions of radical CN were also detected across four other orders of GIANO: lines from the (1-1) band around 1.13 μm were present in order #68, lines from the (0-1) and (1-2) bands around 1.4 μm were present in orders #54 and #53 (together with water lines), and several lines of the (1-3) band around 2.06 μm were seen in order #37 (see Table 7 of Chapter 7).
- In this work we showed the retrieval performed on order #70 of GIANO echellogram. A detailed analysis of CN detections in comet Lovejoy will be presented in a future paper. Adopting the slope analysis method for radical CN lines detected in order#70, we obtained a rotational temperature T_{rot} = (246 ± 12) K for the ground ro-vibrational state of CN ($X^2\Sigma^+$, v = 0). This temperature provided the best fit (with slope zero) of ratios of observed fluxes to modelled g-factors (F_{obs} / F_{pred}) with respect to E_{rot}.
- From the nucleus-centered spectral extract and T_{rot} = 246K, we retrieved a total CN production rate Q(CN)= (1.567 ± 0.026) x 10^{25} [s^{-1}]. The 3-σ upper limits obtained for the isotopes ^{13}CN and C^{15}N are Q(^{13}CN) ~ 6.33 x10^{23} [s^{-1}] and Q(C^{15}N) ~ 6.27 x10^{23} [s^{-1}] respectively. These production rates assumed a primary volatile distribution for CN, so their absolute values are much too small but their ratios are

valid.

- Isotopic ratios $^{12}C/^{13}C$ and $^{14}N/^{15}N$ were evaluated from the retrieved upper limits for CN isotopologues. The carbon and nitrogen isotopic ratio upper limits obtained in comet Lovejoy are $^{12}C/^{13}C > 24.8$ and $^{14}N/^{15}N > 25.0$. Our values for carbon and nitrogen isotopic ratios ($^{12}C/^{13}C$, $^{14}N/^{15}N$) are not sufficiently accurate to constrain the trends observed among comets (see Figure 12b, Chapter 3).
- To obtain radical CN global production rates from the nucleus-centered column density, we adopted Yamamoto's formulism for spatial profiles of product species. Assuming the lifetime of CN parent $\tau_p = 70{,}000$ [s] and considering the lifetime of CN product to be $\tau_d = 220{,}000$ [s], our retrieval for the fraction of coma molecules sampled in the 1" fiber beam (nucleus-centered) is: $f(x)^{CENTER} = 1.34 \times 10^{-5}$. Applying a "fiber loss' correction factor, the global cyanide production rate is $Q^{tot}(CN) \sim 2.3 \times 10^{27}$ [mol s^{-1}]. The retrieved mixing ratio is $Q(CN) / Q(H_2O) = 0.46\%$.

8.2 Comparison with other measurements for comet Lovejoy

8.2.1 Water production rate and D/H ratio

(Biver et al., 2016) reported a mean value of water production rate [$Q(H_2O) \sim (5.0 \pm 0.2) \times 10^{29}\ s^{-1}$] for the interval 29 January - 3 February 2015, in agreement with our retrieval ($(4.98 \pm 0.22) \times 10^{29}\ s^{-1}$, and that of (Paganini et al., 2015). Biver et al. combined measurements of 18 cm maser emission from radical OH (January 2015, Nançay radio telescope) and detections of the (1_{10}-1_{01}) line in $H_2{}^{16}O$ and $H_2{}^{18}O$ (556.9 GHz and 547.7 GHz, respectively), acquired with the Odin sub-millimeter space observatory).

(Biver et al., 2016) reported an average value for deuterated water production [$Q(HDO) \sim (15.3 \pm 4.1) \times 10^{25}\ s^{-1}$], based on a 4-$\sigma$ detection of the (2_{11}-2_{12}) line of HDO at 241.561

GHz (IRAM 30m telescope) between 13 and 24 January 2015. Based on these multiple measurements they reported the ratio HD/H_2O in comet Lovejoy to be 3.06 x 10^{-4}, or a ratio of D/H in cometary water to be (1.53 x 10^{-4}) (1.4 ± 0.4) x 10^{-4}. Although a marginal detection of HDO, this retrieval suggests that comet Lovejoy has a water isotopic ratio similar to that of Earth (VSMOW, D/H = 1.56 x 10^{-4}).

With GIANO on the TNG we could not detect HDO emission owing to insufficient both sensitivity of the instrument and collecting area of the telescope. In Figure 27 the water fluorescence emission model (red) with the superimposed deuterated water emission model (green) developed by (Villanueva et al., 2012b) are shown. The plotted models are shown for a comet with Lovejoy's water production rate at heliocentric distance of 1 au, rotational temperature ~100K, and D/H ratio of VSMOW. The g-factors reported are corrected for the terrestrial transmittance of our atmosphere. The GIANO sensitivity for each order in g-factor units [s^{-1}] is reported.

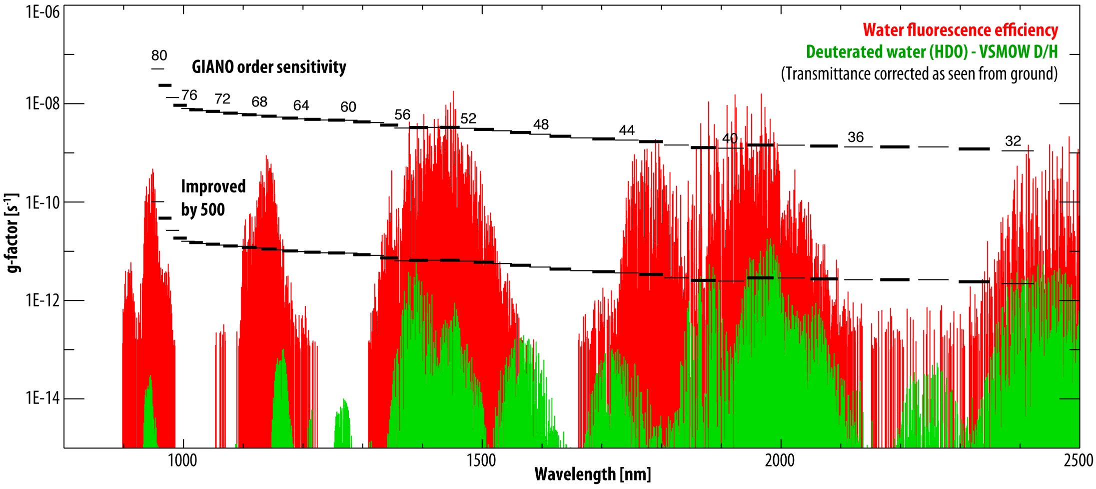

Figure 27
GIANO sensitivity for water detection. The x-axis of the plot shows the wavelength range covered by GIANO from 900 to 2500 [nm]. The y-axis represents the g-factor [s^{-1}], i.e. the fluorescence efficiency. Models for water fluorescence emission (red) and superposed deuterated water fluorescence (green) (g-factors) [s^{-1}] are shown. The models are evaluated at R_h = 1au and T_{rot} = 100 K; they are re-scaled at the VSMOW - D/H ratio value for a comet with a production rate as in C/2014 Q2 Lovejoy. The reported models are corrected for telluric atmospheric transmittance. In black, the GIANO sensitivity and the improved sensitivity for each order is shown.

It is possible to note in Figure 27 with GIANO spectrograph on 3.6 m TNG telescope, we could only detect water across orders 39 - 40 - 41 around 2 μm and 53 - 54 - 55 - 56 near 1.4 μm, as we did.

Future telescopes like the 40mt diameter E-ELT will have a collective area almost 100 times greater that the TNG telescope. Moreover the smaller field of view (see Figure 11 in Chapter 3) can provide a qualitatively estimated improvement in the detected intensity of a factor of ~5, so the sensitivity of an instrument as GIANO could be increased of about ~500. An instrument like GIANO working on a telescope like E-ELT can detect water and deuterated water from the ground.

8.2.2 Carbon and Nitrogen isotopic ratios

The HCN (3-2) line at 265.89 GHz, $H^{13}CN$ (3-2) line at 259.01 GHz and $HC^{15}N$ (3-2) line at 258.16 GHz were detected in comet Lovejoy with IRAM 30mt radio telescope, on January 2015 (Biver et al., 2016). The derived $^{12}C/^{13}C$ ratio is a value of about (109 ± 14), comparable with the terrestrial value (see Figure 12b in Chapter 3). The team also detected a lower limit from methanol $^{12}C/^{13}C > 61$. Although our retrieved value of carbon isotopic ratio is in agreement with these results and with the terrestrial values, our sensitivity limit can not constrain the observed trend in Figure 12b in Chapter 3. Retrieval of the $^{14}N/^{15}N$ isotopic ratio from HCN radio measurements on January 2015 provided a value of about (145 ± 16). This value is in agreement with the twofold enrichment trend observed in the measurements performed in 18 comets from CN and in 2 comets from HCN with respect of telluric value ~272, shown in Figure 12b of Chapter 3 (Jehin et al., 2009), and it is also agrees with the threefold enrichment compared to the proto-solar nebula (~441). Recently, through optical spectroscopic observations with the High Dispersion Spectrograph HDS on Subaru Telescope in Hawaii, (Shinnaka et al., 2016b) derived a value of $^{14}N/^{15}N$ isotopic ratio of about (126 ± 25) from seven emission lines of $^{14}NH_2$ and $^{15}NH_2$ [(100-100) F1 at 570.3582 nm, (111-101) F2 at 571.0959nm, (111-101) F1 at 571.1275 nm, (110-202) F1 at 572.3810 nm, (110-220) F1 at 574.1556 nm, (312-422) F1 at 576.2995 nm, and (312-422) F2 at 576.3076 nm]. The retrieved value is consistent, within the error range, with the nitrogen isotopic ratio value in HCN retrieved by (Biver et al., 2016).

Light elements such as H, H_2, N_2, CO, etc. can show a large range of isotopic ratios (D/H, $^{14}N/^{15}N$, $^{12}C/^{13}C$ etc) among different objects of the solar system. The initial isotopic composition of such species was inferred by the Genesis mission that returned a detailed composition of the Sun and consequently of the solar nebula (Marty et al., 2011). The reason for this variation (see Chapter 3) can be attributed to the several radiative and chemical processes experienced by nebular gases before incorporation into proto-planetesimals. Retrievals of $^{14}N/^{15}N$ ratio in comets are difficult and few measurements have been made. The N-bearing species are around ~1% abundant relative to water in cometary comae (see Figure 7, Chapter 1), thus detection of isotopic species requires very active comets and sensitive techniques. The $^{14}N/^{15}N$ ratio lower limit obtained in our measurements is consistent with the previous retrieved isotopic ratios but, like the carbon isotopic ratio, the sensitivity obtained from our retrieval is not good enough to constrain the observed trend.

8.2.3 Origin of CN radical

The origin of radical CN in cometary coma is not completely resolved and it is not a trivial matter of contention. The radical CN has been studied in a wide spectral range from optical, near infrared to millimeter (Bockelée-Morvan et al., 1985, Rossano et al., 1987, Ziurys et al., 1999, Fray et al., 2005, Jehin et al., 2009, Jockers et al., 2011, Kawakita et al., 2015, Opitom et al., 2015, Paganini and Mumma, 2016, Shinnaka and Kawakita, 2016) trying to understand its origin.

In order to understand if photo-dissociation of HCN produced the detected radical CN in comet Lovejoy, we compared the production rates and mixing ratios achieved from measurements of HCN with our measurements of CN. From (Biver et al., 2016) the HCN production rate, retrieved from the observations on 13-16 January 2015 with IRAM 30mt radio telescope, was a value about Q(HCN) = (4.87 ± 0.02) x10^{26} [s^{-1}]. The relative abundance of hydrogen-cyanide with respect to water provides a value of:

$$\frac{Q_{HCN}}{Q_{H_2O}} \times 100\% = 0.1\%$$

In §7.4 we retrieved a relative abundance for CN relatively to water of about 0.46%, assuming a CN parent (HCN) life time of about τ_p = 70,000 [s] and considering the life time of CN product about τ_d = 220,000 [s]. This disagreement in the mixing ratios of CN and HCN demonstrates that the CN production rate cannot be completely explained by HCN photo-dissociation. The destruction of HCN is a major process of formation of radical CN, but other additional sources are required to explain the CN density in comet Lovejoy and certain other cometary comae. Possible additional parents molecules studied (Fray et al., 2005) such as CH_2CN, HC_3N and C_2N_2, whose scale lengths are comparable with the Haser scale length for parent CN (see equation 1, §1.3.2), are not abundant enough relative to water to explain the corresponding CN production rate. Another hypothesis to explain the CN production rate is the photo-degradation or thermal-degradation of molecular N-bearing compounds stored in cometary grains that could be efficient at heliocentric distances less than 3au (Fray et al., 2005). In future comets, searches for prompt emission from CN radical may help to identify specific molecular precursors.

Chapter 9

Future work

A paradigm shift will occur with HIRES on E-ELT in 2024, the first of the "new generation" 40 mt class telescopes equipped with suitably powerful instruments. But in the relatively near future, we can enhance our knowledge, plan future observations, and develop a "best-use" strategy for E-ELT by working with the emerging instruments now coming on-line. Three are worthy of mention (for instrumental details and performances, see Table 9). iSHELL/NASA-IRTF (commissioned in August 2016), GIARPS/INAF-TNG (the upgraded GIANO and HARPS, available after February 2017), and the upgraded CRIRES+/ESO-VLT (commissioning planned for 2018) will enable huge advances. iSHELL is the first new echelle high-resolution spectrograph available, it offers complete spectral sampling over wide wavelength intervals (e.g., 3.2-3.46 μm in L3 setting), at greatly improved spectral resolving power (λ/δλ ~ 70,000 - 100,000) and much higher sensitivity (2Kx2K HAWAII-2 RG array); active IR guiding will further improve observing efficiency. Importantly, iSHELL has the unique capability to observe during daytime, when some comets are brightest, with the sensitivity to detect HDO at VSMOW levels.

Observations, analysis, and interpretation of the iSHELL, CRIRES+, and GIARPS data, choosing the appropriate instrument settings, will be essential. For example, in the L- and M- bands of iSHELL, we can target biologically relevant species, including H_2O, HDO, CO, HCN, H_2CO, CH_3OH, CH_4, C_2H_2, C_2H_4, C_2H_6, and NH_3. In the J-, H-, and K-bands, we can sense the red-system of radical CN and water hot-bands (as we did with GIANO), identify the precursors for the many unidentified emission lines present in Lovejoy spectra, and search for new emissions (e.g., from C_2 and singlet-O_2). Synthetic spectra of known cometary emitters in the (3-3.5μm) range are shown in Figure 28 at iSHELL resolution; the L3 setting covers the range 3.2-3.46 μm simultaneously.

Table 9
Specifications of the cross-dispersed high-resolution IR spectrometers.

Instrument	Spectral coverage (μm)	Resolving power (λ/δλ)	Spectral coverage for setting	Telescope diam. (m)
GIARPS INAF-TNG	0.6 – 0.7 0.9 – 2.5	110,000	1 setting covers U, B,V, R 1 setting covers Y, J, H, K	3.6
iSHELL NASA-IRTF	1.1 – 5.2	70,000 – 90,000	3 settings to cover J, H, K 5 settings to cover L 2 settings to cover M	3.0
CRIRES+ ESO-VLT	1 – 5.3	100,000	1 setting to cover Y 2 settings to cover J, H 3 settings to cover K 4 settings to cover L 5 settings to cover M	8.2

Table 10
Suitable cometary targets for the coming two years

Comet	Time (mm/yy)	R_H (au)	Δ (au)	V_{geoc} (km/s)	FoM
2P/Encke	03/2017	0.73	0.89	~ 20	1.5
41P/ T-G-K	03–04/2017	1.07	0.15	~ 6	1.7
C/2015 V2	06-07/2017	1.64	0.87	~15	0.7
21P/G-Z	09/2018	1.02	0.40	~11	1.2
46P/Wirtanen	11-12/2018	1.07	0.12	~8	2.8
Bright target-of-opportunity comets are expected at the rate of about 1-3/yr.					

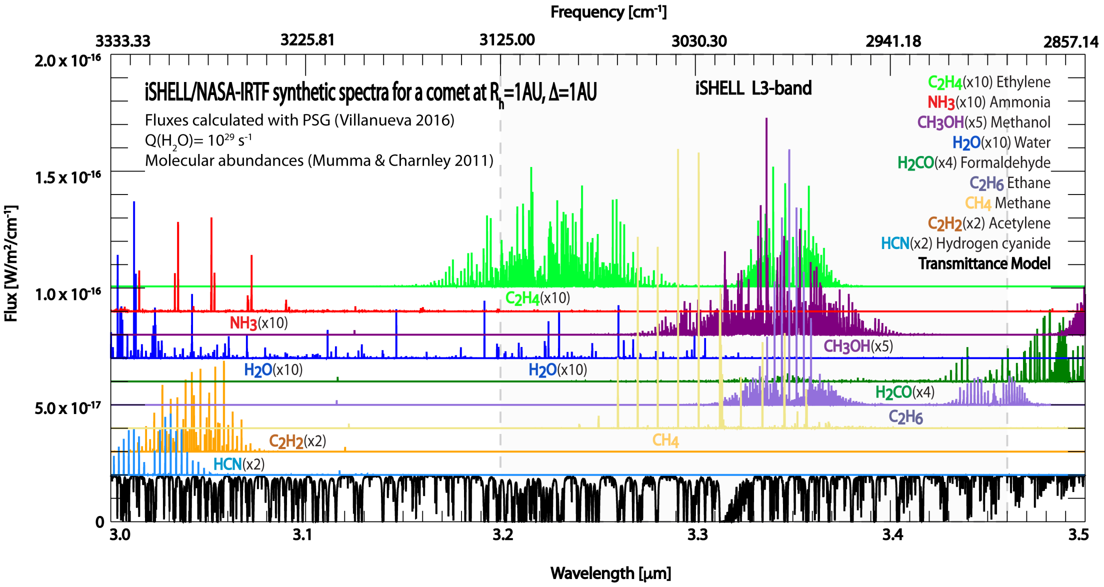

Figure 28. Selected cometary molecular spectra in the range (3 – 3.5 µm) at λ/δλ = 70,000, as synthesized with the GSFC "Planetary Spectrum Generator" (PSG[27]). The emission intensities for spectral lines of C_2H_4, NH_3, CH_3OH, H_2O, H_2CO, C_2H_6, CH_4, C_2H_2 and HCN are shown above the transmittance model (black) of our atmosphere (Mauna Kea). The grey shaded region, between the dashed vertical lines, represents a single setting (L3: 3.2 – 3.46 µm) with iSHELL, in which 5 species are sampled simultaneously. Serendipitous discoveries are enabled by the wide spectral grasp, high resolving power, and high sensitivity.

Multiple target comets are available for ground-based observations, with a Figure of Merit (FoM = $Q_{H2O} * 10^{-29} * R_h^{-1.5} * \Delta^{-1}$) higher than 0.5 (Table 10). [Q_{H2O} is the water production rate at the comet's heliocentric (R_h), and geocentric (Δ) distance when observed.] This parameter (FoM) is strictly connected to the fluorescence brightness of spectral lines in the comet; it indicates the best candidates for which we could perform sensitive measurements (line-by-line) of trace gases. The targets and their observational parameters are listed in Table 10. Unexpected bright new comets can be observed and analyzed as Targets-Of-Opportunity.

This work will provide a **new high-resolution spectral database** of comets obtained with the cutting-edge echelle spectrometers now coming on-line. We could target biologically important organic species emitting in the spectral region (1 – 5 µm), thereby providing

---

[27] http://ssed.gsfc.nasa.gov/psg/

detailed molecular characterizations. **New quantum mechanical fluorescence models** will be developed to properly analyze unidentified molecular emissions (or species) found in our accurately calibrated spectra. Moreover, the advent of extremely large telescopes with very high angular resolution will enable the investigation of molecular emissions in the inner coma regions very near the nucleus. The need to analyze fluorescent emissions under **optically thick conditions** will require development of new (and implementation of existing) molecular fluorescence models to properly interpret them. The analysis of detected species will permit retrieval of cosmogonic parameters (molecular abundances, spin temperatures and isotopic ratios) for testing the delivery of organics and water to Earth by comets. Measurements of **D/H in water** will be of high impact because they will provide new information about the origin of water on our planet, and the multi-line HDO results will remove systematic uncertainties (e.g., in T_{rot}) that plague single-line results. Moreover, our results will provide new constraints for existing theoretical models that depend on assumed local conditions in primordial stages of the solar nebula, and will thereby enhance our understanding of solar system formation and evolution.

We are truly presented with a new frontier in cometary and planetary science!

Appendices

Appendix A.

Table A1 summarizes the wavelength coverage of the 50 orders of a GIANO echellogram. The spectral order number (from 32 to 80) is reported in the first column. For each order, the central wavelength λ_0, the beginning and the ending wavelengths λ_{min} and λ_{max} are shown in columns 2 through 4. Column 5 ($\Delta\lambda$) represents the wavelength subtended by each pixel. The Table is provided by GIANO/TNG web page (see http://www.tng.iac.es/instruments/giano/#manuals).

Table A1.
Central, Beginning, and Ending Wavelength for each spectral order. The nominal pixel subtense is also given for each order.

Spectral order number	**λ_0 µm**	**λ_{min} µm**	**λ_{max} µm**	**$\Delta\lambda$ 10^{-4} µm**
32	2.397	2.369	2.423	0.256
33	2.325	2.297	2.349	0.249
34	2.256	2.230	2.280	0.242
35	2.192	2.166	2.215	0.235
36	2.131	2.106	2.153	0.229
37	2.073	2.049	2.095	0.222
38	2.019	1.995	2.040	0.217
39	1.967	1.944	1.988	0.211
40	1.917	1.895	1.938	0.206
41	18706	1.849	1.890	0.201
42	1.826	1.805	1.845	0.196
43	1.784	1.763	1.802	0.191
44	1.743	1.723	1.761	0.187
45	1.704	1.684	1.722	0.183
46	1.667	1.648	1.685	0.179

47	1.632	1.613	1.649	0.175
48	1.597	1.579	1.614	0.172
49	1.565	1.547	1.581	0.168
50	1.533	1.516	1.550	0.165
51	1.503	1.486	1.519	0.161
52	14744	1.457	1.490	0.158
53	1.447	1.430	1.462	0.155
54	1.420	1.403	1.435	0.152
55	1.394	1.378	1.409	0.150
56	1.369	1.353	1.383	0.147
57	1.345	1.329	1.359	0.144
58	1.322	1.306	1.336	0.142
59	1.299	1.284	1.313	0.140
60	1.277	1.263	1.291	0.137
61	1.256	1.242	1.270	0.135
62	1.236	1.222	1.249	0.133
63	1.217	1.202	1.229	0.131
64	1.197	1.184	1.210	0.129
65	1.179	1.165	1.192	0.127
66	1.161	1.148	1.173	0.125
67	1.144	1.131	1.156	0.123
68	1.127	1.114	1.139	0.121
69	1.111	1.098	1.122	0.119
70	1.095	1.082	1.106	0.118
71	1.079	1.067	1.091	0.116
72	1.064	1.052	1.075	0.114
73	1.050	1.037	1.061	0.113
74	1.035	1.023	1.046	0.111
75	1.021	1.010	1.032	0.110
76	1.008	0.996	1.019	0.108

77	0.995	0.983	1.005	0.107
78	0.982	0.971	0.992	0.106
79	0.970	0.958	0.980	0.104
80	0.957	0.946	0.968	0.103

Appendix B.

Table B1 summarizes the results of the flux calibration process. The first column shows the GIANO spectral order number. The second and third columns report the mean wavelength (λ) and wavelength subtense per pixel (Δλ) evaluated during the calibration. Column four reports the mean flux of the calibration star for each order, while the signal-to-noise ratio (SNR) obtained during flux calibration is shown in column five. Columns 6-9 report the mean flux calibration factors (Γ coefficients) obtained for each track (Topmost, Midup, Middown, and Lowest) and for each order (from 32 to 80).

Table B1.
The Γ coefficients for all 4 tracks of the two fibers (A and B).

Spectr. Order	λ [nm]	Δλ [nm]	Flux10^{-17} [W cm^{-2} µm^{-1}]	SNR	Γ coefficients 10^{-17}[W cm^{-2} µm^{-1} / (ADU/sec)] track positions on array (1,2), and fiber id (A, B)[a]			
					Topmost (B3)	Midup (B4)	Middown (A1)	Lowest (A2)
32	2396.0752	0.02616	2.19	30.9	1.13	2.40	1.15	2.48
33	2323.4006	0.02536	2.92	38.3	1.31	2.81	1.35	2.93
34	2254.9998	0.02460	3.64	53.8	1.52	3.28	1.58	3.46
35	2190.5103	0.02389	4.37	66.9	1.63	3.45	1.66	3.69
36	2129.6035	0.02323	5.10	79.8	1.69	3.67	1.77	3.93
37	2071.9900	0.02259	5.82	61.1	1.85	4.08	1.95	4.38
38	2017.4086	0.02199	6.55	53.3	2.03	4.53	2.15	4.82
39	1965.6276	0.02142	7.28	36.3	2.14	4.80	2.27	5.13

40	1916.4349	0.02088	8.00	95.5	2.01	4.56	1.97	4.39
41	1869.6422	0.02037	8.73	241.2	2.12	4.98	2.17	4.77
42	1825.0779	0.01988	9.45	79.4	2.51	5.77	2.60	5.95
43	1782.5868	0.01941	10.2	35.6	3.03	6.88	3.25	7.50
44	1742.0265	0.01897	10.9	67.7	3.41	7.72	3.67	8.46
45	1703.2695	0.01854	11.6	80.1	3.74	8.50	4.04	9.30
46	1666.1976	0.01813	12.4	78.0	4.11	9.34	4.42	10.2
47	1630.7023	0.01774	13.8	93.0	4.63	10.6	5.03	11.4
48	1596.6864	0.01737	15.3	66.4	5.29	12.1	5.75	13.1
49	1564.0587	0.01701	16.9	72.0	6.01	13.8	6.53	14.9
50	1532.7363	0.01667	18.4	88.8	6.77	15.6	7.34	16.7
51	1502.6404	0.01634	19.9	40.7	7.51	17.3	8.10	18.5
52	1473.7025	0.01602	21.5	26.3	8.25	19.1	8.87	20.3
53	1445.8564	0.01571	23.0	25.9	8.93	20.9	9.63	22.0
54	1419.0410	0.01542	24.5	27.8	9.27	22.0	9.94	22.5
55	1393.1998	0.01514	26.1	84.1	9.71	23.0	10.1	22.3
56	1368.2816	0.01486	27.6	89.5	10.0	23.9	10.0	22.3
57	1344.2369	0.01460	29.1	23.2	11.5	27.1	12.3	28.3
58	1321.0204	0.01434	30.7	26.1	12.2	33.0	15.1	34.8
59	1298.5907	0.01410	32.2	75.2	14.3	33.8	15.4	35.6
60	1276.9080	0.01386	33.7	56.9	15.9	37.4	17.1	39.5
61	1255.9349	0.01363	35.3	75.0	16.5	38.9	18.0	40.8
62	1235.6377	0.01341	36.8	97.5	17.3	40.9	18.6	42.6
63	1215.9846	0.01319	38.3	71.6	18.3	43.3	19.6	44.9
64	1196.9447	0.01298	39.9	55.5	19.5	46.3	20.8	47.7
65	1178.4895	0.01278	41.4	45.7	20.7	52.0	22.1	50.6
66	1160.5929	0.01258	43.0	26.6	22.5	53.5	23.9	54.8
67	1143.2297	0.01239	44.5	18.4	24.3	58.4	25.7	58.7
68	1126.3765	0.01221	46.0	16.4	26.3	62.8	27.6	62.9
69	1110.0103	0.01203	47.6	22.3	27.8	66.5	29.1	66.4
70	1094.1111	0.01185	49.1	54.3	30.1	72.2	31.6	72.0
71	1078.6583	0.01168	50.6	82.5	31.7	76.3	33.2	75.9
72	1063.6345	0.01152	52.2	98.4	34.0	82.2	35.5	80.8
73	1049.0200	0.01136	53.7	110.9	36.5	88.1	37.9	85.2
74	1034.8013	0.01120	55.2	106.8	39.0	94.0	40.2	91.4
75	1020.9597	0.01105	56.8	101.8	41.7	100	42.7	97.3
76	1007.4813	0.01090	58.3	86.2	44.9	109	45.9	116
77	994.3517	0.01076	59.9	91.2	54.3	132	56.2	123
78	981.5579	0.01062	61.4	51.6	78.9	299	75.1	167

79	969.0867	0.01048	62.9	21.7	151	361	133	290
80	956.9262	0.01035	64.5	11.6	366	869	301	620

a. See Figure 1 for positions of A and B fibers on sky, and Figure 2 for track positions of image slices (2 for each fiber) on the array detector.

Appendix C.

The GIANO spectrograph is equipped with a Hawaii-II PACE detector. The acquisition system of GIANO saves multiple non-destructive read-out frames in the local data archive. The number N of non-destructive reads depends on integration time. The system acquires a frame every 10 s, so for an exposure time of 300 s the number of non destructive reads will be 30. These read-out frames are analyzed with the “Flower ramp analysis”, that is performed after the integration (Oliva et al., 2012). If I is the intensity for unit of time and for pixel, every non-destructive read will produce a signal I*t. This analysis consists in the linear fit of measured intensity I, of the N sampled reads, with respect the time t. The error on the fitting allows to obtain the read out noise of only 5 e$^-$/pix.

The dark current and internal background of the instrument present a value of about 0.05 e$^-$/s. This value is close to the 0.033 e$^-$/s reported on the detector data-sheet provided by the manufacturer.

During the observations of 02 February 2015 we collected 10 dark frames, 11 sky frames and 5 nodding (AB) frame on comet Lovejoy (see Table 2). During the data reduction process the frames were arranged as follow: from the 10 dark frames and the 11 sky frames we estimated a mean dark frame (here after D_m) and a mean sky frame (here after S_m). From the 5 nodding on comet we estimated an A-fiber centered mean frame and a B-fiber centered mean frame (here after C^{A}_{m} and C^{B}_{m}). The reduction proceeded as follow: we subtracted the mean dark frame from the mean sky frame (S_m - D_m, here after S_D) and we subtracted the mean dark frame from the A-fiber centered comet mean frame and the B-fiber centered comet mean frame (C^{A}_{m} - D_m , here after A_D and C^{B}_{m} - D_m , here after B_D). Finally we subtracted the dark subtracted mean sky frame from the two dark subtracted mean comet frames (A_D - S_D, here after A and B_D - S_D, here after B). The *Giano_tools* extracts the 1-D spectrum from these cleaned cometary A-frame and B-frame (see Section 2.2).

The expected noise of a single dark frame can be estimated with the following equation:

$$N_D = \sqrt{(D * t_{\text{int}}) + RON^2}$$

while the expected noise of the mean dark frame can be obtained by dividing the noise on the single dark frame by the square-root of the number of dark frames.

$$N_{Dm} = \frac{N_D}{\sqrt{n_{dark}}}$$

where D is the dark current [0.05 e^{-}/s/pix], RON is the read-out noise [5 e^{-}/pix] (reported in Table 1), n_{dark} [10 frame] is the number of dark frames, t_{int} [300 s] is the integration time (reported in Table 2).

The expected noise on dark mean frame is 2.0 e^{-} (0.9 ADU) per pixel. This value is in agreement with the measured noise on mean dark frame of about 2.6 e^{-} (1.2 ADU).

The expected noise on the 1-D sky spectrum, extracted from the mean sky echellogram through *Giano_tool* , can been estimated using the following formula:

$$N_{Sm} = \frac{\sqrt{(S * G) + (D * t_{\text{int}} * n^{y}_{pix}) + (RON^2 * n^{y}_{pix})}}{\sqrt{n_{sky}}}$$

where S is the measured signal on sky spectra [about 14 ADU], D is the dark current [0.05 e^{-}/s/pix], G is the gain of the detector [2.2 e^{-}/ADU], RON is the read-out noise [5 e-/pix] (see Table 1), t_{int} [300 s] is the integration time (see Table 2), n^y_{pix} [4 pix] is the number of row-pixel on the single arch-shaped track from which we extracted a 1-D spectrum adding together the signal of each pixels (see Section 2.2 and Figure 2) and n_{sky} [11 frame] is the number of sky frames.

Due to the fact that each mean sky frame has been dark (mean frame) subtracted, the noise on the mean sky spectrum is obtained by the square root of the square noise of mean sky spectrum plus the square noise of mean dark multiplied for the same number of row-pixel n^y_{pix} [4 pix] from which we extracted the sky spectrum.

$$N^{tot}_{Sm} = \sqrt{N^2_{Sm} + (N^2_D * n^y_{pix})}$$

The expected noise of the mean sky spectrum is 5.8 e^- (2.6 ADU). This value is in agreement with the measured noise on the sky spectrum of about 6.4 e^- (2.9 ADU).

For the comet we have two different cleaned frames, the frame in which the nucleus is centered on fiber A (the coma in sampled in fiber B) and the frame in which the nucleus is centered in fiber B (the coma in sampled in fiber A). From these frames the *Giano_tools* extracts, for each order of GIANO echellogram, four 1-D spectra, that we call track 1, 2, 3 and 4 (see Section 2.2 and Figure 2). In the A-centered frame, the two spectra coming from slicered fiber A (tracks 1 & 2) are sampling the nucleus and the two spectra coming from slicered fiber B (tracks 3 & 4) are sampling the coma, for B-centered frame the situation is exactly the opposite, tracks 1 & 2 of A fiber are sampling the coma and tracks 3 & 4 of fiber B are sampling the nucleus. We chose to estimate the expected noise for order 40 of the A-centered frame. We did the estimation of noise both for a 1-D spectrum sampling the nucleus (track 1) and a 1-D spectrum sampling the coma (track 4).

In order 40 we detected 7 water lines, so we evaluated the noise both considering the signal of line plus cometary continuum and considering the signal from the cometary continuum. The expected noise on the mean comet spectrum sampling the nucleus (A-centered frame, track 1 or 2 and B-centered frame, track 3 or 4) or sampling the coma (A-centered frame, track 3 or 4 and B-centered frame, track 1 or 2) has been estimated using the following formula line by line (here we are showing A-centered frame, track 1, for clarity):

$$N_{C_{A,A1}^{line+cont}} = \frac{\sqrt{(C_{A,A1}^{line+cont} * G) + (D * t_{\mathrm{int}} * n_{pix}^{y} * n_{pix}^{\lambda}) + (RON^2 * n_{pix}^{y} * n_{pix}^{\lambda})}}{\sqrt{n_A}}$$

$$N_{C_{A,A1}^{line+cont}}^{tot} = \sqrt{(N_{C_{A,A1}^{line+cont}})^2 + (N_{Sm})^2 * n_{pix}^{\lambda}}$$

$$N_{C_{A,A1}^{cont}} = \frac{\sqrt{(C_{A,A1}^{cont} * G) + (D * t_{\mathrm{int}} * n_{pix}^{y} * n_{pix}^{\lambda}) + (RON^2 * n_{pix}^{y} * n_{pix}^{\lambda})}}{\sqrt{n_A}}$$

$$N_{C_{A,A1}^{cont}}^{tot} = \sqrt{(N_{C_{A,A1}^{cont}})^2 + (N_{Sm})^2 * n_{pix}^{\lambda}}$$

Considering that the line flux is obtained as: $C_{A,A1}^{line} = C_{A,A1}^{line+cont} - C_{A,A1}^{cont-model}$, the expected noise on the detected lines is:

$$N_{C_{A,A1}^{line}}^{tot} = (N_{C_{A,A1}^{line+cont}})$$

where $C_{A,A1}^{line+cont}$ is the integrated flux under le line plus continuum [ADU], $C_{A,A1}^{cont-model}$ is the model of the continuum (no noise) in [ADU], obtained using the advanced GENLN3 terrestrial model (Edwards, 1992; Villanueva et al., 2015) that synthesizes the transmittance and radiance spectra of Earth's atmosphere. The suffix (A,A1) means that we are considering the nucleus centered on fiber A and we are considering the track 1 of fiber A. D is the dark current [0.05 e-/s/pix], G is the gain of the detector [2.2 e-/ADU], RON is the read-out noise [5 e-/pix] (reported in Table 1), n_A is the number of A comet frames, t_{int} is the integration time [300 s] (reported in Table 2) and n^{λ}_{pix} is the number of pixel under the line [5 pix] from which we estimated the integrated flux and n^{y}_{pix} [4 pix] is the number of row-pixel on the single arch-shaped track from which we extracted a 1-D spectrum. Table

C1 shows the estimated values of noise for order 40, A-centered fiber, on tack A1, i.e. an area sampling the nucleus while in Table C2 the estimated values of noise for order 40, A-centered fiber, on tack B4, i.e. an area sampling the coma, are reported.

Table C1.
Expected noise line by line on order 40 A-centered fiber tack A1 (on nucleus).

Frequency [cm^{-1}]	**$(C \pm N^{tot})_{A,A1}^{line+cont}$ [ADU]**	**$(C \pm N^{tot})_{A,A1}^{cont}$ [ADU]**	**$(C \pm N^{tot})_{A,A1}^{line}$ [ADU]**	**SNR**
5252.39	99.12 ± 7.74	62.19 ± 7.52	36.93 ± 7.74	3.4
5215.04	170.89 ± 8.15	138.04 ± 7.97	32.85 ± 8.15	2.9
5199.75	239.73 ± 8.53	172.47 ± 8.16	67.26 ± 8.53	5.7
5194.56	230.62 ± 8.48	204.93 ± 8.34	25.69 ± 8.48	2.2
5194.28	231.45 ± 8.48	204.93 ± 8.34	26.52 ± 8.48	2.2
5187.98	80.81 ± 7.63	4.18 ± 7.16	76.63 ± 7.63	7.3
5175.41	159.64 ± 8.09	144.39 ± 7.70	15.25 ± 8.09	1.4

a. The integration of flux is done on 5 pixels covering the detected line.

Table C2.
Expected noise line by line on order 40 A-centered fiber tack B4 (on coma).

Frequency [cm^{-1}]	**$(C \pm N^{tot})_{A,B4}^{line+cont}$ [ADU]**	**$(C \pm N^{tot})_{A,B4}^{cont}$ [ADU]**	**$(C \pm N^{tot})_{A,B4}^{line}$ [ADU]**	**SNR**
5252.39	42.90 ± 7.40	24.09 ± 7.29	18.81 ± 7.40	1.8
5215.04	76.56 ± 7.61	63.06 ± 7.53	13.51 ± 7.61	1.3
5199.75	104.66 ± 7.77	89.53 ± 7.69	15.12 ± 7.77	1.4
5194.56	157.70 ± 8.08	90.20 ± 7.69	67.50 ± 8.08	6.1
5194.28	123.75 ± 7.89	90.20 ± 7.69	33.55 ± 7.89	3.0
5187.98	40.40 ± 7.39	8.35 ± 7.18	32.05 ± 7.39	3.1
5175.41	76.58 ± 7.61	70.00 ± 7.67	6.58± 7.61	0.6

a. The integration of flux is done on 5 pixels covering the detected line

To compare the expected noise with respect the measured noise on comet spectra we inserted in *Calib_giano* routine the possibility of computing the noise during the calibration. The noise is computed on the residual spectra after model of transmittance subtraction. In the following table value of measured noise on order 40 both of A-centered and B-centered fibers are reported:

Table C3.
Measured noise on order 40

	Fiber & Track	Noise [ADU/pix]
Fiber A centered on nucleus		
sampling on nucleus	$(A1)^{n}$	3.56
sampling on nucleus	$(A2)^{n}$	4.84
sampling on coma up	$(B3)^{u}$	2.99
sampling on coma up	$(B4)^{u}$	3.07
Fiber B centered on nucleus		
sampling on coma down	$(A1)^{d}$	2.73
sampling on coma down	$(A2)^{d}$	3.21
sampling on nuclues	$(B3)^{n}$	3.53
sampling on nuclues	$(B4)^{n}$	5.15
Combined spectra		
Nucleus	$[(A1)^{n}+(A2)^{n}+(B3)^{n}+(B4)^{n}] / 2$	5.9
Coma up	$(B3)^{u} + (B4)^{u}$	4.8
Coma down	$(A1)^{d}+(A2)^{d}$	4.8

To compare the measured noise with respect the expected noise it is necessary to take into account of the number of pixel, n^{λ}_{pix} [5 pix] on which the signal has been integrated.

For track A1 of A-centered fiber (sampling the nucleus) the measured noise will be (see Table C3): 7.8 e^-/pix (3.6 [ADU/pix]) that, rescaled to $\sqrt{n^{\lambda}_{pix}}$ gives a value of about 17.4 e^- (7.9 [ADU]). This value is in agreement with expected noise of about 17.2 e^-/pix (7.8 [ADU/pix]) evaluated on the continuum. For track B4 of of A-centered fiber (sampling the coma) the measured noise will be: 6.7 e^-/pix (3.1 [ADU/pix]) that, taking into account of $\sqrt{n^{\lambda}_{pix}}$ gives a value of about 15.2 e^- (6.9 [ADU]). This value is in agreement with the expected noise of about 16.5 e^-/pix (7.5 [ADU]) evaluated on the continuum.

As explained in Section 2.2 and showed in Figure 4, *Calib_giano* routine produces 3 distinct residual 1-D spectra combining together the tracks sampling the nucleus (the *center* spectrum) and the tracks sampling the upper and lower parts of the coma (the *coma up* and the *coma down* spectra).

$$I_{nucl} = \frac{I_{A1}^{A-centred} + I_{A2}^{A-centred} + I_{B3}^{B-centred} + I_{B4}^{B-centred}}{2}$$

$$I_{coma\_up} = I_{B3}^{A-centred} + I_{B4}^{A-centred} \qquad I_{coma\_down} = I_{A1}^{B-centered} + I_{A2}^{B-centered}$$

From the usual propagation of the errors, the expected noise on these three spectra has been evaluated as follow, with the assumption that the noises are more or less the same:

$$N_{nucl} = \frac{\sqrt{(N_{A1}^{A-centred})^2 + (N_{A2}^{A-centred})^2 + (N_{B3}^{B-centred})^2 + (N_{B4}^{B-centred})^2}}{2} \approx N_{A1}^{A-centred}$$

$$N_{coma\_up} = \sqrt{(N_{B3}^{A-centred})^2 + (N_{B4}^{A-centred})^2} \approx \sqrt{2} * N_{B4}^{A-centred}$$

$$N_{coma\_down} = \sqrt{\frac{(N_{A1}^{B-centred})^2 + (N_{A2}^{B-centred})^2}{2}} \approx \sqrt{2} * N_{A1}^{B-centred}$$

The expected noise on nucleus spectrum is 17.2 e^- (7.8 [ADU]), while the measured one, rescaled by $\sqrt{n_{pix}^{\lambda}}$ the pixels on which the signal has been integrated, is about 29.0 e^-/pix (13.2 [ADU]) (see Table C3). The expected noise on coma spectra is 23.5 e^- (10.7 [ADU]) while the measured one rescaled by the $\sqrt{n_{pix}^{\lambda}}$ is about 23.6 e^-/pix (10.7 [ADU/pix]). We note that the noise is dominated by read-out noise and dark current noise. The measured noise on nucleus combined spectra seems higher with respect the expected noise on coma combined spectra probably because of larger contribution of cometary continuum in some part of the spectrum between absorption features of atmosphere.

Appendix D.

GIANO spectrograph was originally designed for long-slit spectroscopy and built for direct connection with the focus of TNG telescope. In this configuration the optical efficiency of the spectrometer and preslit system was expected to be close to 60% in the low resolution mode (LR, with resolving power of 400) and of about 39% in the high resolution mode (HR, with resolving power of 50000). The GIANO HAWAII 2-PACE detector has a quantum efficiency of about 73% in K band and 58% in J band. Finally, considering a conservative 75% of efficiency for the telescope, it is possible to obtain a total throughput in the HR mode of 0.21 [e^-/Photons] and 0.17 [e^-/Photons] in K band and J band, respectively; while the throughput for the LR mode are 33% in K band and 26% in J band (Oliva et al., 2006). Due to constraints imposed on the telescope interfacing, during the pre-commissioning phase, GIANO was positioned far from the telescope focus, with a new interface, based on IR-transmitting ZBLAN fibers of about 85μm of diameter, that connect it to the telescope. Fiber equipped spectrographs, to observe both at optical and infrared wavelengths, are used in present telescopes and are going to be used for the future extremely large telescopes because the fibers simplify the interfacing between the spectrograph and the telescope and also because at high spectral resolution they can offer very high spectral accuracy (Iuzzolino et al., 2014).

The first results of fibers's effects on the quality of the spectra achieved with GIANO show that the insertion of fibers probably simplify the interface between the instrument and the telescope, but they reduce drastically the efficiency of the spectrograph. In the Table D1 the evaluation of efficiency for order #60 in the J band, for order #40 at between H and K bands and for order #33 in the K band are reported for comparison with respect the non-fiber original GIANO design. The table describe the entire process to achieve the efficiency [e$^-$/Photons] for Order #60 in the J band, in the order #40 between the H and K band and where we detected water lines, and finally in the order #33 in the K band.

Table D1.
Evaluation of efficiencies for the fibers-fed GIANO spectrograph for comparison with the long-slit GIANO original design in J and K bands.

	Fibers-fed GIANO/TNG Order #60 J band	**Fibers-fed GIANO/TNG Order #40 HK band**	**Fibers-fed GIANO/TNG Order #33 K band**
Wavelength λ[μm]	1.28	1.92	2.32
Frequency k[cm^{-1}]	7831.418	5218.022	4304.036
Delta-Frequency dk[cm^{-1}]	0.085	0.056	0.047
Telescope diameter D[m]	3,58	3,58	3,58
Telescope area A[m^2]	10,07	10,07	10,07
Detector gain G [e$^-$/ADU]	2,20	2,20	2,20
Energy of photon E_{ph} [J]	1.55566E-19	1.03652E-19	8.54966E-20
G [W/m^2/cm^{-1}/ADU/s]	9.42E-17	2.54E-17	2.46E-17
G [Photons/m^2/cm^{-1}/ADU]	606	245	288
G [Photons /cm^{-1} / ADU]	6097	2464	2897
G [Photons / cm^{-1}/ e$^-$]	2772	1120	1317
G [Photons / e$^-$]	236	64	62
e [e$^-$/Photons]	0.0042	0.0157	0.0162

As it is possible to note, the efficiency of GIANO is about 0.016 [e$^-$/Photons] in the K band and 0.004 [e$^-$/Photons] in the J band. The presence of fibers reduced the efficiency of the instrument of a about a factor 10 in the K band and of about a factor 40 in J band with respect to the expected efficiency obtained with long-slit spectroscopy. In the Table D2 a complete summary of the throughputs evaluated for the entire set of 50 orders of GIANO and corresponding efficiencies are reported. The third column shows the Γ in 10^{-17}[W m^{-2} cm^{-1} / ADU/s]. The last column reports the corresponding efficiency [%], i.e. [e^{-}/Photons] multiplied for 100, for each GIANO's order.This huge reduction of efficiency is probably due to the loss of flux at fibers connectors.

Table D2.
Evaluation of the GIANO throughputs across the entire echellogram.

Order	**λ**	**Γ**	ε
#	**[nm]**	**10^{-17} [W m^{-2} cm^{-1} / ADU/s]**	[%]
32	2396.0752	2.236518	1,78
33	2323.4006	2.459726	1,62
34	2254.9998	2.698658	1,47
35	2190.5103	2.704925	1,47
36	2129.6035	2.696096	1,48
37	2071.9900	2.815947	1,41
38	2017.4086	2.940760	1,35
39	1965.6276	2.955593	1,35
40	1916.4349	2.535801	1,57
41	1869.6422	2.604736	1,53
42	1825.0779	2.964431	1,34
43	1782.5868	3.469142	1,15
44	1742.0265	3.732411	1,07
45	1703.2695	3.923136	1,02
46	1666.1976	4.121253	0,97
47	1630.7023	4.466336	0,89
48	1596.6864	4.895304	0,82
49	1564.0587	5.336371	0,75
50	1532.7363	5.764774	0,69
51	1502.6404	6.134699	0,65
52	1473.7025	6.475901	0,62
53	1445.8564	6.767458	0,59
54	1419.0410	6.755584	0,59
55	1393.1998	6.701955	0,60
56	1368.2816	6.550135	0,61
57	1344.2369	7.538176	0,53
58	1321.0204	8.430976	0,47
59	1298.5907	8.777704	0,46
60	1276.9080	9.423168	0,42
61	1255.9349	9.501420	0,42

62	1235.6377	9.597469	0,42
63	1215.9846	9.815923	0,41
64	1196.9447	10.11903	0,40
65	1178.4895	1.048423	0,38
66	1160.5929	10.93939	0,37
67	1143.2297	11.45874	0,35
68	1126.3765	11.97358	0,33
69	1110.0103	12.28162	0,33
70	1094.1111	12.94164	0,31
71	1078.6583	13.24031	0,30
72	1063.6345	13.78423	0,29
73	1049.0200	14.33537	0,28
74	1034.8013	14.86165	0,27
75	1020.9597	15.40755	0,26
76	1007.4813	16.43670	0,24
77	994.3517	19.05040	0,21
78	981.5579	27.25312	0,15
79	969.0867	46.18023	0,09
80	956.9262	103.5567	0,04

Acknowledgments
Ringraziamenti

This thesis represents the conclusion of a work done with a lot of people, not only people belonging to the academic world, but also people that are part of my life from many years.
These few lines of acknowledgments are reductive.
Every single one of you knows exactly his/her importance for me.

Questa tesi rappresenta la conclusione di un lavoro svolto con molte persone, non solo appartenenti al mondo accademico, ma anche persone che fanno parte della mia vita quotidiana da tanti anni.
Queste poche righe di ringraziamenti sono riduttive.
Ognuno di voi sa esattamente l'importanza che riveste per me.

I want to start by sincerely thanking my advisors in Osservatorio Astrofisico di Arcetri, John e Gian Paolo. Thanks to have been my teachers, my guides, my unexpected friends. Thanks to have taught me this work, and infuse to me the passion for astrobiology and cometary science. Thanks to allow me to enhance my knowledge.
Thanks for the trust and the advices you always gave me on work and in my personal life. Thanks for your presence in the first astronomical observations, the first talks, and the PhD course. I could not be more lucky than I have been to met you in my life.

Vorrei iniziare ringraziando sinceramente John e Gian Paolo, i miei tutori presso l'Osservatorio Astrofisico di Arcetri. Grazie di essere stati per me insegnanti, guide e inaspettatamente amici. Grazie di avermi insegnato questo lavoro e avermi trasmesso la passione per l'astrobiologia e lo studio delle comete. Grazie di avermi permesso di ampliare le mie conoscenze.
Vi ringrazio per la fiducia e i consigli che mi avete sempre dato, sia sul lavoro che nella vita privata. Grazie per la vostra presenza durante le mie prime osservazioni astronomiche, i miei talks, e tutto il corso di dottorato. Non potevo essere piú fortunata di cosi nell'avervi incontrati nella mia vita.

I than want to deeply thank Mike and Geronimo that hosted me in Goddard many times and made me always feel part of the team. Thanks for the long talks about science. Thanks to teach me a lot and thanks to stimulate my thirsty of knowledge.
Thanks to make me feel at home when I was far from it. Thanks for the empathy.

Vorrei poi profondamente ringraziare Mike e Geronimo che mi hanno ospitata a Goddard per molte volte e mi hanno sempre fatto sentire parte del team. Grazie per le lunghe chiaccherate scientifiche. Grazie di avermi insegnato molto e grazie di aver stimolato la mia sete di sapere. Grazie di avermi sempre fatto sentire a casa, quando ero lontana da essa. Grazie per l'empatia.

I thank Tino, Andrea, Fabrizio, Nicoletta, Francesca, Emilio and the TNG staff for the observations and data reduction with GIANO. Thanks for your help.

Grazie a Tino, Andrea, Fabrizio, Nicoletta, Francesca, Emilio e lo staff del TNG per le osservazioni e la riduzione dati GIANO. Grazie per il vostro aiuto.

I would like to thank Susi. Thanks for your supporting presence. For your wise advises, for listening me and for your true friendship. Thanks for the "piani per stare insieme sempre" (plans to be always close)! Thanks for the shared phone-beers between Maryland and Ohio, for the usual call after work, and for your trust!
I also thank all the PhD students (and Yuri) at Arcetri Observatory. Thanks for sharing with me all these years and make them wonderful.

Vorrei ringraziare Susi. Grazie per la tua presenza. Per i tuoi saggi consigli, per ascoltarmi e per la tua amicizia sincera. Grazie per "i piani per stare insieme sempre"! Grazie per le birre telefoniche, condivise tra il Maryland e l'Ohio, per la nostra chiamata post lavoro, e per la tua fiducia!
Vorrei anche ringraziare tutti i dottorandi (e Yuri) dell'Osservatorio di Arcetri. Grazie per aver condiviso con me tutti questi anni e averli resi meravigliosi.

I want to thank my friends, my second family. Talk about you would take me probably another manuscript because you are part of my life from kindergarten. You have been a certainty and you have been always present. Each one of you is essential for me! Thanks to be there.

Voglio ringraziare i miei amici di sempre, la mia seconda famiglia. Per parlare di voi non mi basterebbe un'altra tesi perché siete parte della mia vita dai tempi dell'asilo. Siete stati una certezza e siete stati sempre presenti. Ognuno di voi é essenziale per me! Grazie di esserci.

At the end, because the most important, I thank my parents. Thanks to support me, to believe in my dreams. Thanks to understand me. Thanks to leave me free. Thanks to be always there when I needed. Thanks to teach me your values and to be the best example of love I have never seen. Thanks for your love.

In fine, perché il ringraziamento piú importante, ringrazio i miei genitori.
Grazie del supporto che mi avete dato, di aver creduto in me quando ne avevo bisogno. Grazie di avermi insegnato i vostri valori e di avermi regalato il migliore esempio di amore che abbia mai avuto. Grazie per il vostro amore.

References

Abrams, M.C., Goldman, A., Gunson, M.R., Rinsland, C.P., Zander, R., 1996. Observations of the infrared solar spectrum from space by the ATMOS experiment. Appl. Opt. 35, 2747.

A'Hearn, M.F., Millis, R.C., Schleicher, D.O., Osip, D.J., Birch, P.V., 1995. The Ensemble Properties of Comets: Results from Narrowband Photometry of 85 Comets, 1976-1992. Icarus 118, 223–270. doi:10.1006/icar.1995.1190

Altwegg, K., Balsiger, H., Bar-Nun, A., Berthelier, J.J., Bieler, A., Bochsler, P., Briois, C., Calmonte, U., Combi, M., de Keyser, J., Eberhardt, P., Fiethe, B., Fuselier, S., Gasc, S., Gombosi, T.I., Hansen, K.C., Hässig, M., Jäckel, A., Kopp, E., Korth, A., LeRoy, L., Mall, U., Marty, B., Mousis, O., Neefs, E., Owen, T., Reme, H., Rubin, M., Sémon, T., Tzou, C.Y., Waite, H., Wurz, P., 2015. 67P/Churyumov-Gerasimenko, a Jupiter family comet with a high D/H ratio. Science 347, 1261952. doi:10.1126/science.1261952

Arpigny, C., Schulz, R., Manfroid, J., Ilyin, I., Stüwe, J.A., Zucconi, J.-M., 2000. The isotope ratios 12C/13C and 14N/15N in comet C/1995 O1 (Hale-Bopp). American Astronomical Society 32, 41.14–.

Biver, N., Bockelée-Morvan, D., Colom, P., Crovisier, J., Germain, B., Lellouch, E., Davies, J.K., Dent, W.R.F., Moreno, R., Paubert, G., Wink, J., Despois, D., Lis, D.C., Mehringer, D., Benford, D.J., Gardner, M., Phillips, T.G., Gunnarsson, M., Rickman, H., Winnberg, A., Bergman, P., Johansson, L.E.B., Rauer, H., 1997. Long-term Evolution of the Outgassing of Comet Hale-Bopp From Radio Observations. Earth 78, 5–11. doi:10.1023/A:1006229818484

Biver, N., Moreno, R., Bockelée-Morvan, D., Sandqvist, A., Colom, P., Crovisier, J., Lis, D.C., Boissier, J., Debout, V., Paubert, G., Milam, S., Hjalmarson, Å., Lundin, S., Karlsson, T., Battelino, M., Frisk, U., Murtagh, D., team, T.O., 2016. Isotopic ratios of H, C, N, O, and S in comets C/2012 F6 (Lemmon) and C/2014 Q2 (Lovejoy). arXiv. doi:10.1051/0004-6361/201528041

Bockelée-Morvan, D., Biver, N., Jehin, E., Cochran, A.L., Wiesemeyer, H., Manfroid, J., Hutsemékers, D., Arpigny, C., Boissier, J., Cochran, W., Colom, P., Crovisier, J., Milutinovic, N., Moreno, R., Prochaska, J.X., Ramirez, I., Schulz, R., Zucconi, J.-M., 2008. Large Excess of Heavy Nitrogen in Both Hydrogen Cyanide and Cyanogen from Comet 17P/Holmes. Astrophys. J. 679, L49–L52. doi:10.1086/588781

Bockelée-Morvan, D., Colom, P., Crovisier, J., Despois, D., Paubert, G., 1991. Microwave detection of hydrogen sulphide and methanol in Comet Austin (1989c1). Nature 350, 318–320. doi:10.1038/350318a0

Bockelée-Morvan, D., Crovisier, J., Mumma, M.J., Weaver, H.A., 2004. The composition of cometary volatiles. Comets II 391–423.

Bockelée-Morvan, Crovisier, J., 1985. Possible parents for the cometary CN radical - Photochemistry and excitation conditions. A&A 151, 90.

Bonev, B.P., Mumma, M.J., Gibb, E.L., Di Santi, M.A., Villanueva, G.L., Magee-Sauer, K., Ellis, R.S., 2009. Comet C/2004 Q2 (Machholz): Parent Volatiles, a Search for Deuterated Methane, and Constraint on the CH_4 Spin Temperature. Astrophys. J. 699, 1563–1572. doi:10.1088/0004-637X/699/2/1563

Bonev, B.P., Mumma, M.J., Dello Russo, N., Gibb, E.L., DiSanti, M.A., Magee-Sauer, K.,

2004. Infrared OH Prompt Emission as a Proxy of Water Production in Comets: Quantitative Analysis of the Multiplet Near 3046 cm-1 in Comets C/1999 H1 (Lee) and C/2001 A2 (LINEAR). Astrophys. J. 615, 1048–1053. doi:10.1086/424587

Brooke, J.S.A., Ram, R.S., Western, C.M., Li, G., Schwenke, D.W., Bernath, P.F., 2014. Einstein A Coefficients and Oscillator Strengths for the A 2Π-X 2Σ+ (Red) and B2Σ+-X2Σ+ (Violet) Systems and Rovibrational Transitions in the X 2Σ+ State of CN. The Astrophysical Journal Supplement 210, 23. doi:10.1088/0067-0049/210/2/23

Brooke, T.Y., Tokunaga, A.T., Weaver, H.A., Crovisier, J., Bockelée-Morvan, D., Crisp, D., 1996. Detection of acetylene in the infrared spectrum of comet Hyakutake. Nature 383, 606–608. doi:10.1038/383606a0

Buntkowsky, G., Limbach, H.H., Walaszek, B., Adamczyk, A., Xu, Y., Xu, Y., Breitzke, H., Schweitzer, A., Gutmann, T., Waechtler, M., Frydel, J., Elnmler, T., Amadeu, N., Tietze, D., Chaudret, B., 2008. Mechanisms of dipolar ortho/para-H2O conversion in ice. Zeitschrift Fur Physikalische Chemie-International Journal of Research in Physical Chemistry & Chemical Physics 222, 1049–1063. doi:10.1524/zpch.2008.5359

Caselli, P., 2005. Chemical Processes in Star Forming Regions, in: Astrophysics and Space Science Library, Astrophysics and Space Science Library. Springer New York, New York, NY, pp. 47–66. doi:10.1007/0-387-26357-8_4

Caselli, P., Ceccarelli, C., 2012. Our astrochemical heritage. Astron Astrophys Rev 20, 56. doi:10.1007/s00159-012-0056-x

Charnley, S.B., Rodgers, S.D., 2008. Interstellar Reservoirs of Cometary Matter. Space Sci. Rev. 138, 59–73. doi:10.1007/s11214-008-9331-6

Colangeli, L., Epifani, E., Brucato, J.R., Bussoletti, E., De Sanctis, C., Fulle, M., Mennella, V., Palomba, E., Palumbo, P., Rotundi, A., 1999. Infrared spectral observations of comet 103P/Hartley 2 by ISOPHOT. A&A 343, L87–L90.

Combes, M., Crovisier, J., Encrenaz, T., Moroz, V.I., Bibring, J.P., 1988. The 2.5-12 micron spectrum of Comet Halley from the IKS-VEGA Experiment. Icarus 76, 404–436. doi:10.1016/0019-1035(88)90013-9

Combes, M., Moroz, V.I., Crifo, J.F., Lamarre, J.M., Charra, J., Sanko, N.F., Soufflot, A., Bibring, J.-P., Cazes, S., Coron, N., Crovisier, J., Emerich, C., Encrenaz, T., Gispert, R., Grigoriev, A.V., Guyot, G., Krasnopolsky, V.A., Nikolskii, Y.V., Rocard, F., 1986. Infrared Sounding from Comet Halley - Preliminary Results from VEGA-1. SOVIET ASTR.LETT.(TR:PISMA) V.12 12, 257.

Cremonese, G., Boehnhardt, H., Crovisier, J., Fitzsimmons, A., Fulle, M., Licandro, J., Pollacco, D., Rauer, H., Tozzi, G.P., West, R.M., 1997. Neutral sodium from comet Hale-Bopp: a third type of tail. arXiv. doi:10.1086/311040

Crovisier, J., Brooke, T.Y., Hanner, M.S., Keller, H.U., Lamy, P.L., Altieri, B., Bockelée-Morvan, D., Jorda, L., Leech, K., Lellouch, E., 1996. The infrared spectrum of comet C/1995 O1 (Hale-Bopp) at 4.6 AU from the Sun. A&A 315, L385–L388.

Crovisier, J., Encrenaz, T., 1983. Infrared fluorescence of molecules in comets - The general synthetic spectrum. A&A 126, 170.

Dello Russo, N., Mumma, M.J., DiSanti, M.A., , Magee-Sauer, K., Novak, R.E., Rettig, T.W., 2000. Water Production and Release in Comet C/1995 O1 Hale-Bopp. Icarus 143, 324–337. doi:10.1006/icar.1999.6268

Dello Russo, N., DiSanti, M.A., Mumma, M.J., Magee-Sauer, K., Rettig, T.W., 1998. Carbonyl Sulfide in Comets C/1996 B2 (Hyakutake) and C/1995 O1 (Hale-Bopp): Evidence for an Extended Source in Hale-Bopp. Icarus 135, 377–388. doi:10.1006/icar.1998.5990

Dello Russo, N., Kawakita, H., Vervack, R.J., Weaver, H.A., 2016. Emerging trends and a comet taxonomy based on the volatile chemistry measured in thirty comets with high-resolution infrared spectroscopy between 1997 and 2013. Icarus 278, 301–332. doi:10.1016/j.icarus.2016.05.039

Dello Russo, N., Mumma, M.J., DiSanti, M.A., Magee-Sauer, K., 2002. Production of ethane and water in comet C/1996 B2 Hyakutake. J. Geophys. Res. Pl. 107, 5095. doi:10.1029/2001JE001838

DiSanti, M.A., Bonev, B.P., Magee-Sauer, K., Dello Russo, N., Mumma, M.J., Reuter, D.C., Villanueva, G.L., 2006. Detection of Formaldehyde Emission in Comet C/2002 T7 (LINEAR) at Infrared Wavelengths: Line-by-Line Validation of Modeled Fluorescent Intensities. Astrophys. J. 650, 470–483. doi:10.1086/507118

DiSanti, M.A., Mumma, M.J., 2008. Reservoirs for Comets: Compositional Differences Based on Infrared Observations. Space Sci. Rev. 138, 127–145. doi:10.1007/s11214-008-9361-0

DiSanti, M.A., Mumma, M.J., Dello Russo, N., Magee-Sauer, K., 2001. Carbon Monoxide Production and Excitation in Comet C/1995 O1 (Hale-Bopp): Isolation of Native and Distributed CO Sources. Icarus 153, 361–390. doi:10.1006/icar.2001.6695

DiSanti, M.A., Mumma, M.J., Dello Russo, N., Magee-Sauer, K., Griep, D.M., 2003. Evidence for a dominant native source of carbon monoxide in Comet C/1996 B2 (Hyakutake). J. Geophys. Res. Pl. 108, 5061. doi:10.1029/2002JE001961

Eberhardt, P., Reber, M., Krankowsky, D., Hodges, R.R., 1995. The D/H and ^18^O/^16^O ratios in water from comet P/Halley. A&A 302, 301.

Edwards, D.P., 1992. GENLN2: A General Line-by-Line Atmospheric Transmittance and Radiance Model. The National Center for Atmospheric Research: Technical Note 367-STR.

Ehrenfreund, P., Charnley, S.B., 2000. Organic Molecules in the Interstellar Medium, Comets, and Meteorites: A Voyage from Dark Clouds to the Early Earth. Annu. Rev. Astron. Astrophys. 38, 427–483. doi:10.1146/annurev.astro.38.1.427

Faggi, S., Villanueva, G.L., Mumma, M.J., Brucato, J.R., Tozzi, G.P., Oliva, E., Massi, F., Sanna, N., Tozzi, A., 2016a. Detailed Analysis of Near-IR Water (H2O) Emission in Comet C/2014 Q2 (Lovejoy) with the GIANO/TNG Spectrograph. Astrophys. J. 830, 157. doi:10.3847/0004-637X/830/2/157

Faggi, S., Villanueva, G.L., Mumma, M.J., Tozzi, G.-P., Brucato, J.R., 2016b. Near-Infrared high resolution spectral survey of comets with GIANO/TNG: The CN red-system at 1.1 μm. American Astronomical Society 48, #217.03.

Feldman, P.D., Cochran, A.L., Combi, M.R., 2004. Spectroscopic investigations of fragment species in the coma. Comets II 425–447.

Feldman, P.D., Weaver, H.A., Burgh, E.B., 2002. Far Ultraviolet Spectroscopic Explorer Observations of CO and H2 Emission in Comet C/2001 A2 (LINEAR). Astrophys. J. 576, L91–L94. doi:10.1086/343089

Festou, M.C., Keller, H.U., Weaver, H.A., 2004. A brief conceptual history of cometary science. Comets II 3–16.

Fray, N., Benilan, Y., Cottin, H., Gazeau, M.C., Crovisier, J., 2005. The origin of the CN radical in comets: A review from observations and models. Planet. Space Sci. 53, 1243–1262. doi:10.1016/j.pss.2005.06.005

Gibb, E.L., Bonev, B.P., Villanueva, G.L., DiSanti, M.A., Mumma, M.J., Sudholt, E., Radeva, Y., 2012. Chemical Composition of Comet C/2007 N3 (Lulin): Another "Atypical“” Comet. Astrophys. J. 750, 102. doi:10.1088/0004-637X/750/2/102

Gibb, E.L., Mumma, M.J., DiSanti, M.A., Dello Russo, N., Magee-Sauer, K., 2002. An infrared search for HDO in comets, in:. Presented at the In: Proceedings of Asteroids, pp. 705–708.

Gilmour, I., Sephton, M.A., 2004. An introduction to astrobiology. An introduction to astrobiology.

Gladman, B., 2005. The Kuiper Belt and the Solar System's Comet Disk. Science 307, 71–75. doi:10.1126/science.1100553

Gladman, B., Chan, C., 2006. Production of the Extended Scattered Disk by Rogue Planets. Astrophys. J. 643, L135–L138. doi:10.1086/505214

Gomes, R., Levison, H.F., Tsiganis, K., Morbidelli, A., 2005. Origin of the cataclysmic Late Heavy Bombardment period of the terrestrial planets. Nature 435, 466–469. doi:10.1038/nature03676

Hartogh, P., Lis, D.C., Bockelée-Morvan, D., de Val-Borro, M., Biver, N., Küppers, M., Emprechtinger, M., Bergin, E.A., Crovisier, J., Rengel, M., Moreno, R., Szutowicz, S., Blake, G.A., 2011. Ocean-like water in the Jupiter-family comet 103P/Hartley 2. Nature 478, 218–220. doi:10.1038/nature10519

Hase, F., Demoulin, P., Sauval, A.J., Toon, G.C., Bernath, P.F., Goldman, A., Hannigan, J.W., Rinsland, C.P., 2006. An empirical line-by-line model for the infrared solar transmittance spectrum from 700 to. J. Quant. Spectrosc. Radiat. Transfer 102, 450–463. doi:10.1016/j.jqsrt.2006.02.026

Hase, F., Wallace, L., Mcleod, S.D., Harrison, J.J., Bernath, P.F., 2010. The ACE-FTS atlas of the infrared solar spectrum. J. Quant. Spectrosc. Radiat. Transfer 111, 521–528. doi:10.1016/j.jqsrt.2009.10.020

Herzberg, G., 1950. Molecular Spectra and Molecular Structure. I Spectra of Diatomic Molecules. D. Van Nostrand Company, Inc., Princeton, New Jersey.

Herzberg, G., Huber, K.-P., 1950. Molecular spectra and molecular structure. I. Spectra of diatomic molecules. Van Nostrand.

Hoban, S., Mumma, M.J., Reuter, D.C., DiSanti, M.A., Joyce, R.R., Storrs, A., 1991. A tentative identification of methanol as the progenitor of the 3.52-micron emission feature in several comets. Icarus 93, 122–134. doi:10.1016/0019-1035(91)90168-S

Irvine, W.M., Bergin, E.A., Dickens, J.E., Jewitt, D., Lovell, A.J., Matthews, H.E., Schloerb, F.P., Senay, M., 1998. Chemical processing in the coma as the source of cometary HNC. Nature 393, 547–550. doi:10.1038/31171

Iuzzolino, M., Tozzi, A., Sann, N., Zangrillli, L., Oliva, E., 2014, Preliminary results on the characterization and performances of ZBLAN fiber for infrared spectrographs, in:. p. 914766. doi:10.1117/12.2055093

Jehin, E., Manfroid, J., Hutsemékers, D., Arpigny, C., Zucconi, J.-M., 2009. Isotopic Ratios in Comets: Status and Perspectives. Earth 105, 167–180. doi:10.1007/s11038-009-9322-y

Jewitt, D., Luu, J., 1993. Discovery of the candidate Kuiper belt object 1992 QB1. Nature (ISSN 0028-0836) 362, 730–732. doi:10.1038/362730a0

Jewitt, D., Luu, J., Marsden, B.G., 1992. 1992 QB1. IAU Circ. 5611, 1.

Jewitt, D., Matthews, H.E., Owen, T., Meier, R., 1997. The 12C/13C, 14N/15N and 32S/34S Isotope Ratios in Comet Hale-Bopp (C/1995 O1). Science 278, 90–93. doi:10.1126/science.278.5335.90

Jewitt, D., 2012. The Active Asteroids. Astronomical Journal 143. doi:10.1088/0004-6256/143/3/66

Jockers, K., Szutowicz, S., Villanueva, G.L., Bonev, T., Hartogh, P., 2011. HCN and CN in Comet 2P/Encke: Models of the non-isotropic, rotation-modulated coma and CN parent life time. Icarus 215, 153–185. doi:10.1016/j.icarus.2011.06.038

Kawakita, H., Dello Russo, N., Furusho, R., Fuse, T., Watanabe, J.-I., Boice, D.C., Sadakane, K., Arimoto, N., Ohkubo, M., Ohnishi, T., 2006. Ortho - to - Para Ratios of Water and Ammonia in Comet C/2001 Q4 (NEAT): Comparison of Nuclear Spin Temperatures of Water, Ammonia, and Methane. Astrophys. J. 643, 1337–1344.

doi:10.1086/503185

Kawakita, H., Shinnaka, Y., Kondo, S., Hamano, S., Sameshima, H., Nakanishi, K., Kawanishi, T., Nakaoka, T., Otsubo, S., Kinoshita, M., Ikeda, Y., Yamamoto, R., Izumi, N., Fukue, K., Yasui, C., Mito, H., Sarugaku, Y., Matsunaga, N., Kobayashi, N., 2015. High-resolution spectroscopy of the CN red system in comet C/2013 R1 (Lovejoy) using WINERED at Koyama Astronomical Observatory. American Astronomical Society 47, 415.15.

Keller, H.U., Britt, D., Buratti, B.J., Thomas, N., 2004. In situ observations of cometary nuclei. Comets II 211–222.

Keller, H.U., Lillie, C.F., 1974. The Scale Length of OH and the Production Rates of H and OH in Comet Beunett (1970 II). A&A 34, 187–.

Kurucz, R.L., 2009. Including All the Lines, in:. Presented at the AIP Conference Proceedings, pp. 43–51. doi:10.1063/1.3250087

Larson, H.P., Davis, D.S., Mumma, M.J., Weaver, H.A., 1986. Velocity-resolved observations of water in comet Halley. Astrophys. J. 309, L95–L99. doi:10.1086/184769

Le Roy, R.J., Henderson, R.D.E., 2007. A new potential function form incorporating extended long-range behaviour: application to ground-state Ca2. Molecular Physics 105, 663–677. doi:10.1080/00268970701241656

Lis, D.C., Bockelée-Morvan, D., Boissier, J., Crovisier, J., Biver, N., Charnley, S.B., 2008. Hydrogen Isocyanide in Comet 73P/Schwassmann-Wachmann (Fragment B). Astrophys. J. 675, 931–936. doi:10.1086/527345

Magee-Sauer, K., Mumma, M.J., DiSanti, M.A., Dello Russo, N., 2002. Hydrogen cyanide in comet C/1996 B2 Hyakutake. J. Geophys. Res. Pl. 107, 5096. doi:10.1029/2002JE001863

Magee-Sauer, K., Mumma, M.J., DiSanti, M.A., Dello Russo, N., Rettig, T.W., 1999. Infrared Spectroscopy of the ν3 Band of Hydrogen Cyanide in Comet C/1995 O1 Hale-Bopp. Icarus 142, 498–508. doi:10.1006/icar.1999.6215

Manfroid, J., Jehin, E., Hutsemékers, D., Cochran, A., Zucconi, J.-M., Arpigny, C., Schulz, R., Stüwe, J.A., Ilyin, I., 2009. The CN isotopic ratios in comets. arXiv. doi:10.1051/0004-6361/200911859

Marty, B., Zimmermann, L., Krot, A.N., 2011. Early Irradiation as a Possible Cause of 15N Enrichment in Early Solar System Matter. Workshop on Formation of the First Solids in the Solar System 1639, 9129–.

McKay, A.J., Chanover, N.J., DiSanti, M.A., Morgenthaler, J.P., Cochran, A.L., Harris, W.M., Russo, N.D., 2014. Rotational variation of daughter species production rates in Comet 103P/Hartley: Implications for the progeny of daughter species and the degree of chemical heterogeneity. Icarus 231, 193–205. doi:10.1016/j.icarus.2013.11.029

Meier, R., Eberhardt, P., Krankowsky, D., Hodges, R.R., 1993. The extended formaldehyde source in comet P/Halley. A&A 277, 677–.

Meier, R., Owen, T.C., Matthews, H.E., Jewitt, D.C., Bockelée-Morvan, D., Biver, N., Crovisier, J., Gautier, D., 1998. A Determination of the HDO/H2O Ratio in Comet C/1995 O1 (Hale-Bopp). Science 279, 842.

Morbidelli, A., 2008. Comets and Their Reservoirs: Current Dynamics and Primordial Evolution. Trans-Neptunian Objects and Comets. Saas-Fee Advanced Course 35. Swiss Society for Astrophysics and Astronomy Series: Saas-Fee Advanced Courses 79.

Morbidelli, A., Levison, H.F., Tsiganis, K., Gomes, R., 2005. Chaotic capture of Jupiter's Trojan asteroids in the early Solar System. Nature 435, 462–465. doi:10.1038/nature03540

Morbidelli, A., Rickman, H., 2015. Comets as collisional fragments of a primordial planetesimal disk. A&A. doi:10.1051/0004-6361/201526116

Mumma, M.J., Blass, W.E., Weaver, H.A., Larson, H.P., 1988. Measurements of the Ortho-Para Ratio and Nuclear Spin Temperature of Water Vapor in Comets Halley and Wilson(1986l) and Implications for Their Origin and Evolution. BAAS 20, 826–.

Mumma, M.J., Charnley, S.B., 2011. The Chemical Composition of Comets—Emerging taxonomies and Natal Heritage 49, 471–524.

Mumma, M.J., DiSanti, M.A., Dello Russo, N., Magee-Sauer, K., Gibb, E.L., Novak, R., 2003. Remote infrared observations of parent volatiles in comets: A window on the early solar system. Adv. Space Res. 31, 2563–2575. doi:10.1016/S0273-1177(03)00578-7

Mumma, M.J., Dello Russo, N., DiSanti, M.A., Magee-Sauer, K., Novak, R.E., Brittain, S.D., Rettig, T., McLean, I.S., Reuter, D.C., Xu, L.-H., 2001a. Organic Composition of C/1999 S4 (LINEAR): A Comet Formed Near Jupiter? Science 292, 1334–1339. doi:10.1126/science.1058929

Mumma, M.J., DiSanti, M.A., Dello Russo, N., Fomenkova, M., Magee-Sauer, K., Kaminski, C.D., Xie, D.X., 1996. Detection of Abundant Ethane and Methane, Along with Carbon Monoxide and Water, in Comet C/1996 B2 Hyakutake: Evidence for Interstellar Origin. Science 272, 1310–1314. doi:10.1126/science.272.5266.1310

Mumma, M.J., DiSanti, M.A., Xie, X., 1995. Comet 6P/d'Arrest. IAU Circ. 6228, 2.

Mumma, M.J., McLean, I.S., DiSanti, M.A., Larkin, J.E., Dello Russo, N., Magee-Sauer, K., Becklin, E.E., Bida, T., Chaffee, F., Conrad, A.R., Figer, D.F., Gilbert, A.M., Graham, J.R., Levenson, N.A., Novak, R.E., Reuter, D.C., Teplitz, H.I., Wilcox, M.K., Xu, L.-H., 2001b. A Survey of Organic Volatile Species in Comet C/1999 H1 (Lee) Using NIRSPEC at the Keck Observatory. Astrophys. J. 546, 1183–1193. doi:10.1086/318314

Mumma, M.J., Weaver, H.A., Larson, H.P., 1987. The Ortho-Para Ratio of Water Vapor in Comet p/ Halley. A&A 187, 419–424.

Mumma, M.J., Weaver, H.A., Larson, H.P., Williams, M., Davis, D.S., 1986. Detection of water vapor in Halley's comet. Science 232, 1523–1528. doi:10.1126/science.232.4757.1523

Mumma, M.J., , Weissman, P.R., Stern, S.A., 1993. Comets and the origin of the solar system - Reading the Rosetta Stone. In: Protostars and planets III (A93-42937 17-90) 1177–1252.

Mumma, M.J., Reuter, D.C., 1989. On the identification of formaldehyde in Halley's comet. Astrophysical Journal 344, 940–948. doi:10.1086/167862

Oliva, E., Biliotti, V., Baffa, C., Giani, E., Gonzalez, M., Sozzi, M., Tozzi, A., Origlia, L., 2012. Performances and results of the detector acquisition system of the GIANO spectrometer. High Energy 8453, 84532T. doi:10.1117/12.925293

Oliva, E., Origlia, L., Baffa, C., Biliotti, C., Bruno, P., D'Amato, F., Del Vecchio, C., Falcini, G., Gennari, S., Ghinassi, F., Giani, E., Gonzalez, M., Leone, F., Lolli, M., Lodi, M., Maiolino, R., Mannucci, F., Marcucci, G., Mochi, I., Montegriffo, P., Rossetti, E., Scuderi, S., Sozzi, M., 2006. The GIANO-TNG spectrometer, in: McLean, I.S., Iye, M. (Eds.). Presented at the Astronomical Telescopes and Instrumentation, SPIE, pp. 626919–626919–10. doi:10.1117/12.670006

Oliva, E., Origlia, L., Maiolino, R., Baffa, C., Biliotti, V., Bruno, P., Falcini, G., Gavriousev, V., Ghinassi, F., Giani, E., Gonzalez, M., Leone, F., Lodi, M., Massi, F., Montegriffo, P., Mochi, I., Pedani, M., Rossetti, E., Scuderi, S., Sozzi, M., Tozzi, A., Valenti, E., 2013. A GIANO-TNG high-resolution infrared spectrum of the airglow emission. A&A 555. doi:10.1051/0004-6361/201321366

Oliva, E., Origlia, L., Scuderi, S., Benatti, S., Carleo, I., Lapenna, E., Mucciarelli, A., Baffa, C., Biliotti, V., Carbonaro, L., Falcini, G., Giani, E., Iuzzolino, M., Massi, F., Sanna, N., Sozzi, M., Tozzi, A., Ghedina, A., Ghinassi, F., Lodi, M., Harutyunyan, A., Pedani, M., 2015. Lines and continuum sky emission in the near infrared: observational constraints from deep high spectral resolution spectra with GIANO-TNG. A&A 581. doi:10.1051/0004-6361/201526291

Ootsubo, T., Kawakita, H., Hamada, S., Kobayashi, H., Yamaguchi, M., Usui, F., Nakagawa, T., Ueno, M., Ishiguro, M., Sekiguchi, T., Watanabe, J.-I., Sakon, I., Shimonishi, T., Onaka, T., 2012. AKARI Near-infrared Spectroscopic Survey for CO2 in 18 Comets. Astrophys. J. 752, 15. doi:10.1088/0004-637X/752/1/15

Opitom, C., Jehin, E., Manfroid, J., Hutsemékers, D., Gillon, M., Magain, P., 2015. TRAPPIST photometry and imaging monitoring of comet C/2013 R1(Lovejoy): Implications for the origin of daughter species. Astronomy & Astrophysics, Volume 584, id.A121, 10 pp.

Paganini, L., Mumma, M., Villanueva, G., Keane, J., Blake, G., Bonev, B., DiSanti, M., Gibb, E., Meech, K., 2014. Identification of CO-rich comet C/2013 R1 (Lovejoy) --- a new member of the CO-rich family. Asteroids.

Paganini, L., Mumma, M.J., Gibb, E.L., DiSanti, M.A., Milam, S.N., Bonev, B.P., Cordiner, M.A., Charnley, S., Faggi, S., Villanueva, G.L., 2015. The favorable apparition of comet C/2014 Q2 (Lovejoy), and unique insights from ground-based IR observations. American Astronomical Society 47.

Paganini, L., Mumma, M.J., 2016. A Solar-pumped Fluorescence Model for Line-by-line Emission Intensities in the B–X, A–X, and X–X Band Systems of 12C14N. The Astrophysical Journal Supplement Series 226, 3. doi:10.3847/0067-0049/226/1/3

Ram, R.S., Wallace, L., Bernath, P.F., 2010. High resolution emission spectroscopy of the A 2П-X 2Σ + (red) system of 12C 14N. Journal of Molecular Spectroscopy 263, 82–88. doi:10.1016/j.jms.2010.07.002

Rossano, G.S., Rudy, R.J., Russell, R.W., Puetter, R.C., Chapman, S.C., 1987. One-micron CN observations of Comet Halley. Astronomical Society of the Pacific 99, 1099–1101. doi:10.1086/132086

Russo, Dello, N., Vervack, R.J., Weaver, H.A., Kawakita, H., Kobayashi, H., Biver, N., Bockelée-Morvan, D., Crovisier, J., 2009. THE PARENT VOLATILE COMPOSITION OF 6P/d’ARREST AND A CHEMICAL COMPARISON OF JUPITER-FAMILY COMETS MEASURED AT INFRARED WAVELENGTHS. Astrophys. J. 703, 187–197. doi:10.1088/0004-637X/703/1/187

Schloerb, F.P., Kinzel, W.M., Swade, D.A., Irvine, W.M., 1986. HCN production from comet Halley. Astrophysical Journal 310, L55–L60. doi:10.1086/184781

Shinnaka, Y., Kawakita, H., Jehin, E., Decock, A., Hutsemékers, D., Manfroid, J., 2016a. Ortho-to-para abundance ratios of NH2in 26 comets: implications for the real meaning of OPRs. Mon. Not. R. Astron. Soc. 462, S124–S131. doi:10.1093/mnras/stw2298

Shinnaka, Y., Kawakita, H., Jehin, E., Decock, A., Hutsemékers, D., Manfroid, J., Arai, A., 2016b. Nitrogen isotopic ratios of NH 2 in comets: implication for 15 N-fractionation in cometary ammonia. Mon. Not. R. Astron. Soc. 462, S195–S209. doi:10.1093/mnras/stw2410

Shinnaka, Y., Kawakita, H., 2016. Spectroscopic observations of 14N/15N ratios in both NH2 and CN in comet C/2013 US10 (Catalina). American Astronomical Society 48, #330.07.

Sierks, H., Barbieri, C., Lamy, P.L., Rodrigo, R., Koschny, D., Rickman, H., Keller, H.U., Agarwal, J., A'Hearn, M.F., Angrilli, F., Auger, A.-T., Barucci, M.A., Bertaux, J.-L., Bertini, I., Besse, S., Bodewits, D., Capanna, C., Cremonese, G., Da Deppo, V., Davidsson, B., Debei, S., De Cecco, M., Ferri, F., Fornasier, S., Fulle, M., Gaskell, R., Giacomini, L., Groussin, O., Gutierrez-Marques, P., Gutiérrez, P.J., Güttler, C., Hoekzema, N., Hviid, S.F., Ip, W.-H., Jorda, L., Knollenberg, J., Kovacs, G., Kramm, J.R., Kührt, E., Küppers, M., La Forgia, F., Lara, L.M., Lazzarin, M., Leyrat, C., Lopez Moreno, J.J., Magrin, S., Marchi, S., Marzari, F., Massironi, M., Michalik, H., Moissl, R., Mottola, S., Naletto, G., Oklay, N., Pajola, M., Pertile, M., Preusker, F., Sabau, L., Scholten, F., Snodgrass, C., Thomas, N., Tubiana, C., Vincent, J.-B., Wenzel, K.-P., Zaccariotto, M., Pätzold, M., 2015. On the nucleus structure and activity of comet 67P/Churyumov-Gerasimenko. Science 347, aaa1044. doi:10.1126/science.aaa1044

Tozzi, G.P., Feldman, P.D., 1998. Origin and production of C (^ 1D) atoms in cometary comae. Astronomy and ….

Tozzi, G.P., Festou, M.C., 1990. Vectorial Model Scalelengths for Comet Coma Abundance Determinations. Asteroids 463–.

Villanueva, G.L., Mumma, M.J., DiSanti, M.A., Bonev, B.P., Gibb, E.L., Magee-Sauer, K., Blake, G.A., Salyk, C., 2011a. The molecular composition of Comet C/2007 W1 (Boattini): Evidence of a peculiar outgassing and a rich chemistry. Icarus 216, 227–240. doi:10.1016/j.icarus.2011.08.024

Villanueva, G.L., Mumma, M.J., Magee-Sauer, K., 2011b. Ethane in planetary and cometary atmospheres: Transmittance and fluorescence models of the ν_7 band at 3.3 μm. J. Geophys. Res. Pl. 116, 1–23. doi:10.1029/2010JE003794

Villanueva, G.L., Mumma, M.J., Novak, R., Radeva, Y.L., Kaufl, H., Smette, A., Hartogh, P., Encrenaz, T., 2010. Water on Mars: global maps of H_2O, HDO and D/H obtained with CRIRES at VLT and NIRSPEC at Keck II. Am. Geophys. Unio. 52, 05.

Villanueva, G.L., DiSanti, M.A., Mumma, M.J., Xu, L.-H., 2012a. A Quantum Band Model of the ν_3 Fundamental of Methanol (CH_3OH) and its Application to Fluorescence Spectra of Comets. Astrophys. J. 747, 1–11. doi:10.1088/0004-637X/747/1/37

Villanueva, G.L., , Magee-Sauer, K., Mumma, M.J., 2013. Modeling of nitrogen compounds in cometary atmospheres: Fluorescence models of ammonia (NH_3), hydrogen cyanide (HCN), hydrogen isocyanide (HNC) and cyanoacetylene (HC_3N). J. Quant. Spectrosc. Radiat. Transfer 129, 158–168. doi:10.1016/j.jqsrt.2013.06.010

Villanueva, G.L., Mumma, M.J., Bonev, B.P., Novak, R.E., Barber, R.J., DiSanti, M.A., 2012b. Water in planetary and cometary atmospheres: H_2O/HDO transmittance and fluorescence models. J. Quant. Spectrosc. Radiat. Transfer 113, 202–220. doi:10.1016/j.jqsrt.2011.11.001

Villanueva, G.L., Mumma, M.J., Novak, R.E., Käufl, H.-U., Hartogh, P., Encrenaz, T., Tokunaga, A., Khayat, A., Smith, M.D., 2015. Strong water isotopic anomalies in the martian atmosphere: Probing current and ancient reservoirs. Science 348, 218–221. doi:10.1126/science.aaa3630

Wallace, L., Livingston, W., 2003. An atlas of the solar spectrum in the infrared from 1850 to 9000 cm-1 (1.1 to 5.4 micrometer). An atlas of the solar spectrum in the infrared from 1850 to 9000 cm-1 (1.1 to 5.4 micrometer).

Walsh, K.J., Morbidelli, A., Raymond, S.N., O'Brien, D.P., Mandell, A.M., 2012. Populating the asteroid belt from two parent source regions due to the migration of giant planets-"The Grand Tack." Meteoritics & Planetary Science 47, 1941–1947. doi:10.1111/j.1945-5100.2012.01418.x

Weaver, H.A., Feldman, P.D., Festou, M.C., A'Hearn, M.F., 1981. Water production models for comet Bradfield /1979 X/. Astrophys. J. 251, 809. doi:10.1086/159525

Weaver, H.A., Mumma, M.J., 1984. Infrared molecular emissions from comets. Astrophys. J. 276, 782–797. doi:10.1086/161664

Weaver, H.A., , Mumma, M.J., Larson, H.P., Davis, D.S., 1986. Post-perihelion observations of water in comet Halley. Nature 324, 441–444. doi:10.1038/324441a0

Weissman, P.R., Asphaug, E., Lowry, S.C., 2004. Structure and density of cometary nuclei. Comets II 337–357.

Western, C., 2010. Recent Changes in Pgopher: a General Purpose Program for Simulating Rotational Structure. "International Symposium On Molecular Spectroscopy.

Xie, X., Mumma, M.J., 1992a. The contribution of electron collisions to rotational excitations of cometary water. In Lunar and Planetary Inst.

Xie, X., Mumma, M.J., 1992b. The effect of electron collisions on rotational populations of cometary water. Astrophysical Journal 386, 720–728. doi:10.1086/171053

Yamamoto, T., 1981. On the photochemical formation of CN, C2, and C3 radicals in cometary comae. The Moon and the Planets 24, 453–463. doi:10.1007/BF00896911

Ziurys, L.M., Savage, C., Brewster, M.A., Apponi, A.J., Pesch, T.C., Wyckoff, S., 1999. Cyanide Chemistry in Comet Hale-Bopp (C/1995 O1). Astrophys. J. 527, L67–L71. doi:10.1086/312388